# Applications of porous ceramics based on capillary suspensions

Zur Erlangung des akademischen Grades eines
DOKTORS DER INGENIEURWISSENSCHAFTEN (Dr.-Ing.)

von der KIT-Fakultät für Chemieingenieurwesen und Verfahrenstechnik des
Karlsruher Instituts für Technologie (KIT)
genehmigte

DISSERTATION

von
David Nikolaus Georg Menne
aus Langenfeld, Deutschland

Tag der mündlichen Prüfung: 12.04.2023

Erstgutachter: Prof. Dr. Norbert Willenbacher
Zweitgutachter: Prof. Dr. Christof Hübner

# Preface

This publication based dissertation consists of two peer-reviewed scientific journal articles and one peer-reviewed conference proceeding. They include the main results of my experimental work at the Karlsruhe Institute of Technology (KIT), Institute of Mechanical Process Engineering and Mechanics in the group of Applied Mechanics during November 2017 until February 2021.

This thesis follows a brief introduction to the state of the art on porous materials in general and the innovative and inexpensive processing route for manufacturing highly porous sintered materials based on capillary suspensions. The main part of this dissertation consists of the following publications:

- A Robust Soil Water Potential Sensor with High Sensitivity and Broad Measuring Range
- Robust Soil Water Potential Sensor to Optimize Irrigation in Agriculture
- Giant Functional Properties in Porous Electroceramics through Additive Manufacturing of Capillary Suspensions

The dissertation concludes with a generally summary, an outlook as well as a bibliography. The bibliography includes all references of the publications. Hereby, the publications are slightly changed. Some graphs and images are modified in size and color.

# Acknowledgments

I would like to take this opportunity to thank the people who contributed to the success of my dissertation during my time at the Karlsruhe Institute of Technology (KIT) through direct or indirect help with experimental work, fruitful discussions or general support.

First and foremost, I would like to thank my supervisor Prof. Dr. Norbert Willenbacher for giving me the opportunity to do my doctorate under his guidance at the Institute of Mechanical Process Engineering and Mechanics (MVM) in the Applied Mechanics Group (AME). Norbert, I thank you for your trust, your support and for creating an environment with great scientific freedom and creativity.

Furthermore, I would like to thank Prof. Dr. Christof Trübner from the Department of Electrical Engineering of the Hochschule Mannheim. Christof thank you for the successful collaboration, the fruitful discussions, for sharing your expertise in the field of sensors and for taking over as second reviewer of my thesis.

Between August and November 2020, I spend three-months as a visiting researcher in the Functional Materials and Materials Chemistry (FACET) group at the Norwegian University of Science and Technology (NTNU) in Trondheim, Norway under the guidance of Prof. Dr. Julia Glaum. Julia, thank you for the amazing time in Norway. I am very grateful to have been a part of your unit in the FACET group. I felt very welcomed from the first moment, and it was a unique experience. Particularly, I am thankful for the help and input of Dr. Magnus Rotan during my time at NTNU.

Furthermore, I particularly acknowledge the help offered by Dr. Manuel Hinterstein from the Institute for Applied Materials (IAM) in the Ceramic Materials and Technologies (KWT) group. Thank you for the successful cooperation, the fruitful discussions and for sharing your expertise in the field of functional ceramics.

My deep gratitude also to the technical staff of the MVM, especially to Klaus Hirsch, Astrid Huber, Regina Mall and Thomas Lebe for their valuable technical support.

This work would have not been possible without the work of my students. It was a pleasure for me to work with you: Jens-Cedric Höpfer, Christina Litunenko, Benjamin Kanz, Felipe Buffa-Fehr, Dominik Nath, Sebastian Brecht, Marian Weißschuh, Aicha Laghmani, Tamara Milicic, Yuan Yu, Thayane Cantoni da Rocha, Max Ailinger, Nikolas Müller and Anna Koltsova.

I am very grateful to all my colleagues at the AME. Thank you Dr. Bernhard Hochstein and Dr. Claude Oelschläger for your technical and scientific advice. In particular, I want to thank my office colleagues Walter Oswald, Steffen Recktenwald, Annika Hodapp, Ophélie Ranquet and Kevin Tedjokusuma. Thank you for all the laughs we shared. Moreover, I thank Walter Oswald, Moritz Weiß and Ronald Gordon for the long board-game nights and the great time during my doctorate. I also want to mention Ceren Yüce, Annika Völp and Johanna Roether. The time with all of you was incredible.

Thank you to my girlfriend Isabel. You always show me what is really important in life.

Last but not least, I thank my family - my parents Veronika and Georg and my siblings, Mirjam and Raphael - for your never ending support.

# Abstract

Ceramic materials exhibit good oxidation, corrosion and temperature resistance, low thermal expansion, high mechanical strength and good biocompatibility. Porous ceramic materials also exhibit high permeability and are therefore used in a variety of industrial processes such as filtration, as catalyst supports, in energy conversion and storage, as lightweight materials, and as biomimetic materials. For each application, the specific properties of the ceramics, such as porosity, pore size, material composition and component shape, can be adapted and optimized. Four methods have been established for the production of porous ceramics: Partial sintering, sacrificial templating, replica technique and direct foaming. However, with these four manufacturing methods, pore size ranges between 1 and 10 µm at porosities > 50 % are difficult to realize. This gap could be closed by using capillary suspensions for the manufacturing of porous ceramics.

Capillary suspensions are three-phase systems consisting of a particulate solid and two immiscible liquids. One of the liquids is present in the system only in a small amount (typically < 5 vol%). The state in which the secondary fluid wets the particles better than the bulk fluid is called the pendular state. Here, binary bridges of secondary fluid connect adjacent particles and cause attractive capillary forces forming a percolating particle network. This structure formation is accompanied by a change in the flow properties: depending on the type and amount of the secondary liquid added, the properties change from liquid or slightly elastic to strongly gel-like. The resulting pasty and moldable material can be processed using all established techniques, including extrusion-based 3D printing. In addition, the particle network is so stable that it does not collapse even during debinding and sintering processes, producing a molded part with a defined pore structure and high mechanical strength. The novel manufacturing method can be applied to all common ceramic materials. However, the ceramic materials investigated so far did not exhibit any functional properties. In addition, no usable ceramic product based on this principle has been developed so far.

In this dissertation, a first product was developed to market readiness in cooperation with TRUEBNER GmbH, which uses a ceramic based on capillary suspensions as the main component. The product is a soil water potential sensor, with which the plant available water in the soil can be determined. In the ceramic disc, a wide pore size distribution (0.5 to 200 µm) ensures that water can be absorbed from a wide variety of soils. High porosity (> 69 ± 0.1 %) of the ceramic disks allows high water absorption and thus high measurement accuracy. A new circuit board system was built by TRUEBNER GmbH from a transmission line within a time-domain transmission circuit. In this way, a change in the dielectric response of the ceramic discs can be detected as the water uptake changes. The versatility of the new sensor was tested in a large number of laboratory and field experiments in different soil types. The advantages of the new sensor were demonstrated in cooperation with several farms under real conditions, e.g. in the cultivation of blueberries, asparagus and tomatoes. The new sensor provided accurate and reliable data during the trials. Through a comparative study, an empirical relationship was established between the output signal of the new sensor and the soil water potential determined with a commercial tensiometer. This makes it possible to determine the soil water potential with the new sensor without knowledge of the soil type. For this reason, the new sensor can be used for optimized irrigation.

Furthermore, in this dissertation a porous electroceramic based on capillary suspensions was manufactured, 3D printed and characterized with respect to its electromechanical properties for the first time. The capillary suspension was optimized for the 3D printing process Direct Ink Writing in such a way that strut-to-pore ratios of approx. 1:6 (70 µm strut diameter and 440 µm pore diameter) can be realized. Printed strut diameters of that small size have not been documented to date. To investigate the electrical properties, hierarchically structured barium titanate ceramics with printed mesostructure (~ 100 µm) and pore sizes of about 1 µm in the struts with closed bottom and top layers and internal 3-3 connectivity were manufactured. The overall porosity was > 60 % in this case. The unique structure of the particle network of capillary suspensions in the 3D printed structures enables tailored dielectric and electromechanical coupling, resulting in a remanent piezoelectric coefficient $d_{33rem}$ value of 330 pC $N^{-1}$ with a remanent relative permittivity of 1197. As a result, the energy harvesting figure of merit $FOM_{33}$ reaches a value of 10.3 $pm^2 N^{-1}$, which is more than four times higher than any documented data for barium titanate. This proves that the combination of 3D printing and the advantageous microstructure from capillary suspensions can extremely enhance the piezoelectric and electromechanical properties of electroceramics. This opens up new potentials in a variety of applications such as electromechanical energy harvesting, electrode materials for batteries or fuel cells, thermoelectrics or bone tissue engineering with piezoelectrically stimulated cell growth.

# Zusammenfassung

Keramische Materialien weisen gute Oxidations-, Korrosions- und Temperaturbeständigkeit, eine geringe Wärmeausdehnung, eine hohe mechanische Festigkeit und eine gute Biokompartibilität auf. Poröse keramische Materialien weisen darüber hinaus eine hohe Permeabilität auf und finden daher Anwendung in einer Vielzahl von industriellen Prozessen wie beispielsweise der Filtration, als Katalysatorträger, in der Energieumwandlung und -speicherung, als Leichtbaumaterialien und als biomimetische Materialien. Für jede Anwendung können die spezifischen Eigenschaften der Keramik wie die Porosität, die Porengröße, die Materialzusammensetzung und die bauteilform angepasst und optimiert werden. Zur Herstellung von porösen Keramiken haben sich vier Methoden etabliert: Partielles Sintern, Platzhaltermethode, Replikatechnik und Direktschäumung. Mit diesen vier Herstellungsmethoden sind jedoch Porengrößenbereich zwischen 1 und 10 µm bei Porositäten > 50 % nur schwer zu realisieren. Diese Lücke könnte durch die Verwendung von Kapillarsuspensionen für die Herstellung von porösen Keramiken geschlossen werden.

Kapillarsuspensionen sind drei Phasen Systeme, die aus einem Partikulären Feststoff und zwei nicht miteinander mischbaren Flüssigkeiten bestehen. Eine der Flüssigkeiten liegt nur in einer geringen Menge (meist< 5 vol%) im System vor. Der Zustand, in dem die Sekundärflüssigkeit die Partikel besser benetzt als die Hauptflüssigkeit, wird als *pendular state* bezeichnet. Hier verbinden binäre Brücken der Sekundärflüssigkeit benachbarte Partikel und verursachen anziehende Kapillarkräfte, die ein perkolierendes Partikelnetz bilden. Das Netzwerk wird durch die Kapillarkräfte, die durch die Ausbildung von Flüssigkeitsbrücken an den Kontaktstellen zwischen den Partikeln entstehen, zusammengehalten. Mit dieser Strukturbildung geht die Änderung der Fließeigenschaften einher: Je nach Art und Menge der zugegebenen zweiten Flüssigkeit verändern sich die Eigenschaften von flüssig oder schwach elastisch zu stark gel-artig. Der so entstandene pastöse und formbare Stoff lässt sich mit allen etablierten Techniken inklusive dem 3D Druck verarbeiten. Darüber hinaus ist das Partikelnetzwerk so stabil, dass es auch beim Entbinder- und Sinterprozess nicht kollabiert und ein Formteil mit definierter Porenstruktur und hoher mechanischer Festigkeit erzeugt wird. Die neuartige Herstellungsmethode lässt sich auf alle gängigen keramischen Sintermaterialien anwenden. Die bisher untersuchten keramischen Materialien wiesen dabei jedoch keine funktionellen Eigenschaften auf. Hinzu kommt, dass bisher noch kein verwertbares keramisches Produkt auf Basis dieses Prinzips entwickelt wurde.

In dieser Dissertation wurde in Kooperation mit der TRUEBNER GmbH ein erstes Produkt bis zur Marktreife hin entwickelt, das eine Keramik auf Basis von Kapillarsuspensionen als Hauptkomponente verwendet. Das Produkt ist ein Saugspannungssensor, mit dem das pflanzenverfügbare Wasser im Boden bestimmt werden kann. In der Keramikscheibe gewährleistet eine breite Porengrößenverteilung (0.5 bis 200 µm), dass Wasser aus unterschiedlichsten Böden aufgenommen werden kann und eine Messung unabhängig von der Bodenzusammensetzung erfolgt. Eine hohe Porosität (> 69 ± 0.1 %) der Keramikscheiben ermöglicht eine hohe Wasseraufnahme und damit eine hohe Messgenauigkeit. Von der TRUEBNER GmbH wurden leiterplattenintegrierte Übertragungsleitungen als Sensorelemente entwickelt, deren Ausbreitungseigenschaften mit einer Hochfrequenzschaltung im Zeitbereich erfasst werden. Auf diese Weise kann eine Veränderung des dielektrischen Verhaltens der Keramikscheiben bei einer sich verändernden Wasseraufnahme festgestellt werden. In einer Vielzahl an Labor- und Feldversuchen in unterschiedlichen Bodenzusammensetzungen wurde die Vielseitigkeit des neuen Sensors erprobt. Dabei konnten die Vorteile des neuen Sensors in Kooperation mit einigen Landwirtschaftsbetrieben unter Realbedingen, z.B. beim Anbau von Heidelbeeren, Spargel und Tomaten, aufgezeigt werden. Der neue Sensor liefert bei den Versuchen genaue und zuverlässige Daten. Durch eine vergleichende Studie wurde eine empirische Beziehung zwischen Ausgangssignal des neuen Sensors und dem mit einem kommerziellen Tensiometer ermittelten Saugspannung hergestellt. Dadurch ist eine Bestimmung der Saugspannung ohne Kenntnis der Bodenzusammensetzung mit dem neuen Sensor möglich. Aus dem Grund kann der neue Sensor für eine optimierte Bewässerung eingesetzt werden.

Des Weiteren wurde in dieser Dissertation erstmalig eine poröse Elektrokeramik auf Basis von Kapillarsuspensionen hergestellt, 3D gedruckt und auf ihre elektromechanischen Eigenschaften untersucht. Die Kapillarsuspension wurde für das 3D Druck Verfahren Direct Ink Writing derart optimiert, dass sich Steg-Poren-Verhältnisse von ca. 1:6 (70 µm Steg- und 440 µm Porendurchmesser) realisieren lassen. Derartige geringe Durchmesser von gedruckten Streben sind bisher nicht dokumentiert worden. Um die elektrischen Eigenschaften zu untersuchen wurden hierarchisch strukturierte Bariumtitanat-Keramiken mit gedruckter Mesostruktur (~ 100 µm) und Porengrößen von ca. 1 µm in den Streben mit geschlossenen Boden- und Deckenschichten und innerer 3-3-Konnektivität hergestellt. Die Gesamtporosität betrug dabei > 60 %. Die einzigartige Struktur des Partikelnetzwerks der Kapillarsuspensionen in den 3D gedruckten Bauteilen ermöglicht eine maßgeschneiderte dielektrische und elektromechanische Kopplung, was zu einem remanenten piezoelektrischen Koeffizienten $d_{33rem}$-Wert von 330 pC $N^{-1}$ bei einer remanente relative Permittivität von 1197 führt. Die Energy Harvesting Leistungszahl $FOM_{33}$ erreicht dadurch einen Wert von 10,3 pm² $N^{-1}$, was mehr als

viermal höher ist als alle dokumentierten Daten für Bariumtitanat. Das beweist, dass sich durch die Kombination aus 3D Druck und der Vorteilhaften Mikrostruktur von Kapillarsuspensionen die piezoelektrischen und elektromechanischen Eigenschaften von Elektrokeramiken extrem erweitern lassen. Auf diese Weise werden neue Potentiale in einer Vielzahl an Anwendungen wie beispielsweise elektromechanisches Energy Harvesting, Elektrodenmaterialien für Batterien oder Brennstoffzellen, Thermoelektrik oder Knochenersatzmaterialien mit piezoelektrisch stimuliertem Zellwachstum möglich.

# Notations

## Abbreviations

| | |
|---|---|
| AM | Additive manufacturing / Additive manufactured |
| BSE | Backscattering method |
| BT | Barium titanium oxide / Barium titanate |
| TCP | Beta-Tricalciumphosphat / β-Tricalciumphosphat |
| BURPS | Burned out polymer spheres |
| CAPS | Capillary Suspension |
| CIP | Cold-isostatic-press |
| CS | Conventionally sintered |
| CT / XCT | X-ray computed tomography |
| DIW | Direct ink writing |
| DPF | Diesel particulate filters |
| EDXS | Energy-dispersive X-ray spectroscopy |
| EMI | Electromagnetic interference |
| FEM | Finite element method |
| LVE | Linear viscoelastic regime |
| LVG | Teaching and Research Institute for Horticulture |
| MEMS | Micro-mechanical systems |
| SEM | Scanning electron microscope |
| SOFC | Solid oxide fuel cell |
| SWP | Soil water potential |
| TDT | Time-domain transmission |
| TEM | Transmission electron microscopy |
| XRD | X-ray diffraction |

## Latin symbols

| | | |
|---|---|---|
| $\sigma_y$ | Apparent yield stress | [Pa] |
| $x_{pore,av}$ | Average pore size | [µm] |
| $F_C$ | Capillary force | [N] |
| $E_c$ | Coercive electric field | [kV/mm] |
| $Q_3$ | Cumulative distribution | [-] |
| z | Distance between the layers of the log-pile structure | [µm] |
| S | Distance between the two spherical particles | [µm] |
| $FOM_{33}$ | Energy harvesting Figure of Merit | [pm$^2$/N] |
| $g_1$ | Grain size | [µm] |
| $t_H$ | Holding time in furnace | [h] |
| $G''$ | Loss modulus | [Pa] |
| $d_{33max}$ | Maximum piezoelectric strain coefficient (high field) | [pC/N] |
| $P_{max}$ | Maximum polarization (high field) | [µC/cm$^2$] |
| $S_{max}$ | Maximum strain (high field) | [%] |
| x | | |

| | | |
|---|---|---|
| $x$ | Particle diameter | [µm] |
| $d_{33}$ | Piezoelectric coefficient | [pC/N] |
| $d_{ij}$ | Piezoelectric strain coefficient | [pC/N] |
| $x_{pore}$ | Pore size | [µm] |
| $q_3$ | Pore size distribution | [1/µm] |
| $R_1$ | Radius of fluid bridge’s curvation | [µm] |
| $R_2$ | Radius of fluid bridge’s neck | [µm] |
| $d_{33rem}$ | Remanent piezoelectric strain coefficient | [pC/N] |
| $P_{rem}$ | Remanent polarization | [$\mu C/cm^2$] |
| $S_{rem}$ | Remanent strain | [%] |
| $G'$ | Storage modulus | [Pa] |
| $T_S$ | Sintering temperature | [°C] |
| $T$ | Temperature | [°C] |
| $x_{90,3}$ | Volume-based average diameter | [µm] |
| $x_{50,3}$ | Volume-based average diameter | [µm] |
| $x_{10,3}$ | Volume-based average diameter | [µm] |

## Greek symbols

| | | |
|---|---|---|
| $\omega$ | Angular frequency | [rad/s] |
| $\sigma_c$ | Compression strength | [MPa] |
| $\theta$ | Contact angle | [°] |
| $\rho$ | Density | [$g/cm^3$] |
| $\Gamma$ | Fluid’s surface tension | [mN/m] |
| $\beta$ | Half filling angle | [°] |
| $\varepsilon_{max}$ | Maximum relative permittivity (high field) | [-] |
| $\varepsilon_{open}$ | Open porosity | [%] |
| $\alpha$ | Overall porosity | [%] |
| $\varepsilon_{ii}^{\sigma}$ | Permittivity | [-] |
| $\varepsilon_r$ | Relative permittivity | [-] |
| $\varepsilon_{rem}$ | Remanent relative permittivity | [-] |
| $\phi_{sec}$ | Secondary fluid volume fraction | [vol %] |
| $\Psi_t$ | Soil water potential | [MPa] |
| $\phi_{solid}$ | Solid particle volume fraction | [vol %] |
| $\alpha_s$ | Strut porosity | [%] |
| $\varepsilon_s$ | Strut porosity | [%] |
| $\theta_{S,B}$ | Three phase contact angle | [°] |
| $\eta$ | Viscosity | [Pa s] |
| $\sigma_y$ | Yield stress | [Pa] |

# Contents

# 1 General introduction

Ceramic materials exhibit high mechanical hardness and strength, good oxidation and corrosion resistance, good biocompatibility, good stability and operational potential at high temperatures and low thermal expansion. [1–4]

The brittleness of ceramics, however, limits their mechanical damage tolerance. This is a major obstacle to their wide technical applications. To overcome this problem, pores can be incorporated into the structure. The properties of ceramics can be extremely extended in this way. Porous ceramics feature unique structural advantages such as a low density, a high specific surface area, high toughness, good thermal insulation capability, strong thermal shock resistance, low dielectric constant, and improved piezoelectric properties. [1, 2, 5–7]

These special properties open up entirely new possibilities for a whole range of different industrial applications (1) as filters of hot gases from industrial processes removing unwanted particulate matters, as (2) filters for drinking water removing heavy metals, virus and contaminants, (3) as catalyst support for pollutants degradation, environmental remediation, phenol mineralization, and hydrogen production, (4) as energy conversion and storage components in concentrated solar power configurations, solid oxide fuel cell (SOFC) and batteries, (5) as ferroelectric ceramics with incorporated pores for the development of advanced micro-mechanical systems (MEMS) powering small scale electronic devices, (6) as electromagnetic interference (EMI) shielding for commercial wireless communication devices and automobile applications, (7) as advanced construction materials for heat insulation and sound absorption and (8) as bio-mimetic materials, e.g. as bone substitutes. [1, 6, 15, 16, 7–14]

Numerous manufacturing processes for macroporous sintered materials are established. For the range of pore sizes < 10 µm at porosities > 50 % Dittmann *et al.* [17] recently published an innovative and inexpensive manufacturing process. So-called capillary suspensions (CapS) are used as precursors for sintered materials. The process is based on standard unit operations and all common sintered materials can be used. A CapS is an ink consisting of particles (typically $\phi_{solid} < 30$ vol%), a bulk fluid, and a small fraction of an immiscible secondary fluid (typically $\phi_{sec} < 5$ vol%). The capillary forces acting in this ternary solid/fluid/fluid system induce the formation of a self-organized, sample-spanning particle network with high shear modulus and yield stress [18]. Based on the unique rheological flow properties and stable sample-spanning particle network of CapS, innovative product formulations can be developed in a wide range of applications. Formulations range from pastes for ultra-stretchable electronics [19], over electrode slurries for lithium-ion battery electrodes [20] up to silver pastes for solar cell metallization [21].

This thesis focuses on the formulation of CapS as precursors for highly porous sintered materials [22–28]. It focusses on the development of first applications of porous ceramics based on capillary suspensions. This includes first the development and manufacturing of innovative ceramic discs for use in a soil moisture sensor and the subsequent testing and evaluation of the sensor in soil moisture experiments for optimizing irrigation in agriculture. And finally, the tuning of the functional properties of an electroceramic material through 3D printing of highly open porous, hierarchically structured ceramics via direct ink writing (DIW) of CapS-type inks. This way opening up new opportunities in a broad variety of applications, including electromechanical energy harvesting, electrode materials for batteries or fuel cells, thermoelectrics, or bone tissue engineering with piezoelectrically stimulated cell growth.

In this chapter, the properties and economic importance of porous materials for industrial applications in general are discussed. Subsequently, the most important manufacturing routes for highly porous inorganic materials are presented and compared with sintered materials based on the capillary suspension concept developed by Dittmann *et al.* [17, 22]. This concept and the adaptation of the formulation of the CapS for 3D printing of structural ceramics by Maurath *et al.* [24] form the basis for the product formulations developed in this thesis. This chapter closes with an outline and an overview about open questions which will be answered within this dissertation, consisting of two peer-reviewed publications and one peer-reviewed conference proceeding.

## 1.1 State of the art

### 1.1.1 Porous sintering materials

Advanced porous ceramics show an indispensable potential for a wide range of applications especially in energy- and environment- related fields [11]. This is because they exhibit high thermal and chemical resistivity at a high mechanical strength making them feasible for applications in extremely harsh conditions.

The microstructure, i.e. the open and closed porosity, the pore size, the pore orientation, the grain size, the degree of sintering and the hierarchical structure has to be carefully adapted to the demands of the respective application as they define the mechanical properties and advanced functionalities of the porous ceramics [1, 2].

Typically, porous materials can be classified into three main categories depending on the pore size: microporous ($x_{pore} < 2$ nm), mesoporous (2 nm $< x_{pore} < 50$ nm), and macroporous ($x_{pore} > 50$ nm) materials [1]. The commonly used term *hierarchical pore structure* refers to the coexistence of a combination of pores of different sizes spanning several length scales in a single ceramic matrix. Furthermore, the pore structure of porous ceramics can be divided into open and closed pores. Open pores are interconnected in the ceramic matrix, and closed pores are isolated.

The four most common manufacturing techniques for porous ceramics are *partial sintering*, the *replica technique*, the *sacrificial template method* and *direct foaming*. In addition, *additive manufacturing* (AM), as an emerging technology, offers great potential for the production of porous ceramics, as it opens up new possibilities in all fields. As shown in Figure 1.1, depending on the choice of manufacturing method, the microstructure, i.e. the porosity and the pore size can be adjusted within a certain range.

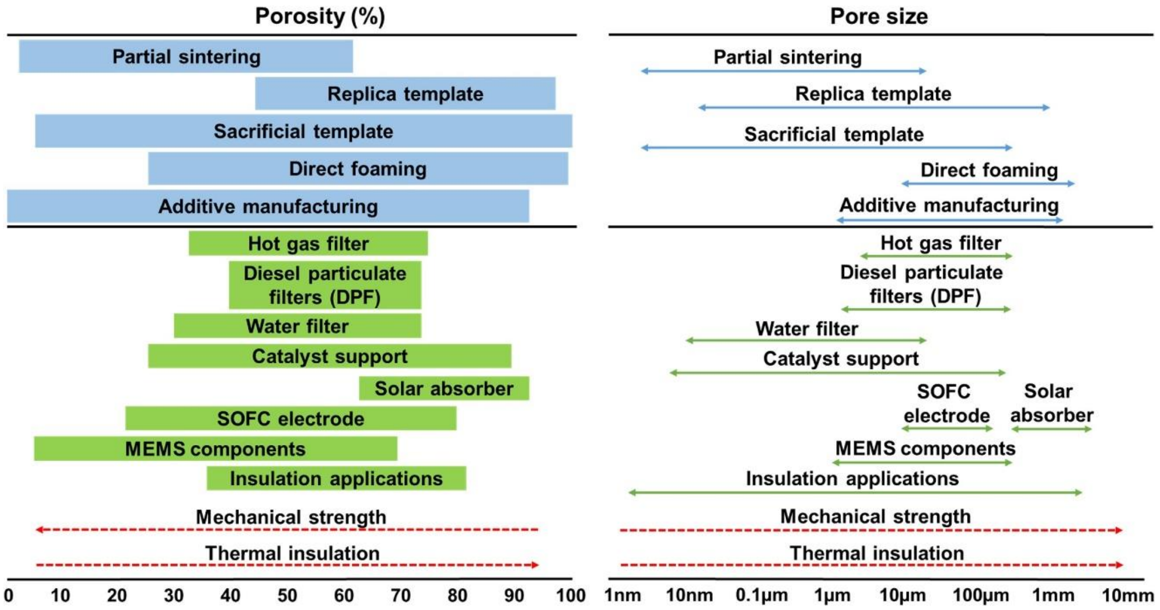

Figure 1.1 The porosity and pore size distribution features of porous ceramics that can be created by techniques such as partial sintering, replica template, sacrificial template, and direct foaming. Each type of porous ceramic has its own specific features regarding microstructure and application properties. Reproduced with permission [11]. *Copyright © 1969, Elsevier.*

In the following paragraphs these four most common manufacturing techniques for porous ceramics are introduced. Figure 1.2 schematically visualizes the main processing steps of the four manufacturing techniques.

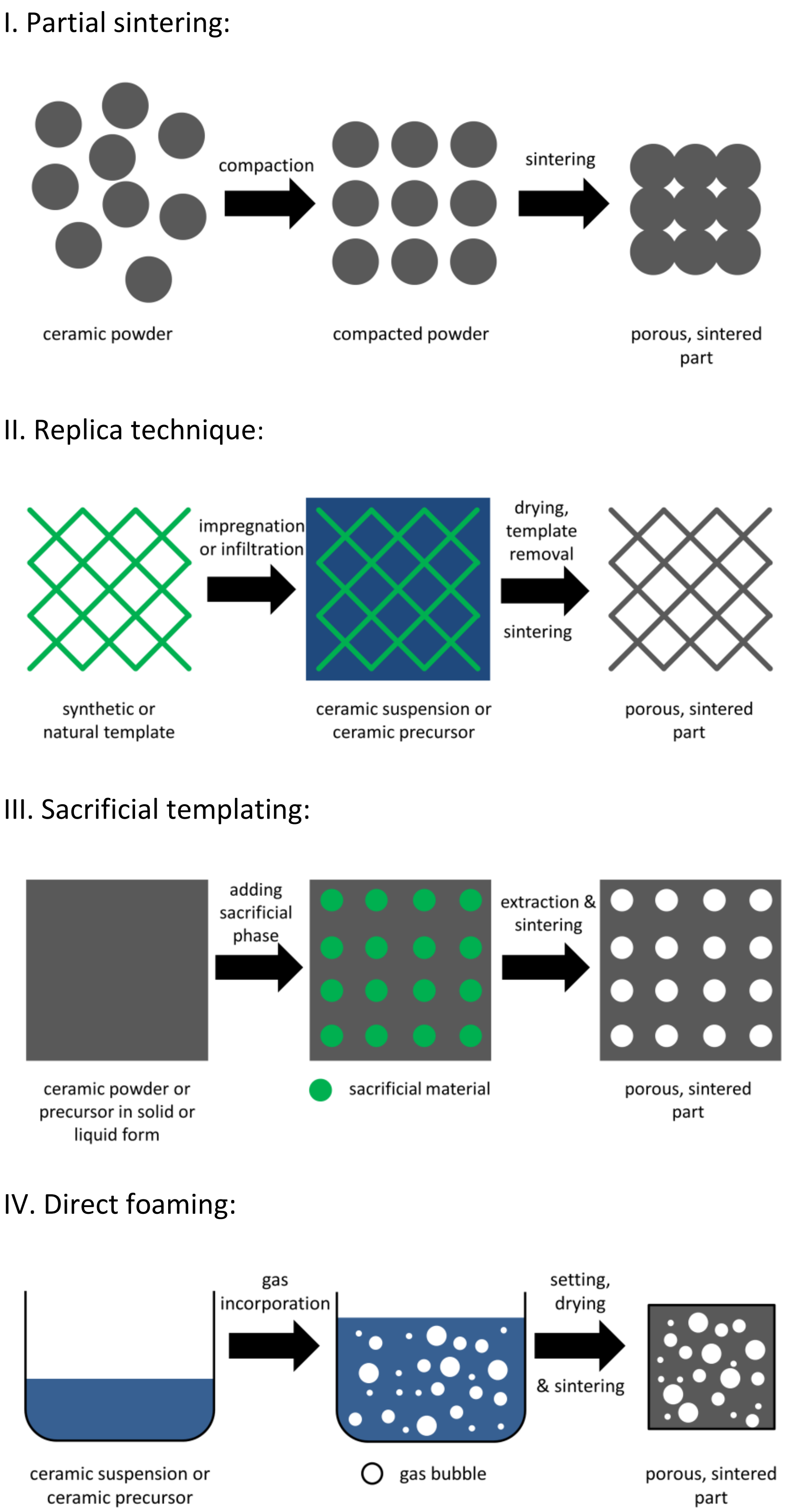

I. Partial sintering:

II. Replica technique:

III. Sacrificial templating:

IV. Direct foaming:

Figure 1.2 Schematic of the four major processes for manufacturing macroporous sintering materials (adapted with permission from [2, 29]). *Copyright © 2006 The American Ceramic Society*

The most widely used and employed process for the production of porous sintered materials is *partial sintering*. In this process, powdered solids are pressed into a mold and the resulting green body is subsequently sintered until the desired porosity is reached. The starting powders and the sintering conditions mainly determine the microstructure of the porous ceramic. The pore size distribution can be adjusted by the particle size and particle size distribution used. The porosity, on the other hand, is adjusted by not only the particle size distribution used, but also the molding pressure and temperature treatment applied. Generally, porosities $< 50\ \%$, macropores with diameters between $50\ \text{nm} < x_{\text{pore}} < 10\ \mu\text{m}$, a narrow pore size distribution and an interconnected open porosity are obtained. [1, 11]

With the *replica technique* open porous ceramics can be manufactured using the porous structure of an organic template. The templates are first infiltrated with a ceramic slurry, then dried, thermally debinded and sintered. During the thermal treatment, the organic template is decomposed while the ceramic remains. Finally, porous ceramics are obtained that replicate the structure and morphology of the organic template. Using this technique porosities up to 95 % and pore sizes $10\ \mu\text{m} < x_{\text{pore}} < 3\ \text{mm}$ can be reached depending on the template used. [2, 6, 11, 30]

In the *sacrificial template* method, a disperse phase is mixed into a ceramic suspension or a ceramic precursor (in solid or liquid form). The disperse phase is subsequently removed via evaporation, pyrolysis or extraction. This way, the removed dispersed phase forms the macropores. Finally, the porous ceramic or preceramic framework is sintered. Therefore, the sacrificial template method differs from the replica technique in that the latter replicates the original configuration of the template, while the former creates a negative replica of the original pore features. Both open and closed pores can be created using the sacrificial template method. Both natural and synthetic organic materials, but also metals or salts, can be used as sacrificial templates in this method. Due to this variety of different materials, the porosity can be adjusted between 20 and 90 % with pore sizes ranging from $1\ \mu\text{m} < x_{\text{pore}} < 700\ \mu\text{m}$. [11, 31, 32]

*Freeze casting* is related to the sacrificial templating method. In this method a frozen liquid is used as a template to create pores. To obtain a frozen liquid, ceramic suspensions are subjected to a directional cooling process. This allows the frozen suspension to be subsequently removed by directional sublimation, resulting in macroporous ceramics with unidirectionally aligned pores. This way, porosities $> 50\ \%$ are possible. [11, 33–35]

In the *direct foaming* process, a ceramic suspension is foamed using a gaseous dispersion phase consisting of air or inert gases. For stabilization of the gas bubbles the suspension contains surfactants. Theses prevent the coalescence of the gas bubbles in the foam due to a reduction of the interfacial tension between the gas and liquid. After subsequent drying of the foam, thermal debinding and sintering take place. In this way, porous ceramics with porosities of up to 97% can be manufactured with both open and closed pores with sizes $x_{pore} > 10$ µm. [2, 36–39]

The named processes cover a wide range of achievable porosities and pore sizes, which are summarized in Table 1. None of these methods provides a straightforward route for manufacturing macroporous ceramics with porosities > 50 % and pore sizes $x_{pore} < 10$ µm. Porous ceramics based on CapS could fill this gap [17, 22–25, 27, 28, 40–42].

Table 1 Methods for producing macroporous ceramics with corresponding pore size $x_{pore}$ and porosity (adapted from [17])

| **method** | **$x_{pore}$ / µm** | **porositiy / %** |
|---|---|---|
| Partial sintering | < 10 | < 50 |
| Replica technique | 10 - 3000 | 25 - 95 |
| Sacrificial templating | 1 - 700 | 20 - 90 |
| Direct foaming | 10 – 1200 | 40 - 97 |

## 1.1.2 Highly porous ceramics based on capillary suspensions

A Capillary Suspension can be formed by adding a secondary fluid to a two-phase suspension consisting of solid particles suspended in a bulk fluid, where the secondary and bulk fluid have a miscibility gap. Characteristic for this material is an overall structure consisting of a percolated network of particles, connected by attractive capillary interactions induced by the secondary fluid. Due to the particle network, CapS exhibit high shear modulus, high yield stress and shear thinning behavior [18, 22]. The rheological properties of the suspension can be tuned from liquid or weakly elastic to gel-like by changing the fraction of secondary fluid (see Figure 1.3 (A)) [17]. In addition, the suspension is stabilized in this way, as the network caused by the capillary force prevents the sedimentation of particles [18].

Two types of CapS are defined: In the *pendular state* the secondary fluid wets the solid particles better than the bulk fluid ($\theta_{S,B} < 90°$) and forms concave bridges between the particles (see Figure 1.3 (B)). In the *capillary state* the secondary fluid does not wet the solid particles ($\theta_{S,B} > 90°$) and no bridges are formed, but particles aggregate to form small, e.g. tetrahedral or octahedral clusters. [43–45] In this thesis, we will focus on CapS in the *pendular state* since the material systems used within in this work are in this state.

The capillary force holds the particle network together. In order to understand this force acting in the pendular state, a liquid bridge between two spherical particles in air can be considered in a simplified manner (see Figure 1.3 (C) and (D)).

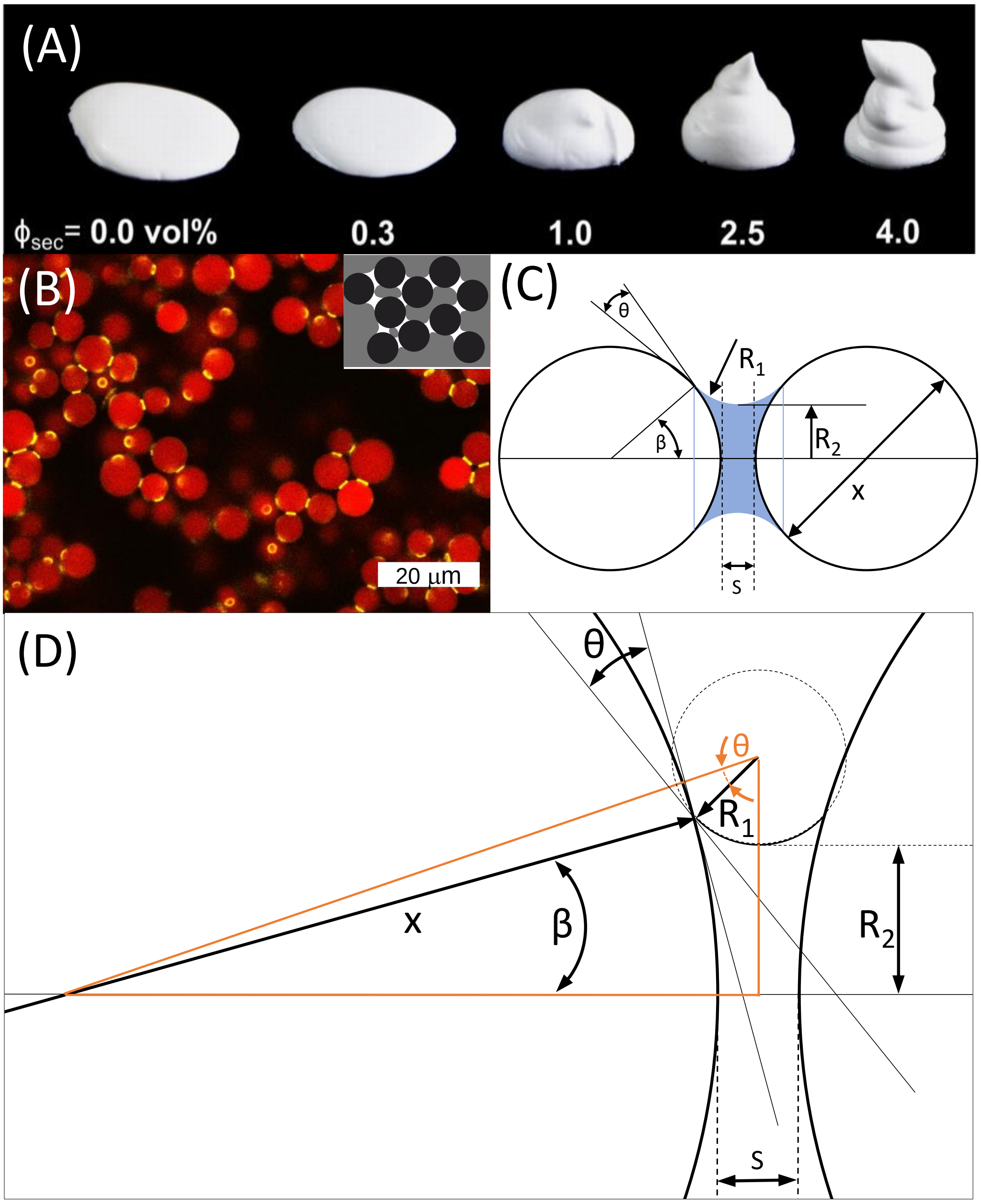

Figure 1.3 (A) Transition from liquid to weakly elastic to gel-like state by adding an appropriate amount of secondary fluid to an oil-based alumina suspension (α-$Al_2O_3$; $x_{50,3}$ = 5.67 µm; $\phi_{solid}$ = 20 vol%). The secondary fluid is an aqueous sucrose-solution (50 vol%). Adapted with permission from [17]. *Copyright © 2012 The American Ceramic Society*. (B) Confocal image of silica ($x_{50,3}$ = 6.43 µm) based CapS in pendular state and in the top right corner a schematic of a pendular article network. Solid particles are shown in red, secondary fluid in yellow, and undyed nonpolar bulk fluid as black regions. Adapted with permission from [44]. *Copyright © 2016 The American Ceramic Society*. (C) Schematic of a pendular state capillary bridge between two spherical particles and (D) schematic of the angle relation.

Here, θ is the contact angle between secondary liquid and solid particles, $R_1$ the radius of curvature of the fluid bridge, $R_2$ the radius of fluid bridge's neck, x the particle diameter, β the half filling angle and S the distance between the two spherical particles. With the fluid's surface tension Γ the capillary force $F_c$ can be calculated (see equation (1)) [46].

$$F_C = \pi\, x\, \Gamma\, sin\beta \left[ \underbrace{\sin(\beta + \theta)}_{I} + \underbrace{\frac{x}{4}\left(\frac{1}{R_1} - \frac{1}{R_2}\right)\sin\beta}_{II} \right] \tag{1}$$

With the parameters used as labeled in Figure 1.3 (C) equation (1) is valid only for zero particle distance S = 0. The capillary force consists of two parts: an axial component of the surface tension acting at the liquid-gas interface (I) and the Laplace pressure acting inside the fluid bridge (II). Typically, the second term is much larger than term I, further assuming that $R_1 << R_2$ equation (1) reduces to equation (2) [47–49]:

$$F_C = \pi\, x\, \Gamma\, \sin\beta\, \underbrace{\frac{x}{4}\frac{1}{R_1}\sin\beta}_{II} = \pi\, \Gamma\, \frac{x^2}{4}\frac{1}{R_1}\sin^2\beta \tag{2}$$

Assuming S = 0, equation (3) can be formed using Pythagoras, and with $R_1 << R_2$ it reduces to equation (4):

$$\left(\frac{x}{2}\right)^2 + (R_1 + R_2)^2 = \left(\frac{x}{2} + R_1\cos\theta\right)^2 \tag{3}$$

$$R_1 = \frac{{R_2}^2}{x\cos\theta} \tag{4}$$

With the same assumption of S = 0, the sine angle relation can be formed to equation (5) and simplified with R1 << R2 to equation (6):

$$\sin\beta = \frac{R_1 + R_2}{\frac{x}{2} + R_1\cos\theta} \tag{5}$$

$$\sin\beta = \frac{R_2}{\frac{x}{2}} \tag{6}$$

Inserting equation (4) & (6) in equation (2) it reduces to equation (7):

$$F_C = \pi\, x\, \Gamma\cos\theta \tag{7}$$

In the context of CapS [17, 47] this simplified equation is often used to illustrate the main factors that can be influenced during paste formulation. The rheological behavior of CapS have already been studied in detail and the theoretical correlations between yield stress and material properties have been explained [22, 25, 44, 47]. Equation (8) describes a simplified version of the yield stress $\sigma_y$ of a capillary suspension with the assumption of two spherical particle with diameters of equal size, and the boundary conditions of a distance of S = 0 between the spherical particles [22, 25, 47].

$$\sigma_y = f(\phi_{solid}, N_{bridge})\, g(V_{bridge})\, \frac{4\,\pi\,\Gamma\cos\theta}{x} \tag{8}$$

Here, $f(\phi_{solid}, N_{bridge})$ is a function of the solid content and the number of capillary bridges and $g(V_{bridge})$ a function of the bridge volume. Both functions are not yet fully described. Investigations regarding these functions and the influence of individual parameters on the yield stress can be found in [17, 25, 44, 45, 47, 50, 51], but will not be elucidated in more detail here.

Dittmann *et al.* [17, 22] used the CapS phenomenon to develop an innovative processing route for manufacturing open porous ceramics with porosities higher 50 % at pore sizes lower 10 µm by using ceramic particles as solid phase in the suspension. Here, the CapS with a stable percolated particle network acts as precursor for the porous sintered parts. The network can be preserved during debinding and sintering making completely open porous sintered structures accessible. The main processing steps are schematically shown in Figure 1.4. A small amount of second phase is added to a regular ceramic suspension with a solids content of solid $\phi_{solid}$ = 10 - 30 vol%. After a homogenization step, the CapS can be shaped by casting, extrusion or 3D printing, for example. This is followed by mechanical debinding, i.e. the removal of a large part of the bulk phase by using adsorbing supports or porous substrates or by applying solvent extraction. By adding a binder dissolved in the second phase (e.g. sucrose), the capillary bridges are solidified as soon as volatile component of the second phase is removed by evaporation. This especially helps to form a stable green body and to safely handle it. After mechanical debinding, the green bodies are thermally treated. In this process, all organic components are pyrolyzed during thermal debinding and subsequently, the ceramic body is sintered. In the end, fully open porous ceramics with unprecedented porosities (> 50 %) and pore size (0.5 µm < $x_{pore}$ < 50 µm) specifications can be produced using this processing route.

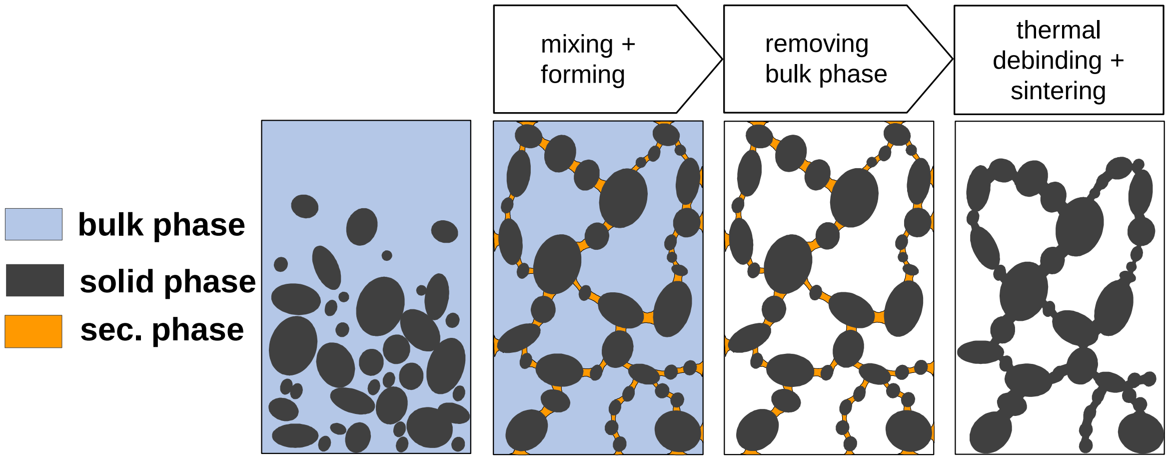

Figure 1.4 Flow sheet with the main process steps for porous sintering materials based on CapS [17, 52].

The ceramics manufactured with the processing route described by Dittmann *et al.* [17, 22] are mostly based on paraffin oil as bulk fluid, $Al_2O_3$ as solid particles and an aqueous sucrose solution as secondary phase. Whereby he specifies that also other ceramics (silicon dioxide, tricalcium phosphate, titanium dioxide), other bulk phases (paraffin oil, paraffin wax, decanol, octanol and diisononyl phthalate) and other secondary phases (glycerine, polyvinyl alcohol, polyvinyl pyrrolidone and polyethylene glycol) can also be used. Dittmann *et al.* [17, 22] used the $Al_2O_3$ system to investigate the rheological properties of the Caps and the microstructure (porosities, pore size distributions and mechanical strength) of this sintered material with a variation of the solid fraction ($\phi_{solid}$ = 10 - 30 vol%) and a variation of the secondary phase ($\phi_{sec}$ = 0 - 4 vol%).

Dittmann *et al.* [17, 22] presented a three regime model describing the changes in the network structure depending on the second phase volume fraction. The network structure corresponding to the three regimes can be visualized by the microstructure of the sintered ceramics using scanning electron microscope (SEM) images (see Figure 1.5). in regime I, the transition from a suspension to a structure with a weak particle network to a fully developed paste-like CapS (regime II) takes place. Regime II is characterized by a homogeneous structure of the particle network, which can only be achieved with a very specific amount of secondary phase. Regime III is achieved by using slightly more secondary phase. This regime is characterized by increasing inhomogeneities, which are dominated by spherical agglomerates, which destabilize the network. With increasing second-phase content, the average pore diameter $x_{50,3}$ increases in this case from about 10 to 50 µm (here, determined via image analysis: Line Intercept Count Method – see Figure 1.5). But not only the average pore size is affected by the changed network, also the pore size distribution $q_3$. In regime (I), a monomodal pore size distribution is present, in (II) a second, somewhat larger characteristic pore size occurs which leads to a bimodal distribution, and finally in regime (III) a broad multimodal pore size distribution is present (see Figure 1.5) [22].

By adjusting the material type, particle size, solid fraction and secondary phase fraction, both the rheological properties of the CapS and the properties of the sintered components such as porosity, pore size and pore size distribution can be specifically tailored.

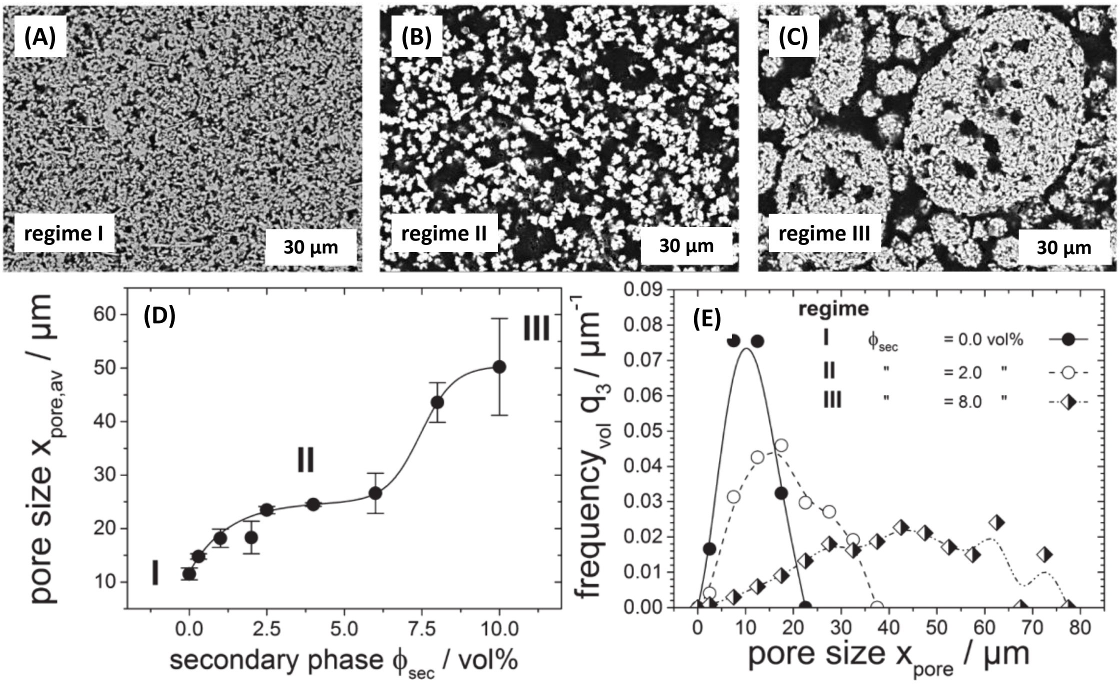

Figure 1.5 (A)-(C) Three regime model for CapS illustrated via appropriate SEM crosscut image (solid particles appear light gray and pores black) of sintered capillary suspensions; (D) Average pore size $x_{pore,av}$ plotted versus the amount of secondary fluid; (E) the resulting pore size distribution $q_3(x_{pore})$ for different amounts of secondary fluid ($\alpha$-$Al_2O_3$; $x_{50,3}$ = 5.67 µm; $\phi_{solid}$ = 20 vol%). Adapted with permission from [22]. *Copyright © 2012 The American Ceramic Society.*

Maurath [24] combined the principle of CapS with additive manufacturing by printing $Al_2O_3$ based CapS inks using DIW, also referred to as robocasting. The special properties of CapS, such as the high yield stress, the pronounced shear thinning and the rapid structure recovery, are of decisive advantage here compared to other formulations, since it enables the printing of complex 3D bodies with large span ratios [47, 53]. With an adapted composition, Maurath succeeded in manufacturing cellular structures (log-pile and honeycomb structures, see Figure 1.6) with debinding and sintering the structures crack-free. Whereby the printed structures always had the µm pores of the CapS ceramics with fully open porosity. With the paste composition produced [24], it was possible to work with nozzle diameters in the range of 200-650 µm for extrusion. Due to the properties of CapS it was possible to achieve a strut/pore ratio of approx. 1:1 (490-634 µm strut and 490-570 µm pore diameter). Maurath named filtration processes in hot gas applications or the use of these structures as catalyst supports with smart flow channels for fast chemical reactions as potential areas of application.

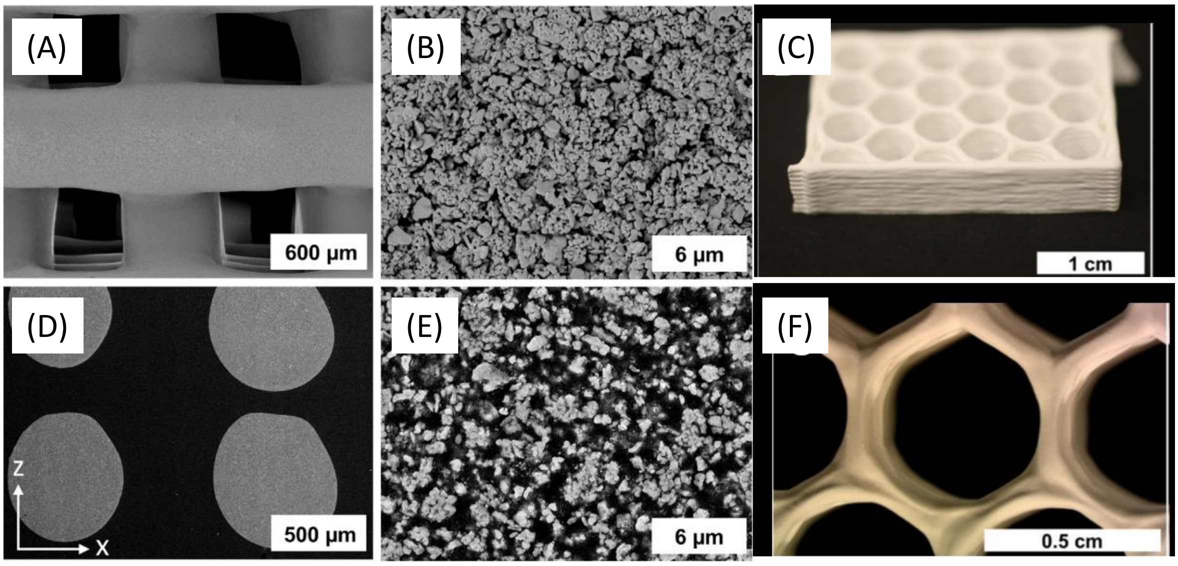

Figure 1.6 SEM images of sintered log-pile structures based on CapS (α-$Al_2O_3$; $x_{50,3}$ = 0.5 µm, printed with a 610 µm nozzle). (A) Top view, (B) magnified surface of filament, (D) Crosscut image of printed filament and (E) crosscut image of microstructure of sintered CapS. (C) and (F) Images of sintered hexagonal honeycomb structures, printed with a 200 µm nozzle. Adapted with permission from [24]. *Copyright © 2017 Elsevier.*

In [23] Dittmann *et al.* modified the concept of CapS to advanced or smart CapS. They mention, that it is possible to tune the properties such as the mechanical strength of the $Al_2O_3$ ceramic system by adding suitable active ingredients to the particle contact zones using the secondary fluid as transport medium. Finally, they achieve the improved ceramic properties by adding t-$ZrO_2$ as fine powder fraction to the original $Al_2O_3$ CapS composition (see Figure 1.7). This mixed material composition resulted in an increase of flexural strength by a factor of 2.5 and of compressive strength by a factor of almost 3.5 compared to the monomodal α- $Al_2O_3$ coarse powder preparation. This effect is due to the mixed phase of the particles that forms at the particle contact points during the sintering process, but not because it was added to the secondary fluid.

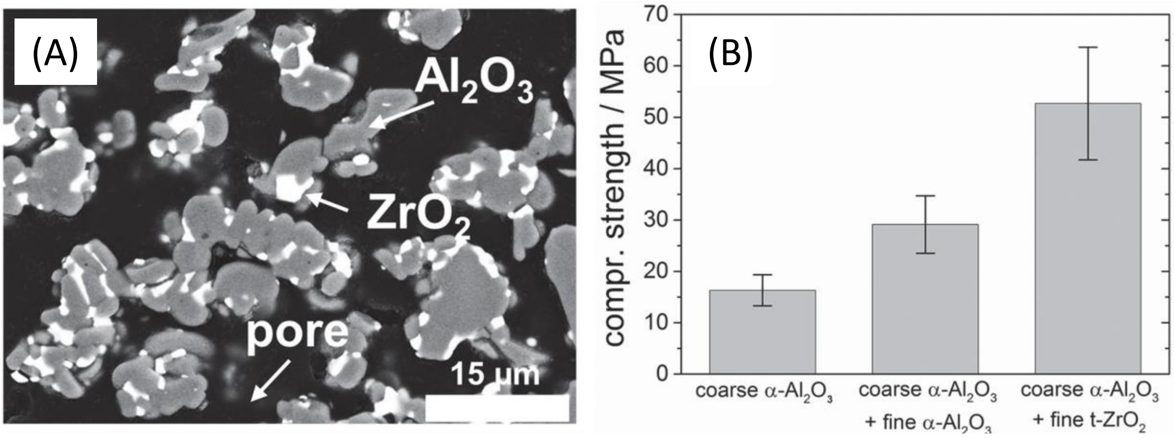

Figure 1.7 SEM crosscut image and mechanical properties of sintered CapS made from different powder compositions. (A) Powder mixture of α-$Al_2O_3$ and t-$ZrO_2$ (t-$ZrO_2$ appears white and α-$Al_2O_3$ grey). Compression strength of corresponding sample with a porosity of approx. 55 %. Adapted with permission from [23]. *Copyright © 2016 Wiley-VCH Verlag GmbH & Co. KGaA*

Weiß *et al.* [28] combined the works of Maurath [24] and Dittmann *et al.* [23] by 3D printing CapS with nanoparticles included in the secondary phase. Here, the nanoparticles are exclusively deposited at the contact regions between coarse particles (see Figure 1.8). This way the compressive strength increased by a factor of 2.0 for porosities of 51 % and an increase by a factor of 5.0 for porosities of 70 %. The finest achieved structure showed a density of 192 kg/m³ with a compressive strength of 4.0 MPa, which is very close to the specific strength values of balsa wood. With the paste composition produced by Weiß *et al.* [28], 200 and 410 µm nozzle diameters were used for 3D printing resulting in 327 and 527 µm sintered strut diameters. The increased strut width beyond the nozzle diameter might be related to material overflow during extrusion [24]. In this work, only honeycomb structures were manufactured to evaluate the compressive strength. No strut size to pore size ratios were investigated. Therefore, no strut size to pore size ratios have been documented so far for the pastes made from CapS with incorporated nanoparticles. According to Weiß *et al.* [28] the designed lightweight materials could be used in high temperature catalytic applications or as filters in chemically harsh environments, but also as construction and/or thermal insulation materials.

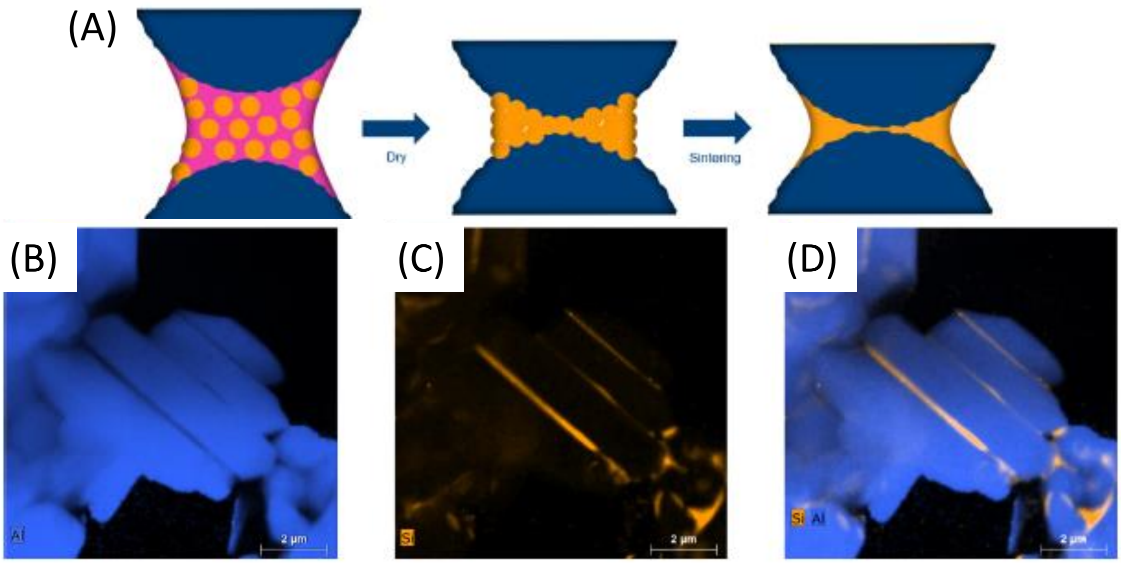

Figure 1.8 (A) Schematic sintering neck formation with incorporated nanoparticles. (B-D) TEM-EDXS mappings of sintered CapS using α-$Al_2O_3$ as solid phase and silica nanosuspension as secondary phase. Dark areas represent vacuum-, yellow areas Si-, and blue areas Al regions. (B) showing only Al fractions, (C) only Si fractions and (D) showing both mapped elements. Adapted with permission from [28]. *Copyright © 2020 Elsevier.*

# 2 Motivation and manuscript outline

In the previous chapter, an innovative concept for the manufacturing of porous ceramics using CapS was presented. This process allows the properties of macroporous ceramics to be tailored in a range, which cannot be achieved with the conventional methods described before (see Figure 2.1). In particular, the range of porosities > 50 % and small pore sizes $x_{50,3} < 10$ µm is not covered by the conventional manufacturing methods. Here, the manufacturing of ceramics using CapS as precursors comes into play as porosities between 20 and 80 % with pore sizes between 0.5 and 50 µm can be flexibly adjusted with this approach: the experimental data from previous work are collected and shown as orange stars for CapS and as half-filled orange stars for CapS with incorporated nanoparticles. Showing this novel process has great potential to close precisely the previously existing gap in manufacturing porous ceramics.

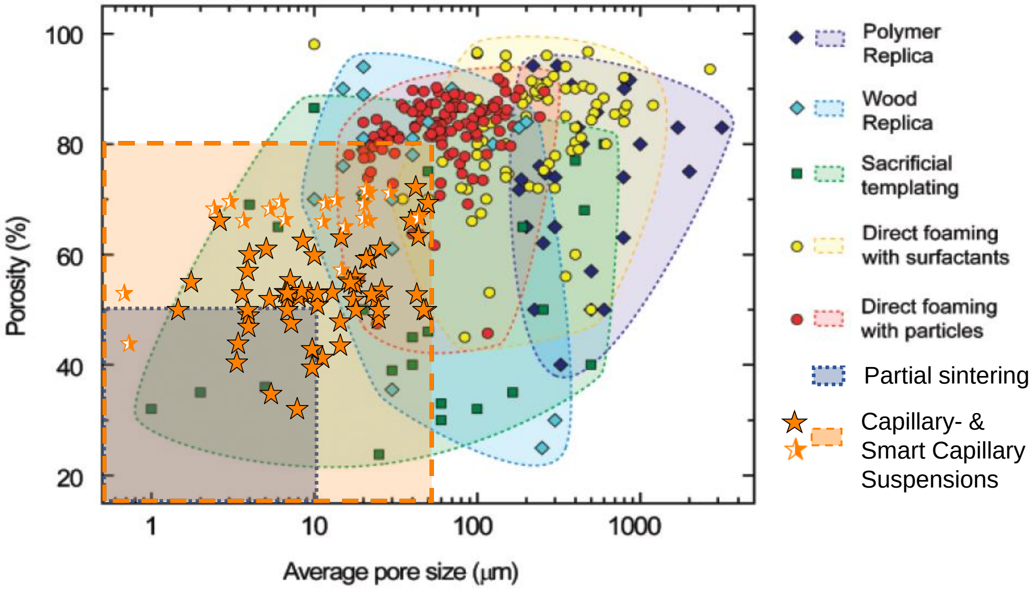

Figure 2.1 Porosities and pore sizes achieved by common manufacturing routes for macroporous ceramics and the capillary suspension method. Adapted with permission from [2, 28, 54]. *Copyright © 2006 The American Ceramic Society.*

In addition to the parameter range mentioned above, the use of CapS in 3D printing offers new possibilities to open up pore size ranges previously not reached by CapS. In this way, printed pores in the range of > 50 µm could be achieved using CapS.

Investigations on porous ceramics from CapS so far have mainly been carried out to determine the rheological properties of the ceramic pastes [17, 25], the structural properties of the porous structural ceramics [22, 26, 27] and how the structural properties can be improved [23]. In addition, different molding methods such as 3D printing for CapS were investigated [24, 28]. Up to now, there is no literature about CapS based ceramic products which were developed up to market readiness. In addition to that, there is no literature about CapS based functional ceramics. In addition to CapS based structural ceramics, the development of CapS-based functional ceramics may open up a whole new world for applications in the field of mechanical and thermal energy conversion, electromechanical energy harvesting or bone tissue engineering with piezoelectrically stimulated cell growth.

In this thesis, the step of research to business for ceramics based on CapS will be done for the first time. To achieve this, the properties such as pore size distribution and porosity of a CapS-based ceramic are extended to previously unreached ranges. In addition, the CapS phenomenon will be applied to a piezoelectric ceramic material for the first time, which will also be 3D printed. The following main part of this thesis consists of two peer-reviewed scientific journal articles and one peer-reviewed conference proceeding which may be divided into two sections:

I. Application: soil water potential sensor
II. 3D printing of functional ceramic

Section I includes one peer-reviewed publication and one conference proceeding, while section II includes one peer-reviewed publication. The publications in **section I** discuss the development [41] and testing of a novel soil water potential sensor to optimize irrigation in agriculture [42] and can be found in **chapter 3**. The project was a collaboration with TRUEBNER GmbH, a manufacturer of soil moisture sensors. The construction of the sensor includes on the one hand the development of a ceramic based on capillary suspensions with a pore size distribution as wide as possible and a porosity as high as possible with a sufficiently high mechanical strength and on the other hand the development of a suitable sensor board by TRUEBNER GmbH. For the testing of the sensor, a large number of laboratory and field experiments were carried out in a wide range of soil types in order to demonstrate the versatility of the sensor.

In **section II**, the CapS phenomenon is applied for the first time to an electroceramic material and can be found in **chapter 4**. The properties of the CapS are adapted in such a way that previously unreached minimum strut diameters and previously unreached span ratios are achieved for the DIW process. By combining the structural properties of the CapS with a printed structure using additive manufacturing, the piezoelectric and electromechanical properties are tuned to a previously unattained level.

# 3 The Soil Water Potential Sensor

## 3.1 A Robust Soil Water Potential Sensor with High Sensitivity and Broad Measuring Range

Full titel: A Robust Soil Water Potential Sensor with High Sensitivity and Broad Measuring Range

Authors: David Menne, Christof Hübner, Dennis Trebbels, Norbert Willenbacher

Status: published [41]

Bibliographic data: *2021 13th International Conference on Electromagnetic Wave Interaction with Water and Moist Substances (ISEMA)*, 2021, pp. 1-7, doi: 10.1109/ISEMA49699.2021.9508320.

**Abstract**

Agriculture is by far the largest consumer of water worldwide. Soil moisture sensors contribute to the sustainable use of this scarce resource. So far, these devices only measure how much water is present in the soil. The decisive factor, however, is how much water the plants can draw from the soil with their roots, which depends heavily on the composition of the soil. This is the reason why we developed a novel sensor for soil water potential (SWP) measurement. The sensor consists of a highly porous ceramic disc and a new circuit board system for detecting the change in dielectric response of the ceramic discs with changing water uptake. The ceramic was tailored using a novel processing route [17], based on so-called capillary suspensions as precursors, allowing the production of highly open-porous ceramics with characteristic pore size distribution and high mechanical strength. Two different kieselguhr powders were used as ceramic sintering material because they allowed the reproducible fabrication of defect-free sensor discs with high shape accuracy at low sintering temperatures. Ceramic discs with open porosities ranging from 58 to 69 % and broad pore size distributions with pore sizes ranging from 0.5 to 200 µm were manufactured for this new sensor. Drying experiments were carried out in air, in a model soil and in field experiments demonstrating the feasibility and improved sensitivity of the setup.

## 3.2 Robust Soil Water Potential Sensor to Optimize Irrigation in Agriculture

Full titel: Robust Soil Water Potential Sensor to Optimize Irrigation in Agriculture

Authors: David Menne, Christof Hübner, Dennis Trebbels, Norbert Willenbacher

Status: published [42]

Bibliographic data: *Sensors 2022, 22, 4465*.doi: 10.3390/s22124465

**Abstract**

Extreme weather phenomena are on the rise due to ongoing climate change. Therefore, the need for irrigation in agriculture will increase, although it is already the largest consumer of this valuable resource. Soil moisture sensors can help to use water efficiently and economically. For this reason, we have recently presented a novel soil moisture sensor with high sensitivity and a broad measuring range. This device does not measure the moisture in the soil, but the water available to plants e.g. the soil water potential (SWP). The sensor consists of two highly porous (> 69 %) ceramic discs with a broad pore size distribution (0.5 to 200 µm) and a new circuit board system using a transmission line within a time-domain transmission (TDT) circuit. This detects the change in dielectric response of the ceramic discs with changing water uptake. To prove the concept, a large number of field tests were carried out and comparisons were made with commercial soil water potential sensors. The experiments confirm that the sensor signal is correlated to the soil water potential irrespective of soil composition and is thus suitable for the optimization of irrigation systems.

## 3.3 Introduction

Global climate change continues to progress. In the year 2020 global temperatures tied record highs [55]. For this reason, too, even more urgent attention must be paid to the waste of water and the associated consequences for the water supply of mankind. Agriculture is responsible for > 70% of water consumption worldwide [56, 57]. At the same time, water losses of > 50 % are state of the art in this sector. Accordingly, this is where the leverage for sustainable and efficient water use is greatest and of crucial importance for mankind. [58, 59]

A sustainable use of the worldwide available water resources is only possible using modern monitoring and control techniques. Especially due to increasing conflicts of objectives such as between environmental protection and crop production [60]: on the one hand, the washing out of nutrients is to be prevented by a sustainable water supply, on the other hand, ever-increasing quality demands require an ever more intensive cultivation [61]. The technology of irrigation systems has already reached a high level. However, the associated measurement systems for determining soil moisture in agriculture are limited [62–64].

To determine the water content of a soil one possibility is to use the water retention curve. The water retention curve relates the volumetric water content to the soil water potential $\Psi_\mathrm{t}$, (SWP), i.e. the specific potential energy of water in the soil. The SWP can be expressed as the sum of normalized forces acting on the water in the soil (see equation (9))

It includes the gravitational- ($\Psi_\mathrm{g}$), matric- (capillary and adsorptive, $\Psi_m$), osmotic- ($\Psi_o$) and hydrostatic potential ($\Psi_h$). All forces emanating from the soil matrix are summarized in the matric potential [59].

$$\Psi_\mathrm{t} = \Psi_\mathrm{g} + \Psi_m + \Psi_o + \Psi_h \tag{9}$$

The SWP does not indicate the volumetric water content, but the fraction of water available to plants. Therefore, soil water potential sensors are not only essential for the most efficient use of water in agriculture, but for Earth system models [65]. Most common sensors for measuring the soil water potential are piezometers, tensiometers, heat dissipation sensors, thermocouple psychrometers, and dielectric sensors [59]. Advantages and disadvantages of the individual devices are summarized in [66]: classic tensiometers have a limited measurement range and require frequent maintenance, heat dissipation sensors have a high power consumption and a slow reaction time. In contrast, dielectric sensors are inexpensive, require little maintenance and have low power consumption [66]. Only a few sensors described in literature are commercially available and the market is dominated by a small number of devices (see Table 1) [62–64]. For further information on commercially available sensor systems see [64]. In addition to the mentioned commercially available sensors, Whalley [67–69] developed a porous matrix sensor which shows a measuring range from 500 hPa to 3000 hPa. Recently a few new sensors have been introduced in the literature, which could market launch in the near future [67, 70, 79, 71–78].

Table 3.1 Commercially available Sensor systems. All information according to the respective manufacturer.

| system name | manufacturer | measuring range | approx price | source |
|---|---|---|---|---|
| TEROS 21 (former MPS-6) | METER Group, Inc. (Pullman, WA, USA) (former Decagon Devices, Inc.) | 90 to ∞ hPa | 250 € | [80] |
| Watermark (granular matrix) | Irrometer Company, Inc. (Riverside, CA, USA) | 0 to 2000 hPa | 70 € | [81] |
| EQ3 Equitensiometer | Delta-T Devices Ltd. (Burwell, Cambridge, United Kingdom) | 0 to 10,000 hPa | 800 € | [82] |
| Tensiomark (0-7) | EcoTech Umwelt-Meßsysteme GmbH (Bonn, Germany) | 1 to 10,000,000 hPa | 650 € | [83] |
| Full Range (Polymer-) Tensiometer | Wageningen University (Wageningen, Netherlands) | 0 to 15,000 hPa | 1000 € | [84–86] |

In conclusion, a sensor is still needed which offers a low-cost alternative, covers the whole measuring range from very dry soils often addressed in soil science to very wet soils relevant in agriculture, and offers good performance in saline, vertic and stoney soils [62].

Our sensor principle is based on the high-frequency measurement of the dielectric constant of a porous ceramic disc, which is in hydraulic equilibrium with the surrounding soil [87]. Depending on the water potential of the soil, water is transported into or out of the ceramic. The water content in the disc is determined from the resonance frequency of the electrical resonant circuit. In order to achieve a large measuring effect over a wide range of matric potential, the ceramic has a particularly high pore volume and a broad pore size distribution. By measuring the dielectric permittivity of the porous ceramic disc, the water potential is determined. In this way, the water potential of the soil can be calculated using correlation functions for standard soils.

The main component of our dielectric sensor are two highly porous ceramic discs. The ceramic has pore sizes between 0.5 µm and 200 µm, with an open porosity of well over 60 % and a sufficiently high mechanical strength. This is enabled by using so-called capillary suspensions as precursor for the production of highly porous ceramics. Capillary suspensions are ternary solid/fluid/fluid systems consisting of microscopic particles suspended in a main liquid and a small proportion of an immiscible secondary liquid. The capillary forces inferred by the secondary liquid trigger the formation of a sample spanning particle network. The particle network, stabilized by the strong capillary forces, remains largely intact even after the main liquid has been removed, so that highly porous green bodies can be formed. These green bodies are then sintered to produce open-pore ceramic parts. With this concept, pore shape, pore size distribution, porosity, and mechanical strength can be adjusted over a wide range by varying particle type, size, and shape. [22, 23, 25]

## 3.4 Materials and Methods

### 3.4.1 Raw materials

The raw powder used to fabricate the ceramic discs were commercial grade brown kieselguhr with a volume-based particle diameter $x_{50,3}$ of 12.0 µm and a density of 2.57 g/cm$^3$ and white kieselguhr with a $x_{50,3}$ of 33.5 µm and a density of 2.24 g/cm$^3$ (VWR International GmbH, Karlsruhe, Germany). The initial particle size distribution of the employed powders and soils was determined according to DIN EN ISO 8130-13 using a commercial Fraunhofer diffraction device (Helos H0309; Sympatec, Clausthal-Zellerfeld, Germany) equipped with an ultrasonic wet dispersing unit (Quixel, Sympatec) and sieve analysis. The particle size distribution of both kieselguhr systems, Figure 3.1., was broad, but monomodal. The bulk phase used to fabricate the ceramic discs was odorless mineral spirits, (Sigma-Aldrich, Karlsruhe, Germany) with a relative density of 0.752 g/cm³ and the secondary phase was a 50 vol% solution of D(+)-sucrose (Carl Roth, Karlsruhe, Germany) in distilled water prepared at room temperature.

The cumulative particle size distributions of the model soils are shown in Figure 3.1. Data shown in blue in the diagram was used for calibration of the sensor. The soil types were a soil at a measuring station of Landesforsten Rheinland-Pfalz - forestry administration in Hermeskeil (Rhineland Palatinate High Forest, Germany), consisting of 22.8 % clay, 41.6 % silt and 35.6 % sand, soil at State Horticultural College and Research Institute (LVG; Heidelberg, Germany) with a $x_{50,3}$ of approx. 45 µm, soil at a measuring station of Landesforsten Rheinland-Pfalz - forestry administration in Merzalben (Rhineland Palatinate High Forest, Germany), consisting of 11.3 % clay, 19.0 % silt and 69.7 % sand, soil at Hegehof (Hegehof GmbH, Ladenburg, Germany) with a $x_{50,3}$ of approx. 190 µm, a model soil so called lawn base layer with lavasand (corthum Nordschwarzwald GmbH, Marxzell, Germany) with a $x_{50,3}$ of approx. 700 µm and coconut substrate at Erlenhof (Erdbeerland Funck GbR, Eisenberg, Germany) with a $x_{50,3}$ of approx. 1700 µm.

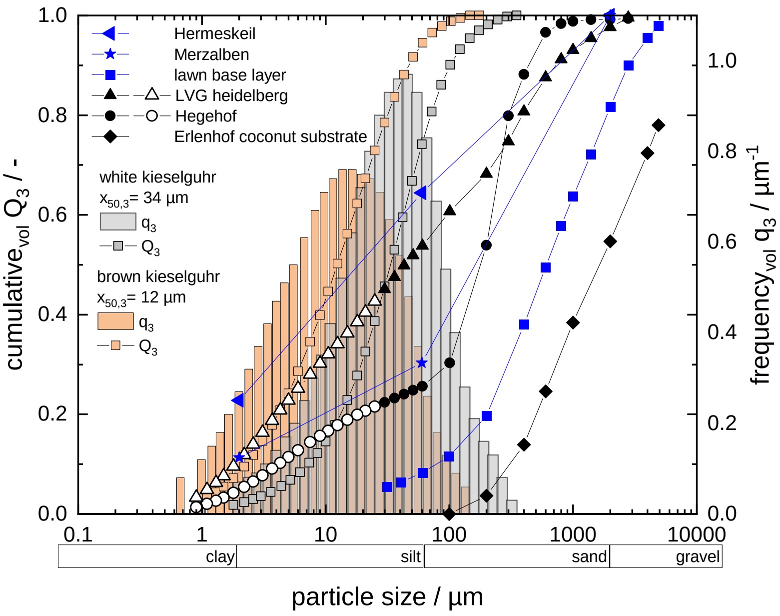

Figure 3.1 Particle size analysis of the used raw kieselguhr powders and soils. Cumulative distribution $Q_3$ and frequency particle size distribution $q_3$ were determined through sieve analysis (open symbols) and through Fraunhofer diffraction (filled symbols).

## 3.4.2 Ceramic disc fabrication

Suspensions were prepared by mixing the ceramic particles into the bulk phase in a planetary mixer (Speedmixer, Hauschild GmbH & Co KG, Hamm, Germany). Sample volumes of 70 ml were mixed for 5 min at 2200 rpm in 150 ml cups. Subsequently, the secondary fluid was added to the suspension and then mixed for 5 min at 2200 rpm and 1 min at 700 rpm. The solids content of the kieselguhr suspension was set to $\phi_{solid} = 15$ vol%. The amount of secondary phase was varied between $\phi_{sec} = 0 - 7$ vol%. The prepared pastes were placed by hand into a cylindrical sample mold (diameter = 55 mm and height = 8 mm). The sample's top was smoothed using a doctor blade. The mold was placed on an absorbent pad and directly demolded after filling was completed. Mechanical debinding of the bulk phase was carried out by capillary extraction for 3 days at room temperature, followed by thermal debinding at 200 °C (30 min), 500 °C (1 h), and 800 °C (1 min) to ensure a complete and gentle debinding of the bulk and secondary phase (LVT 05/11, Nabertherm GmbH). The heating rate to reach the different levels of constant temperature was 3 °C/min. Brown kieselguhr samples were heated to 1050 °C and white kieselguhr samples to 1160 °C, both with a heating rate of 5 °C/min and both subsequently sintered at their temperature for 2 h (LHT 04/17, Nabertherm GmbH). After sintering the ceramic plates height was adjusted to 5 mm, respectively, and a diameter of 45 mm by hand with SiC paper. In the center, a hole with a diameter of 3 mm was drilled to fix the ceramic discs on the circuit board.

### 3.4.3 Sensor layout

For measuring the water content in the porous ceramic discs two different methods have been developed. Both methods determine the capacitance between electrodes which is affected by the dielectric properties of the porous discs, i.e. their water content. In the first setup, comb-like electrodes are designed with proper geometric dimensions to confine the electrical field within the disc. The electrodes are embedded in a multilayer printed circuit board. An optional metal mesh encasing the disc provides an additional screen for the electrical field. The capacitance of the electrodes and the enclosed ceramic disc results in a resonance frequency of the electric circuit in the upper MHz range. A microcontroller read out via an RS-485 interface is used to determine the resonance frequency varying with the water content of the ceramic discs.

The second setup uses a transmission line within a time-domain transmission (TDT) circuit. The propagation velocity of electrical pulses along this line depends on the capacitance between the electrodes. [88] The geometric circuit dimensions are also designed to confine the electrical field mainly to the ceramic disc. The transmission line is embedded in a multilayer printed circuit board and forms a ring oscillator with the accompanying electronic circuit. The oscillating frequency is a few hundred MHz which is advantageous compared to the first design since variations of electrical conductivity of the water in the disc, e.g. due to varying salinity, has less effect on the measured signal. The oscillating frequency is measured by a microcontroller and usually provided as so-called “counts” which are the raw data for calibration experiments. The counts are inversely proportional to the oscillation frequency. The stability of the ring oscillator is about one count. Together with a dynamic range of over 1000 counts its resolution is 10 bit.

In Figure 3.2 both electrode structures are shown - on the left-hand side the comb-like electrodes and on the right the TDT circuit.

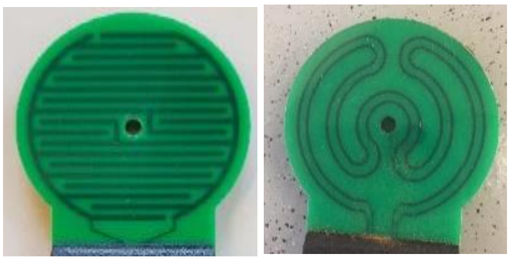

Figure 3.2 The electrode of the comb-like electrode (left) and the TDT (right).

## 3.4.4 Ceramic and sensor characterization

The open porosity of the ceramic discs was determined using Archimedes' principle according to DIN EN 993-1 (calculation of Archimedes density) and DIN EN 993-18 (technical implementation). Compressive mechanical strength was measured following DIN51104. Based on image processing using line intercept count method of crosscut images obtained from scanning electron microscopy in backscattering mode (SEM-BSE) pore size distributions were calculated as described in [17, 22].

The maximum and minimum count value of each sensor was determined from measurements with just the circuit board in air and in water.

To correlate the measured count values to the volumetric water content in the ceramic, the ceramics were first infiltrated with water for 1 min under atmospheric pressure and room temperature, then set for drying at ambient conditions until a selected count value was reached. For this condition, the water content of the ceramics was determined by drying the ceramics at 105 °C for 3 using a Halogen Moisture Analyzer HX204 (Mettler-Toledo GmbH, Gießen, Germany).

To analyze the temperature sensitivity of the sensors at different moisture levels, the sensors were infiltrated with water at the conditions already mentioned and also dried to a selected count value. The sensors were then completely sealed with a plastic cover and exposed to temperatures ranging from 5 °C to 50 °C in a refrigerator and drying oven.

For air drying experiments the porous ceramics were infiltrated with water and then set to dry under the conditions already mentioned.

For soil drying experiments lawn base layer with lava sand and coconut substrate were used as model soils, 16 vol% of distilled water was added during continued mixing using a dissolver stirrer. Sensors were placed in the soil, and drying took place at room temperature (approx. 20 °C), atmospheric pressure and a relative humidity of 36 ± 3 %.

Commercially available soil sensors used in this work were: the SMT100 (TRUEBNER GmbH, Neustadt, Germany) measuring the soil water content using a transmission line within a time domain transmission (TDT) circuit; the TEROS 21 Gen.1 formerly MPS-6 (METER Group, Inc., Munich, Germany formerly Decagon Devices, Inc., USA) a matric potential sensor using an impedance of 70 MHz signal in equivalent porous medium [64]; and the T8 tensiometer (METER Group, Inc., Munich, Germany formerly UMS GmbH, Munich, Germany) a matric potential sensor measuring the tension of water directly at a pressure transducer [64].

## 3.5 Experimental results

### 3.5.1 Ceramic and sensor properties

We characterized our white and brown ceramics regarding their open porosity $\varepsilon_{open}$, mechanical compressive strength $\sigma_c$ and pore size distribution to determine the highest possible porosity with acceptable strength for our ceramics.

The brown kieselguhr system shows a compressive strength of 27 ± 2 MPa at an open porosity of 52 ± 0.2 % when prepared without secondary fluid and a compressive strength of 12 ± 3 MPa at an open porosity of 59 ± 0.1 % with $\phi_{sec}$ = 7 vol%. The white kieselguhr system shows a compressive strength of 11 ± 1 MPa at an open porosity of 65 ± 0.2 % without added secondary fluid and a compressive strength of 6 ± 1 MPa at an open porosity of 69 ± 0.1 % with $\phi_{sec}$ = 4 vol%. At a given porosity the compressive strength of both kieselguhr systems is similar to that of aluminum oxide, one of the most widely used ceramic material [23]. Compressive strength of > 5 MPa was proven to be high enough to withstand all relevant stresses which were applied to the ceramic discs and the sensor during the laboratory and field tests. Therefore, the brown kieselguhr ceramic with a porosity of 59 % and the white kieselguhr ceramic with a porosity of 69 % were used for setting up the sensors.

The dimensions, characteristic pore size distribution data, mechanical strength and porosity of the discs made from brown and white kieselguhr used in our sensor setup are summarized in Table 2.

Corresponding SEM images, particle size distribution data and photographs of the sensors are shown in Figure 3.3.

Table 3.2 Data of ceramic characterization of brown and white kieselguhr ceramics.

| ceramic type | diameter / mm | height / mm | $x_{10,3}$ / µm | $x_{50,3}$ / µm | $x_{90,3}$ / µm | $\varepsilon_{open}$ / % | $\sigma_c$ / MPa |
|---|---|---|---|---|---|---|---|
| brown ceramic | 43.0 ± 0.2 | 5.0± 0.2 | 16 | 41 | 72 | 59 ± 3 | 12 ± 3 |
| white ceramic | 43.0 ± 0.2 | 5.0± 0.2 | 44 | 101 | 159 | 69 ± 3 | 6 ± 1 |

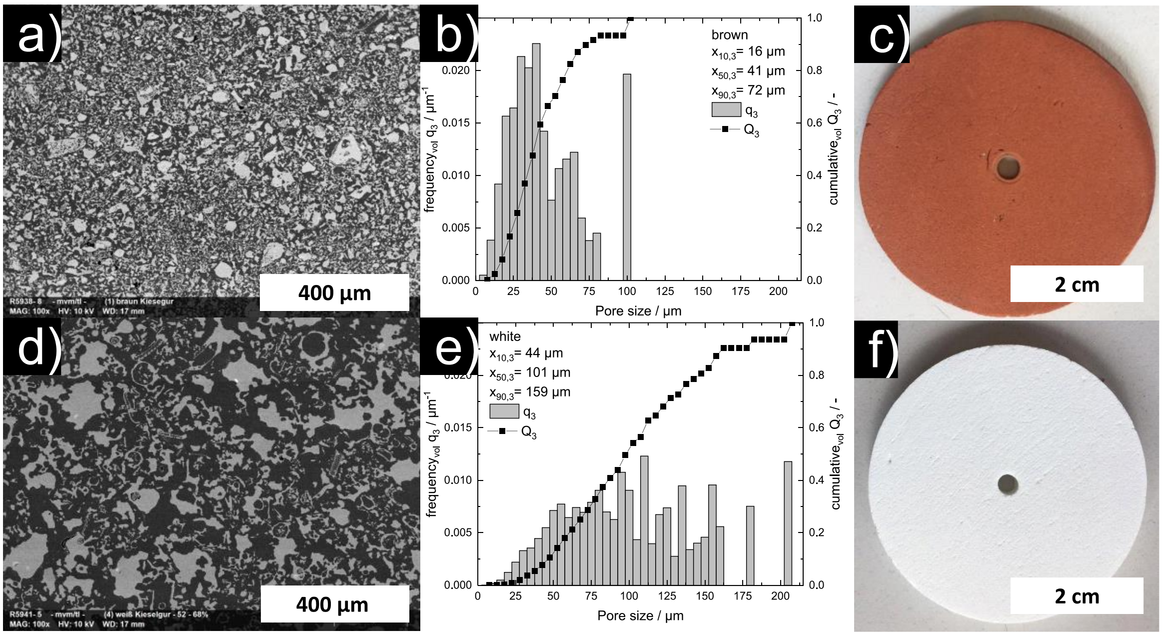

Figure 3.3 Comparison of the the brown (top) and white ceramics (bottom): SEM images of polished surfaces of sintered parts (cavities in black and ceramic material in white) [a), d)], pore size distribution $q_3$ ($x_{pore}$) and $Q_3$ ($x_{pore}$) [b), e)], top view of the ceramics [c), f)].

In order to establish the correlation between volumetric water content in the ceramic and a count value measured with the sensor, both white and brown kieselguhr ceramics with different water contents were analyzed. Explicit care was taken to ensure that there was no water between the plate and the ceramic, since this could induce systematic measurement errors. As the ceramics are completely infiltrated with water, values of 3400 ± 5 counts are obtained for the sensor. For completely dried ceramics, values of 4450 ± 5 counts are obtained. There is no significant difference whether the measurements are performed using brown and white ceramic discs. Thus, neither the material type nor the pore size distribution has a significant influence on the count values. The linear correlation between counts and volumetric water content in the ceramic is shown in Figure 3.4 (left).

For the experiments on the temperature dependence of the sensors between 5 °C and 50 °C, it was crucial that the sensors were completely sealed and no water could evaporate, which would distort the measurements. Sensitivity measurements were performed with both brown and white kieselguhr ceramics at different water contents. Regardless of the water content in the ceramic, there is a variation of up to 100 counts between the measured value at 5 °C and that at 50 °C (see Figure 3.4 (right)). Since the influence of the temperature is independent of the water content, this could be compensated by an additional control in the sensor. There is no significant difference in the use between brown and white ceramics.

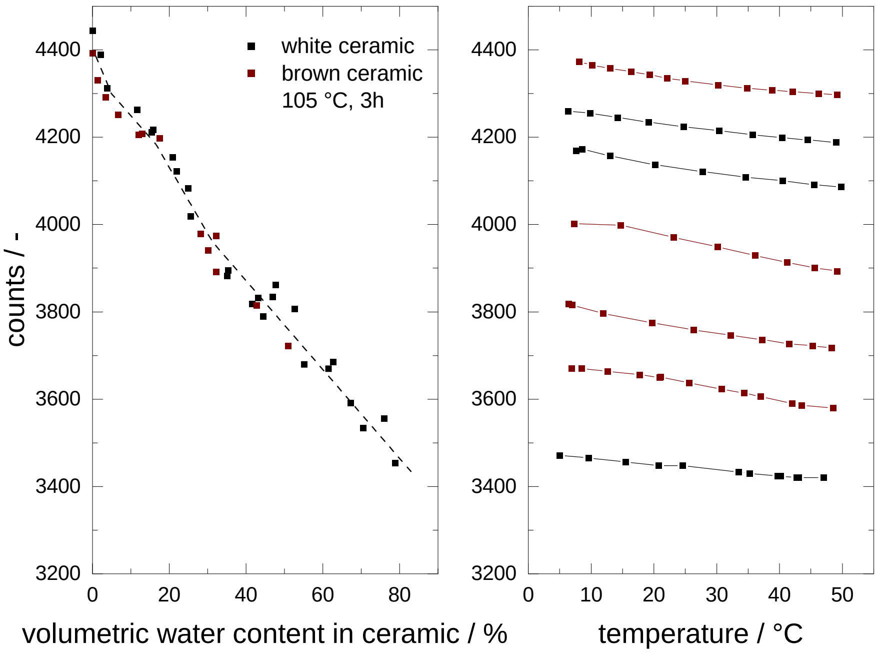

Figure 3.4 Correlation between measured counts and volumetric water content in white and brown ceramics (left) and sensors sensitivity with constant vol. water content: counts are plotted versus temperature (right).

The results of the air-drying experiment are shown in Figure 3.5. Fully infiltrated and submerged in water the sensors showed count values of approx. 3200 ± 5 counts for both ceramic types. The drying curves of the sensors with both ceramics do not show significant differences, although the ceramics show significant differences in the pore size distribution (see Figure 3.3). Obviously, the difference in pore size distribution of the two ceramics is not significant for drying kinetics under atmospheric pressure. In air at dry state the sensors mounted with white ceramics showed count values of approx. 4450 ± 5 counts and for sensors mounted with brown ceramics approx. 4400 ± 5 counts.

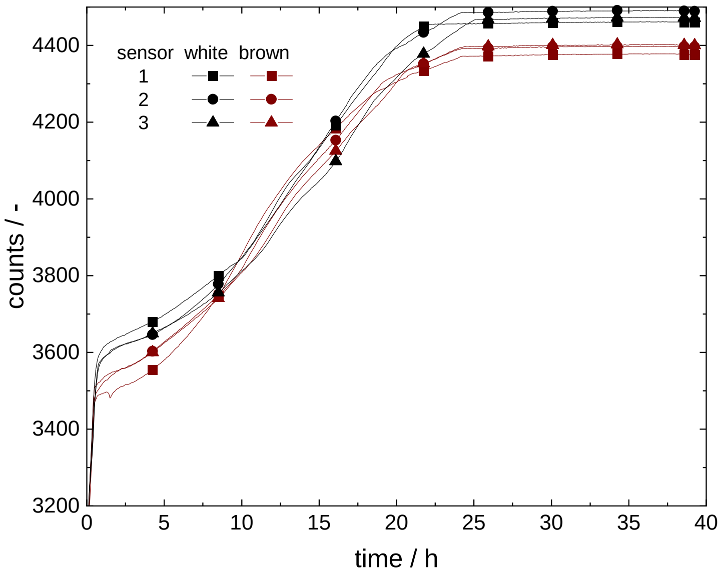

Figure 3.5 Drying experiment in air at 25 °C: counts are plotted versus time in hours, ceramic drying curves of six different TDT circuit sensors: three sensors with brown and three sensors with white ceramic discs.

### 3.5.2 Soil moisture measurement experiments

To test the electronic layout of the sensor and the different functionality of the two ceramics in soil and to test the sensor, soil moisture measurement experiments were conducted in soils with different particle size distributions.

The aim of these experiments was to find out the potential of the sensor for optimized irrigation, collect sufficient data to correlate measured counts with soil water potential and to compare the functionality of our sensor with commercially available sensors.

For the experiments, sensors mounted with brown and white ceramic discs were installed in two different soils for ***laboratory experiments*** and in field experiments at ***Hegehof***, ***Erlenhof***, at the Teaching and Research Institute for Horticulture in Heidelberg, Germany (***LVG)*** and at a measuring station at ***Hermeskeil*** and at ***Merzalben*** in the Rhineland Palatinate High Forest in cooperation with the Landesforsten Rheinland-Pfalz – forestry administration. A dielectric sensor for volumetric water content (SMT100), tensiometers (T8 and ES-3V 500) and a soil water potential sensor (TEROS 21) were used in this measurement campaign for comparison.

**Laboratory experiments**

For the soil drying experiments, 16 vol% water was mixed into the respective model soils. Six TDT circuit board sensors with ceramic discs of brown (three) and white kieselguhr (three), two sensors without ceramic for control and one commercial sensor ES-3V 500 tensiometer for comparison were placed in the soil.

In Figure 3.6 the corresponding drying curves for the experiment in the model soil lawn base layer are shown with counts plotted vs. time for our sensors and tensiometer data in mV vs. time. Based on manufacturer information [89] tensiometer data x were converted from mV into soil water potential values y in hPa as shown in Table 3.3 according to $y = 0.25x - 125$.

At the beginning all sensors are essentially dry and the initial count values were around 4400 counts for the brown and 4500 counts for the white ceramic discs, respectively. Then the sensors were placed in the wet soil, soak up with water and reach count values of 3250 for the brown and 3350 counts for the white ceramic discs, respectively, within minutes. Then, a hydraulic equilibrium with the surrounding soil was established within about 50 h as indicated by a constant level of counts. For the sensors mounted with brown ceramic discs at about 3400 counts and for the ones equipped with white ceramic discs at about 3500 counts. Subsequently, all sensors with white ceramic discs almost ran dry within approx. 150 h showing a value of about 4200 counts, but still kept steadily, but slowly drying to about 4400 counts within 300 h. The sensors mounted with brown ceramic discs were mostly dried after approx. 200 h and kept steadily drying to about 4200 counts within 300 h, too. The sensors with the white ceramics exhibited a count increase to the dry level much faster than those with the brown discs and we attribute this to the different pore size distribution with smaller pores and hence stronger capillary forces in the brown ceramics.

Within each set of ceramic types, however, no significant difference was observed regarding absolute count values and characteristic drying kinetics. The sensors without ceramic discs exhibited a monotonic increase in count values without equilibrium plateau value or a sharp increase corresponding to drying out. Instead, they monitored the monotonic loss of water in the soil. However, the absolute values of counts differed significantly between both sensors, which could be due to moisture content inhomogeneities in the soil.

The tensiometer established a hydraulic equilibrium with the surrounding soil just as both ceramics did. Subsequently, the SWP steadily increased until the tensiometer ran dry after approx. 125 h reaching approx. 1790 mV (322 hPa), 50 h later the tensiometer was refilled, but ran dry again within approx. 25 h, ending at the upper measuring limit of 3300 mV (700 hPa). According to the data sheet, the tensiometer has a certified upper measuring limit of 2500 mV (500 hPa).

Table 3.3 Conversion of tensiometer data from mV to soil water potential in hPa.

| **tensiometer/mV** | 500 | 1000 | 1500 | 2000 | 2500 | 3000 | 3500 |
|---|---|---|---|---|---|---|---|
| **SWP/hPa** | 0 | 125 | 250 | 375 | 500 | 625 | 750 |

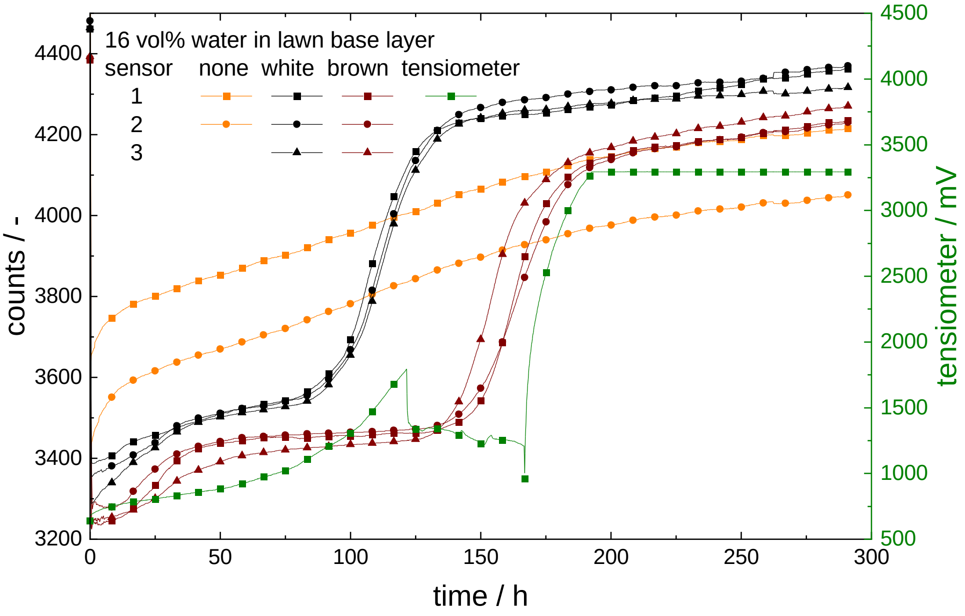

Figure 3.6 Drying experiment in model soil lawn base layer: counts are plotted versus time in hours, ceramic soil drying curves of eight different TDT circuit sensors: three sensors with brown and three sensors with white ceramic discs, two without ceramic disc, and one commercial tensiometer (ES-3V 500).

In Figure 3.7 the corresponding drying curves for the experiment in the model soil coconut substrate shown with counts plotted vs. time for our sensors and tensiometer data in mV vs. time. Here, the tensiometer data x were converted from mV into soil water potential values y in hPa just as in Figure 3.6 according to Table 3.3 based on manufacturer information [89].

The drying experiment in coconut substrate was very similar to the experiment in lawn base layer shown in Figure 3.6. At the beginning of the experiment, all sensors are essentially dry. After the sensors are placed in the moist soil, they become saturated with water and establish a hydraulic equilibrium with their surrounding soil, indicated by a constant level of counts. Here, count values of

3400 for the sensor with brown ceramic discs and 3500 for the sensor with white ceramic discs are reached. Subsequently, all sensors with white ceramic discs almost ran dry within approx. 300 h showing a value of about 4300 counts, but still kept steadily, but slowly drying to about 4400 counts within 800 h. The sensors mounted with brown ceramic discs were mostly dried after approx. 800 h. Jus

Just like in the drying test in the lawn base layer, the sensors with the white ceramics exhibited a count increase to the dry level much faster than those with the brown due to bigger pores and hence weaker capillary forces in the white ceramics.

Also in this experiment, the tensiometer establishes a hydraulic equilibrium with the surrounding soil just as both ceramics did. Subsequently, the SWP steadily increased until the tensiometer ran dry after approx. 175 h, also reaching approx. 1790 mV (322 hPa), after which it ceased to provide useful data.

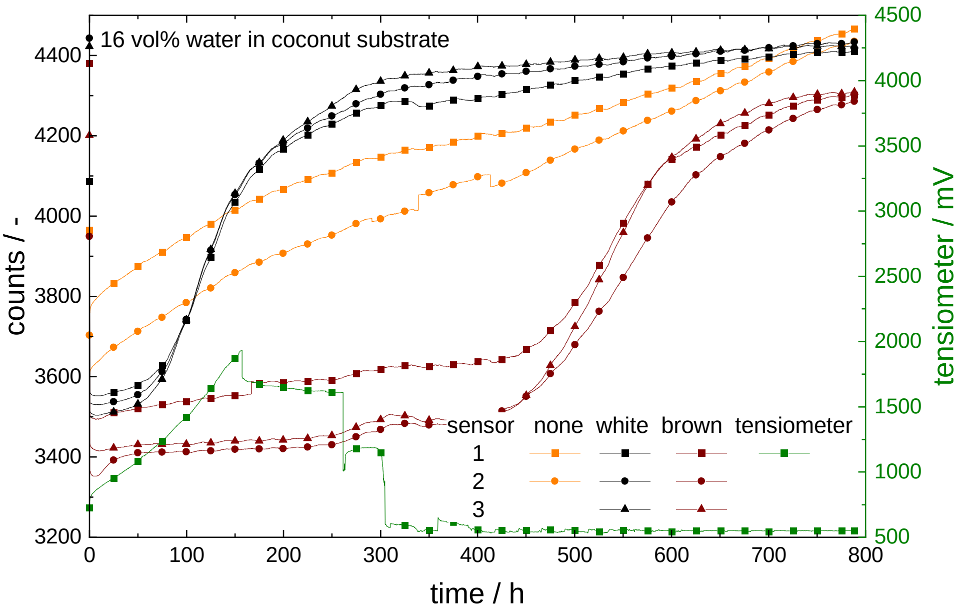

Figure 3.7 Drying experiment in model soil coconut substrate: counts are plotted versus time in hours, ceramic soil drying curves of eight different TDT circuit sensors: three sensors with brown and three sensors with white ceramic discs, two without ceramic disc, and one commercial tensiometer (ES-3V 500).

**Field experiments**

***Hegehof***

The sensors were installed in an asparagus bed in a depth of approx. 15 cm under plastic foil. Irrigation took place only through natural precipitation. The measuring period examined was between April 21, 2020 and June 06, 2020. In Figure 3.8 the variation of temperature during this is shown. The temperature in the soil ranged between a minimum of 10 °C and a maximum of 30 °C and reproduces the usual temperature fluctuations between day and night. All sensors exhibited the same temperatures during this trial. Furthermore, Figure 4 shows the corresponding soil moisture measurement values for the sensors with brown and white ceramic discs as well as for the SMT100.

The curves can be divided into three sections: the first section lasts up to about 250 h, the second to about 475 h and the last period extends to the end of the measuring period at 800 h. In the first range, the sensors with brown and white ceramic discs form a hydraulic equilibrium at approx. 3900 counts (white) and at approx. 3500 counts (brown). In the second regime precipitation took place on the fields. The sudden drop in temperature also indicates an atmospheric low-pressure period. The counts of the sensor with the white ceramic discs therefore dropped to 3750 counts and those with brown ceramic discs to approx. 3700 counts. The sensors reacted here with a strong delay, since the precipitation is only slowly absorbed into the asparagus soil wall due to the protective plastic film covering it. In the third period, the process of natural precipitation was repeated. Here, the count values for the sensor with white ceramic discs reached a minimum of 3600 and those for the sensor with brown ceramic discs a minimum of 3450. Both precipitation events were also recorded by the SMT100: volumetric water content increased from the first to the second regime from 11.5 vol% to 12.2 vol% and finally to 13.5 vol% in period three.

Although the SMT100 gives a relatively accurate indication of the increasing moisture in the soil, it is not possible to determine how much soil water is available for the plants.

The difference in the measurement values of the sensors with brown and white ceramic discs can be attributed to the different pore size distributions. The pore size distribution of the brown ceramic is much narrower than that of the white ceramic and has predominantly small pores. As a result, the brown ceramics exhibit a higher capillary effect and, in this case, extract more water from the surrounding soil than the white ceramics.

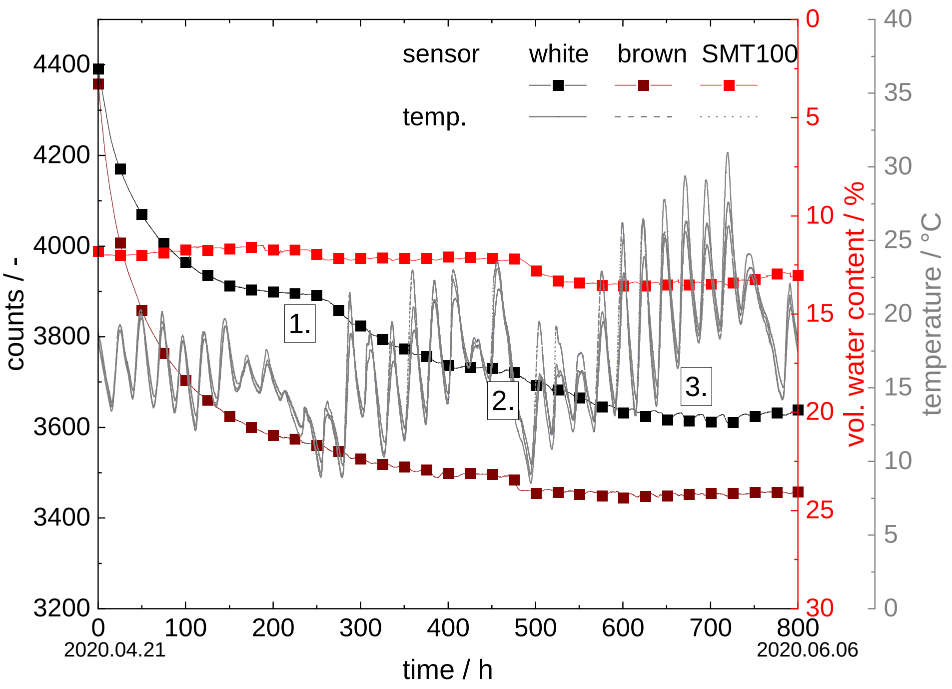

Figure 3.8 Soil moisture measurement experiment at Hegehof in asparagus field: counts are plotted versus time in hours for our new sensors, vol. water content vs. time for the SMT100

***Erlenhof***

For the experiments at the Erlenhof, a total of four sensors were installed in two 50 L pots between 27.04.2020 and 04.08.2020. The pots were filled with coconut substrate and planted with blueberries. The blueberries were regularly irrigated by an automatic irrigation system.

In Figure 5 the corresponding temperature is plotted vs time for all sensors in both blueberry pots. Further, in Figure 5 the corresponding soil moisture measurement curves are shown with counts plotted vs. time for the sensors with white ceramic discs and vol. water content vs. time for the SMT100.

The temperature in the substrate of both pots started at approx. 20°C on April 27 and fluctuated between a minimum of approx. 10 °C and a maximum of approx. 28 °C in the following weeks. The blueberry pots were located outside under a tunnel tent. The usual temperature fluctuations between day and night are reflected equally by all sensors. The sensors exhibit no significant difference among each other.

In the first blueberry pot, the SMT100 measured a water content of approx. 13.5 vol% for the first 1200 h. Subsequently, the water content dropped reaching a minimum of 6.5 vol% after 1650 h and then increased again to approx. 13.5 vol% in the final measurement period. Over the entire measuring range, the data fluctuated in a range of ± 6 vol%. This could be due to the sensor being installed very close to the irrigation unit. This means that each irrigation cycle is registered directly by the sensor, without the water being able to distribute itself evenly in the substrate beforehand. The sensor mounted with white ceramic discs established a hydraulic equilibrium with the surrounding soil within 24 h at approx. 3400 ± 50 counts. After 1200 h the counts values started to rise reaching a maximum of approx. 4050 ± 50 counts at 1650 h, then dropped to 3800 ± 50 counts for 100 h, and increased again to approx. 4050 ± 50 counts. Finally, the signal steadily dropped back to 3400 ± 50 counts. Like the SMT100, this sensor was installed close to the irrigation valve. This could allow the water to be absorbed by the sensor's ceramics during irrigation cycles without being evenly distributed in the substrate.

The data collected in the second blueberry pot were similar to those from the first pot. The SMT100 data, however, exhibit only weak fluctuations in a range of ± 0.5 vol%. This is due to the greater distance between the sensors and the irrigation valve. The measuring curve obtained using the sensor with white ceramic discs ran almost parallel to that of the SMT100 underlining the functionality of the new sensor.

Finally, this experiment shows that both the SMT100 and our sensor with white ceramic discs captured the water content in the coconut substrate, a soil which is a very coarse with a $x_{50,3}$ of approx. 1700 µm, satisfactorily. On the other hand, it also shows that the appropriate placement of the sensor in the substrate has a significant influence on the measurement results obtained.

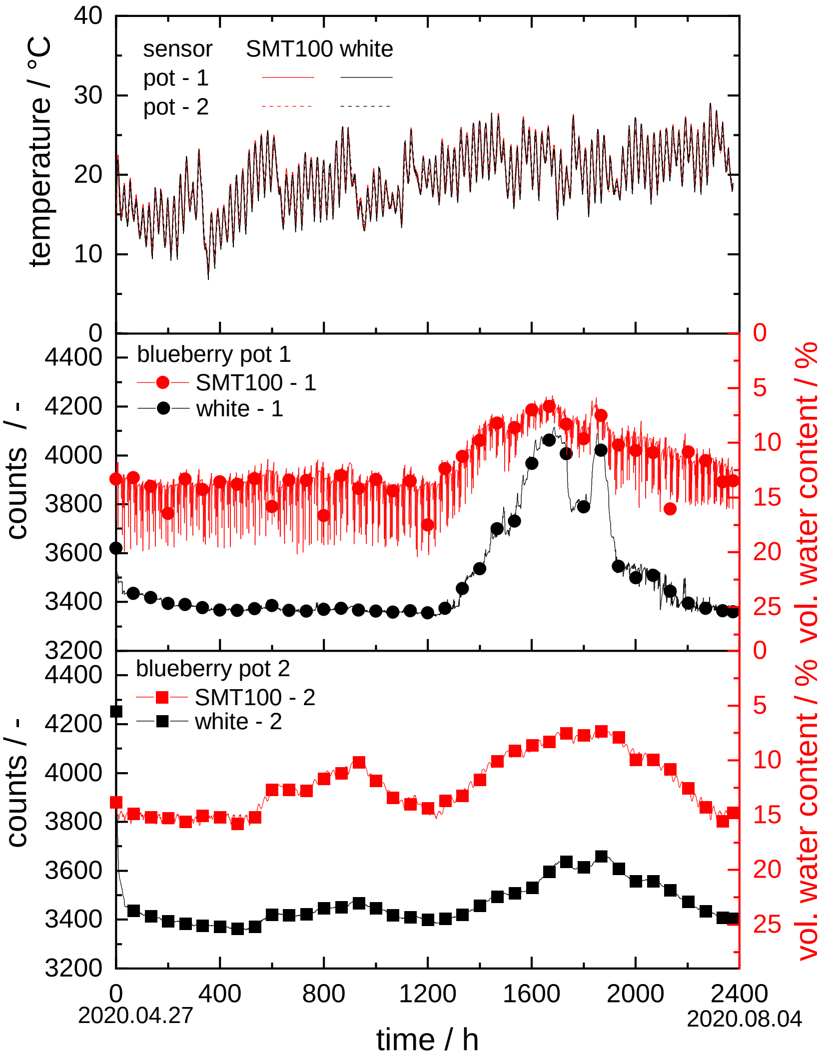

Figure 3.9 Soil moisture measurement experiment at Erlenhof in two blueberry pots: the upper graph shows temperature vs. time at all sensor positions, in the middle and lower graph counts are plotted vs. time in hours for our new sensors, vol. water content vs. time in hours for our new sensors, vol. water content vs. time for the SMT100.

***LVG***

For the experiments at the LVG, a total of seven sensors were installed in the tomato research field (see Figure 6) and eight sensors in the spinach research field (see Figure 7). In the tomato field, measurements were taken between 29.06.2020 and 06.08.2020 and in the spinach field between 07.10.2020 and 30.12.2020. In both fields, three and four sensors, respectively, were installed at two different locations approximately 1 m apart at a depth of 30 cm. Both fields were regularly irrigated by an automatic irrigation system with time schedule. In both Figure 3.10 and Figure 3.11 the temperature is plotted vs time for the sensors grouped at spot 1. Furthermore, the corresponding soil moisture data obtained from the sensors with white and brown ceramic discs, the SMT100 and the TEROS 21 are shown.

- Tomato research field:

The temperature in the soil started at approx. 20 °C on June 29 and fluctuated in the range of ± 1 °C in the following weeks. The small temperature variations between day and night are reflected equally by all sensors, the temperature signals detected by the different sensors exhibited no significant difference among each other.

At spot 2, initially a relatively dry area, the first irrigation took place after approx. 50 h, which was registered similarly by all three sensors, but for the ceramic disc sensor the respective count drop came with some delay. The soil water potential detected by the TEROS 21 then increased from -300 kPa to -10 kPa within 100 hours, the count value obtained by the sensor with white ceramic discs dropped from 4325 counts to 3315 counts in the same time interval and the water content measured with the SMT100 rose from 14.5 vol% to 25.6 vol%. The TEROS 21 then remained at -10 kPa without significant fluctuations until hour 700, then decreased to -90 kPa and finally rose again to -10 kPa, corresponding to lower measuring limit of the teros21. In contrast, the further drying (after 375, 600, and 800 h) and irrigation (after 400, 650, and 840 h) periods were similarly registered by the SMT100 as well as the ceramic disc sensors.

Since spots 1 and 2 were only about 1 m apart, the drying and watering processes detected by the three sensors were similar to each other. For the SMT100 at spot 1, the irrigation cycles were registered more strongly than at spot 2. For this sensor, for example, the measured water content in the soil even increased to approx. 35 vol% during the first irrigation period after 100 h. For the sensor with white ceramic discs and the TEROS 21 at spot 1, for example, the drying period after 600 hours showed up more pronounced, the sensor with white ceramic discs measured 4235 counts at this spot and the TEROS 21 detected a soil water potential of - 215 kPa. In contrast, at spot 2, the TEROS 21 registered no drying phase at all and the sensor with white ceramic discs detected a less pronounced drying phase. In addition, a sensor with brown ceramic discs was used at spot 1. Here, too, the transient counts data vary similarly as the data of the SMT100 showing the irrigation and drying cycles. However, since the pores of the brown ceramic discs were much smaller than those of the white ceramic discs, they retain the stored water more strongly, and as a result, the drying cycles in particular show up less pronounced. Here, the measured values increased to a maximum of 3600 counts after 800 h.

These measurements show in particular that the installation location of the sensor is significant for the obtained results. Even small differences in the distance to the irrigation unit among the individual sensors can cause significant differences in the obtained results. Basic irrigation or drying trends, however, were properly detected by all sensors at all installation locations in this trial.

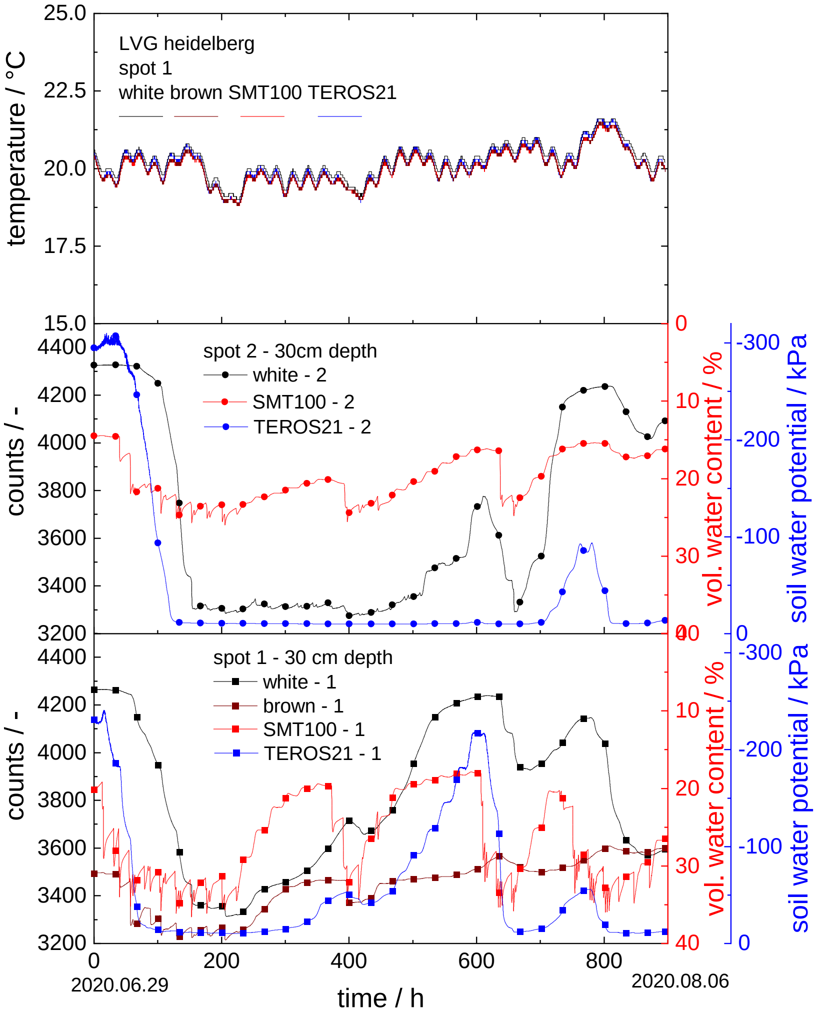

Figure 3.10 Soil moisture measurement experiment at LVG in tomato research field: the upper graph shows temperature vs. time at all sensor positions, in the middle and lower graph counts are plotted vs. time for the new sensors with white and brown ceramic discs, vol. water content vs. time for the SMT100 and soil water potential vs. time for TEROS 21

- Spinach research field:

The subsequent experiments in the spinach field at LVG were similar to those in the tomato field, but this time sensors with brown ceramics were installed at both spots and irrigation was carried out more regularly. Furthermore, the measuring domain of the TEROS 21 was reduced to a range of 0 to – 23 kPa.

The temperature in the soil started at approx. 18 °C on October 7 and steadily decreased to approx. 8 °C on December 30. Day and night fluctuations in the range of ± 1 °C during the whole measuring process were reflected equally by all sensors.

In the spinach field experiments, a total of five irrigation events were recorded by all sensors at both spots: after 35 h, 220 h, 730 h, 970 h, and 1500 h. If irrigation 3 at 730 h is neglected, all irrigations occurred after similar readings were obtained for the respective sensor at both spots with non-significant variations, data are summarized in Table 3.4.

Table 3.4 Data for the irrigation events at spot 2 and 1.

| spot | white / counts | TEROS 21 / kPa | SMT100 / % | brown / counts |
|---|---|---|---|---|
| 2 | 3484 ± 10 | 11.7 ± 0.5 | 16.5 ± 2.8 | 3292 ± 35 |
| 1 | 3406 ± 25 | 11.9 ± 0.6 | 16.5 ± 2.8 | 3567 ± 10 |

The differences between spot 2 and 1 were negligible for the sensor with white ceramic discs, the TEROS 21 and the SMT100. Only the sensors with brown ceramic discs showed a significant difference of 276 counts on average between the two spots. This could be due to the narrow pore size distribution and small average pore size in this ceramic. Due to the small pores, the ceramic might not be able to establish a hydraulic equilibrium with the different particle size ranges in the soil and thus may exhibit a significantly higher dependence on the correct positioning during installation.

The sensor with white ceramic discs provided promising results similar to the TEROS 21 in determining plant-available water in the soil. Compared to the SMT100, the transient data provided by these sensors show similar variations over time with high accuracy and little scatter.

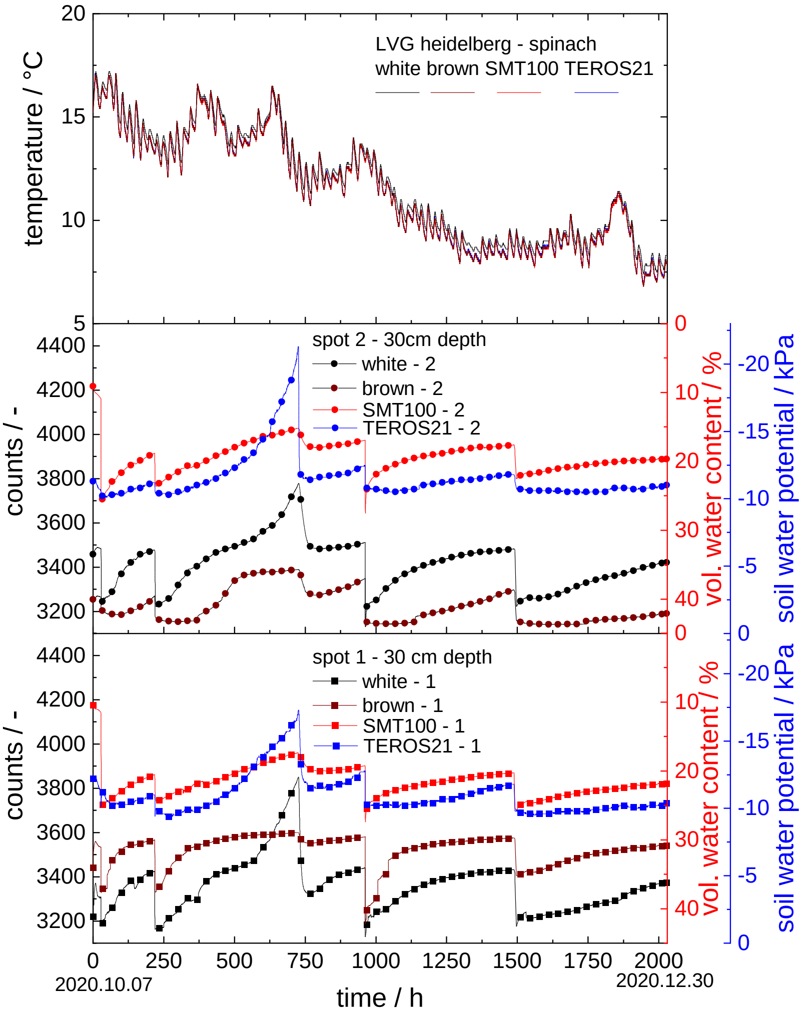

Figure 3.11 Soil moisture measurement experiment at LVG in spinach research field: the upper graph shows temperature vs. time at all sensor positions, in the middle and lower graph counts are plotted vs. time in hours for our new sensors, vol. water content vs. time for the SMT100 and soil water potential vs. time for TEROS 21.

***Forest field experiments***

For the forest field experiments, sensors mounted with brown and white ceramics and a dielectric sensor (SMT100) were installed at a measuring station at Hermeskeil in the Rhineland Palatinate High Forest and at Merzalben in Palatinate Forest in cooperation with the Landesforsten Rheinland-Pfalz-forestry administration. The results of the soil moisture measurements are shown in Figure 3.12 for Hermeskeil and Figure 3.13 for Merzalben. In both cases irrigation took place only through natural precipitation.

- Hermeskeil:

At the measuring station a tensiometer (T8) was already installed in a depth of 60 cm. The six additional sensors were mounted in a depth of 30 cm and 60 cm. The measuring period examined was between Mai 27, 2020 and August 12, 2020.

All three sensors used at a depth of 30 cm registered the precipitation events after 210, 550, 1200, 1650 h. According to the measurements, however, the forest soil dried out over the whole measuring period. The measured values of the sensor with white ceramic discs increased over the measuring period from 3860 to 4230 counts and those with the brown ceramic discs from 3530 to 4070 counts. At the same time the water content according to the SMT100 decreased from 19.5 to 14.8 vol%.

The data recorded with the sensors at a depth of 60 cm are similar to those at a depth of 30 cm. The difference, however, is that the precipitation events are not registered by the sensors at a depth of 60 cm. Only for the first event after 210 h the sensor with white ceramic discs as well as the T8 tensiometer show a slight drop in the measured values. Overall, the long term drying out of the soil became even clearer at a depth of 60 cm: here the count values detected by the sensor with white ceramic discs increased from 3820 to 4260 counts and those registered with the brown ceramic discs sensor increased from 3580 to 4210 counts. At the same time, the vol. water content according to the SMT100 drops from 23.8 to 18.4 vol%. TheT8 tensiometer registered an increase in soil water potential to the degree of drying out completely after 1000 h, reaching the maximum reading of 825 hPa. This is followed by the typical drying-out behavior of such kind of tensiometer itself, in which the measured values decrease constantly, but not related to a change in soil humidity.

This experiment revealed a great disadvantage of the commercial tensiometer, which was no longer functional above a certain soil water potential and required increased maintenance. Especially in remote areas, our sensor offers a valuable alternative, since it does not require any service and can still measure far beyond the soil water potential limit specified by the classical tensiometers (here 825 hPa).

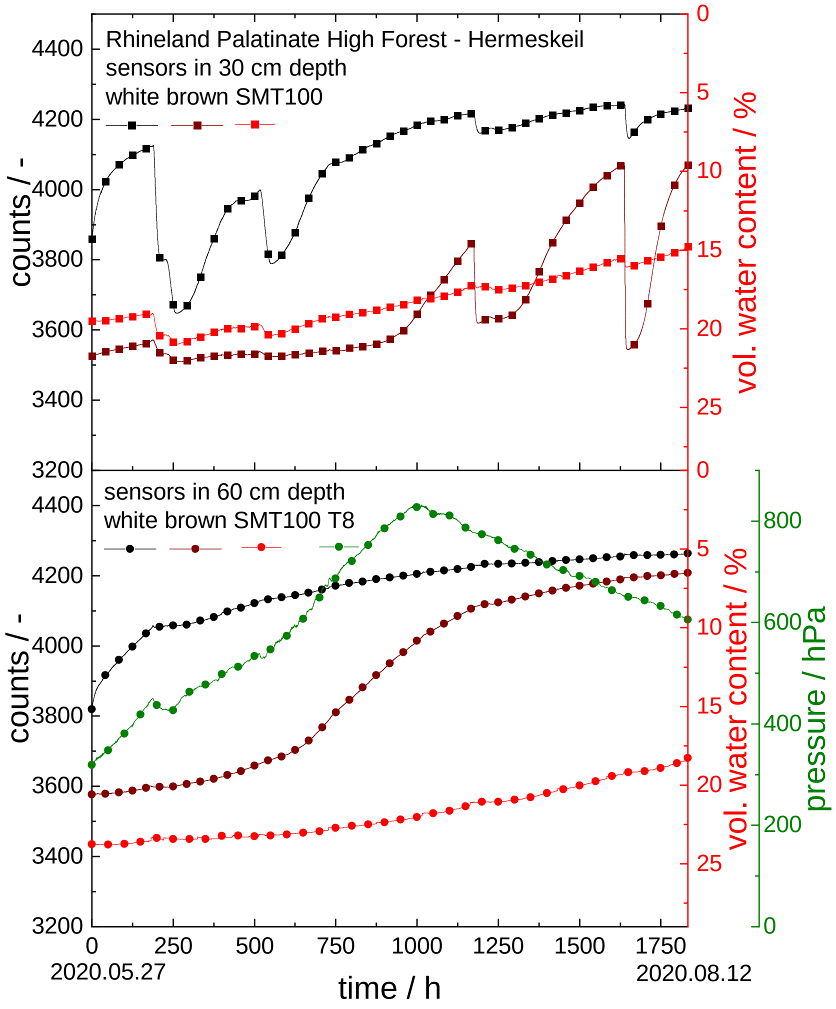

Figure 3.12 Drying experiment in forest soil (Rhineland Palatinate High Forest – Hermeskeil): counts are plotted vs. time in hours for the sensors with the ceramic discs, vol. water content vs. time for the SMT100 and soil water potential vs. time for the T8 tensiometer. Time = 0 h corresponds to the date May 27, 2020, and time = 1833 h to August 12, 2020

- Merzalben:

At the measuring station a tensiometer (T8) was already installed in a depth of 30 cm. The three additional sensors were mounted in a depth of 30 cm. The measuring period examined was between April 1, 2020 and July 21, 2020. The temperature in the soil started at approx. 5 °C in April and steadily rose to approx. 15 °C in July. The sensors exhibit no significant difference among each other.

The sensor mounted with brown ceramic discs quickly established a hydraulic equilibrium at approx. 3500 counts and did not show a significant change for 2250 h. From this point on, the ceramic dried out monotonically within the next 50 hours to approx. 4200 counts. Subsequently, the value dropped to 3500 counts indicating strong rain. Then the ceramic discs dried out again within the next 250 h to subsequently register strong rain again after 2800 h indicated by another drop to approx. 3500 counts, and finally another drying process started.

The sensor mounted with white ceramic discs also established a hydraulic equilibrium at approx. 3500 counts at the beginning, but quickly started drying until after 750 h a count drop to 3370 counts was registered. The rain was also detected by the SMT100 with an increase in water content from 13 vol% to 15 vol%, and for the T8 a decrease in soil water potential from 146 hPa to 77 hPa was found within that period of time. During the next 2000 h, the sensor equipped with the white discs repeatedly captured switches between drying and irrigation by rain, which was detected consistently also by the SMT and the T8 sensors. After approx. 2700 h, however, the tensiometer ran dry, as indicated by the monotonic drop in the measured values over the remaining period in time. At this point, the great advantage of the new sensor concept is evident, as it continued to register rainfall and dry periods, which is characterized by falling and rising count values registered at times > 2500 h. The SMT100 also continues to work reliably even in very dry soil. However, it only indicates the volumetric water content, which, as already explained above, requires additional information about the soil properties for reasonable interpretation

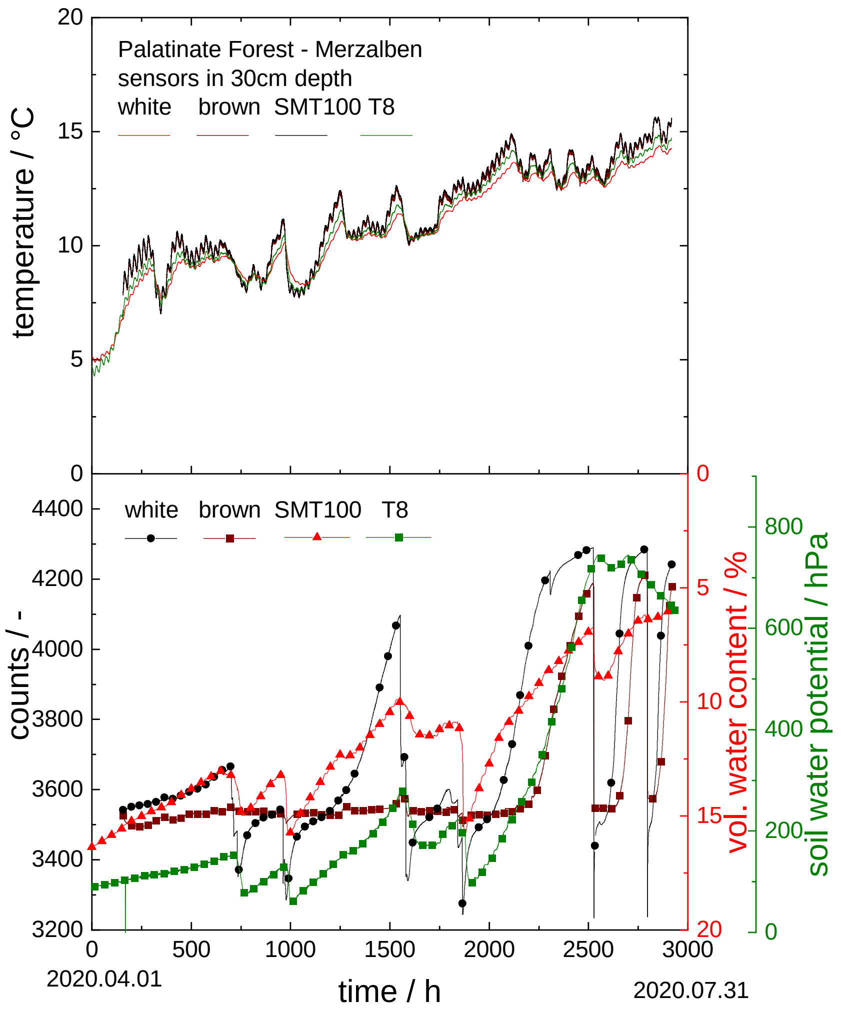

Figure 3.13 Drying experiment in forest soil (Palatinate Forest – Merzalben): temperature is plotted vs. in hours for all sensors (top), counts are plotted vs. time in hours for the sensors with ceramic discs, vol. water content vs. time for the SMT100 and soil water potential vs. time for the T8 tensiometer. Time = 0 h corresponds to the date April 01, 2020, and time = 3000 h to July 31, 2020.

## 3.6 Discussion

To make irrigation efficient and resource-saving, the water available to plants in the soil should be determined reliably and accurately. With this goal in mind, we developed a novel sensor.

In order to retrieve the soil available water for plants, this sensor detects the resonance frequency of an electrical circuit, which includes two ceramic discs as dielectric layers in a capacitor layout. The resonance frequency depends on the water content in these discs, i.e. the amount of water absorbed from the surrounding soil, and is subsequently converted into so-called counts as an output signal of the sensor system. However, the counts are only raw data which should be converted into the soil water potential, since this parameter is generally used to characterize the water available for plants.

To achieve this, the soil water potential obtained from a commercial T8 tensiometer is plotted as a function of the count values recorded with the novel sensor during forest soil experiments in Hermeskeil and Merzalben, as well as in laboratory experiments in lawn base layer and coconut substrate. Corresponding data are shown in Figure 3.14. During the experiments in Hermeskeil, the upper measurement limit of 850 hPa of the T8 tensiometer was exceeded, but the ceramic disc sensor still recorded data during further drying of the soil. A linear correlation was assumed to extrapolate water potential data corresponding to these count values (shown as open symbols in Figure 3.14). An empirical function was fitted to the whole set of data points (see equation (10)):

$$\mathrm{SWP} = \mathrm{f(counts)} = \frac{1}{a+b\cdot counts^{c}} \tag{10}$$

$$a = 0.1$$

$$b = -0.01$$

$$c = 0.274$$

Based on this function, the count values from the new ceramic sensor can be converted into soil water potential data with a reasonable accuracy ± 100 hPa, no additional knowledge about soil composition is required.

In the wet regime around 3400 counts the measured data show irregular scatter. This could be due to the delayed data logging of the T8 tensiometer, which occurs during abrupt changes in soil moisture such as heavy rain. Our sensor does not exhibit this delay. As a result, measured count values are assigned to soil water potential values that are too high. In addition, hysteresis in the irrigation and drying process occurs with tensiometers such as T8 [90]. For this reason, fluctuations of ± 50 hPa in soil water potential up to 3800 counts are present in the correlation.

Particularly in the dry regime > 4000 counts, the soil water potential values obtained at a given count value in the Merzalben soil are systematically higher than those recorded in the Hermeskeil soil. this could be due to the different particle size distributions in these soils. Since the soil in Hermeskeil includes a larger fraction of small particles, the water is bound more strongly there, especially in the dry regime. The sensor including the white ceramic discs with a wide pore size distribution was explicitly designed to form a hydraulic equilibrium with all soils. However, there are apparently still systematic differences in the range of ± 100 hPa in the measured data when the particle size distribution in the soil differs greatly.

With our novel sensor and the empirical model proposed in equation (10), it is now possible to accurately characterize the soil water potential from very wet to very dry conditions up to 1200 hPa independent of the soil type with an accuracy ± 100 hPa. The reproducibility of SWP determination in a single given soil even is ± 15 hPa.

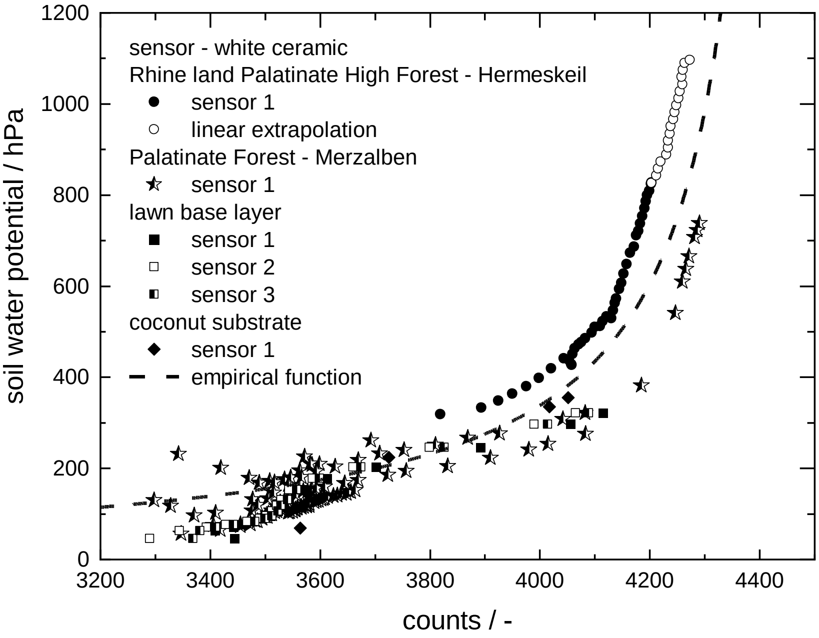

Figure 3.14 Correlation of soil water potential data (T8) and count values from the sensor with white ceramic discs recorded during drying experiments in model soil lawn base layer and coconut substrate as well as forest soil (Palatinate Forest – Merzalben and Rhine land Palatinate High Forest – Hermeskeil).

## 3.7 Conclusion

We presented a novel sensor for soil moisture characterization. This device includes a printed circuit board with tailored electronic layout and two porous ceramic discs mounted on it. Dielectric measurements are used to determine the amount of water absorbed by the discs which is considered to be related to the soil water potential. The porous ceramic discs were fabricated using an innovative processing route employing so-called capillary suspensions as pre-cursor [17, 22] allowing for tailoring a wide pore size distribution, very high porosity, and sufficient mechanical strength. The novel sensor is a highly sensitive and robust device with a wide measurement range, as confirmed here in a large number of field trials in direct comparison with competing products.

The new sensor provides accurate and reliable results, in particular, the experiments with controlled irrigation have shown that the sensor provides data with high accuracy and low scatter. It is thus a valuable tool, suited for optimizing irrigation in agriculture.

Based on a comparative study including three very different soil types a universal, empirical relationship between the output signal of the new sensor and the soil water potential as obtained using a T8 tensiometer was established which allows for a determination of the soil water potential without knowledge about the soil composition.

## 3.8 Acknowledgments

D. Menne would like to thank corthum Nordschwarzwald GmbH for the donation of the model soil, Mike Brando from the Landesforsten Rheinland-Pfalz for installing the sensors in the Palatinate Forest and Rhine land Palatinate High Forest and supporting me with valuable information, Thorsten Bornwaßer from the State Horticultural College and Research Institute for the help with the field experiments and supporting me with valuable information, Maximilian Hege at Hegehof and Alexander Seiler at Erlenhof for the help with the field experiments. Thanks also to Thomas Lebe (KIT) for the work at the SEM microscope, Astrid Huber and Klaus Hirsch (both KIT) for the analysis of the particle size distributions, as well as Sebastian Brecht, Yuan Yu and Nikolas Müller (all KIT) for contributing to the ceramic characterization and drying experiments.

D. Menne acknowledges support by the KIT-Publication Fund of the Karlsruhe Institute of Technology and financial support by the Federal Ministry of Education and Research (BMBF – KMU - innovativ), grant no. 02WQ1465B.

# 4 Giant Functional Properties in Electroceramics

Full titel: Giant Functional Properties in Electroceramics

Authors: David Menne, Lucas Lemos da Silva, Magnus Rotan, Julia Glaum, Manuel Hinterstein, Norbert Willenbacher

Status: published [40]

Bibliographic data: *ACS Appl. Mater. Interfaces*, 2022, *14* (2), 3027–3037; doi: 10.1021/acsami.1c19297.

**Abstract**

Dedicated hierarchical structuring of functional ceramics can be used to shift the limits of functionality. This work presents the manufacturing of highly open porous, hierarchically structured barium titanate ceramics with 3-3 connectivity via direct ink writing of capillary suspension type inks. The pore size of the printed struts (~1 μm) is combined with a printed mesostructure (~100 μm). The self-organized particle network, driven by strong capillary forces in the ternary solid/fluid/fluid-ink, results in a high strut porosity and the distinct flow properties of the ink allow for printing high strut size to pore size ratios, resulting in total porosities > 60 %. These unique and highly porous additive manufactured log-pile structures with closed bottom and top layers enable tailored dielectric and electromechanical coupling, resulting in an energy harvesting figure of merit $FOM_{33}$ more than four times higher than any documented data for barium titanate. This clearly demonstrates, that combining additive manufacturing of capillary suspensions in combination with appropriate sintering allows for creation of complex architected 3D-structures with unprecedented properties. This opens up opportunities in a broad variety of applications, including electromechanical energy harvesting, electrode materials for batteries or fuel cells, thermoelectrics, or bone tissue engineering with piezoelectrically stimulated cell growth.

## 4.1 Table of Content

We fabricated highly porous, hierarchically structured barium titanate ceramics with 3-3 connectivity via direct ink writing using capillary suspension type inks. The unique pore structure yields remanent piezoelectric strain coefficient values similar as for dense barium titanate but at ≈ 60% porosity and an energy harvesting figure of merit four times higher than any documented data for this particular material.

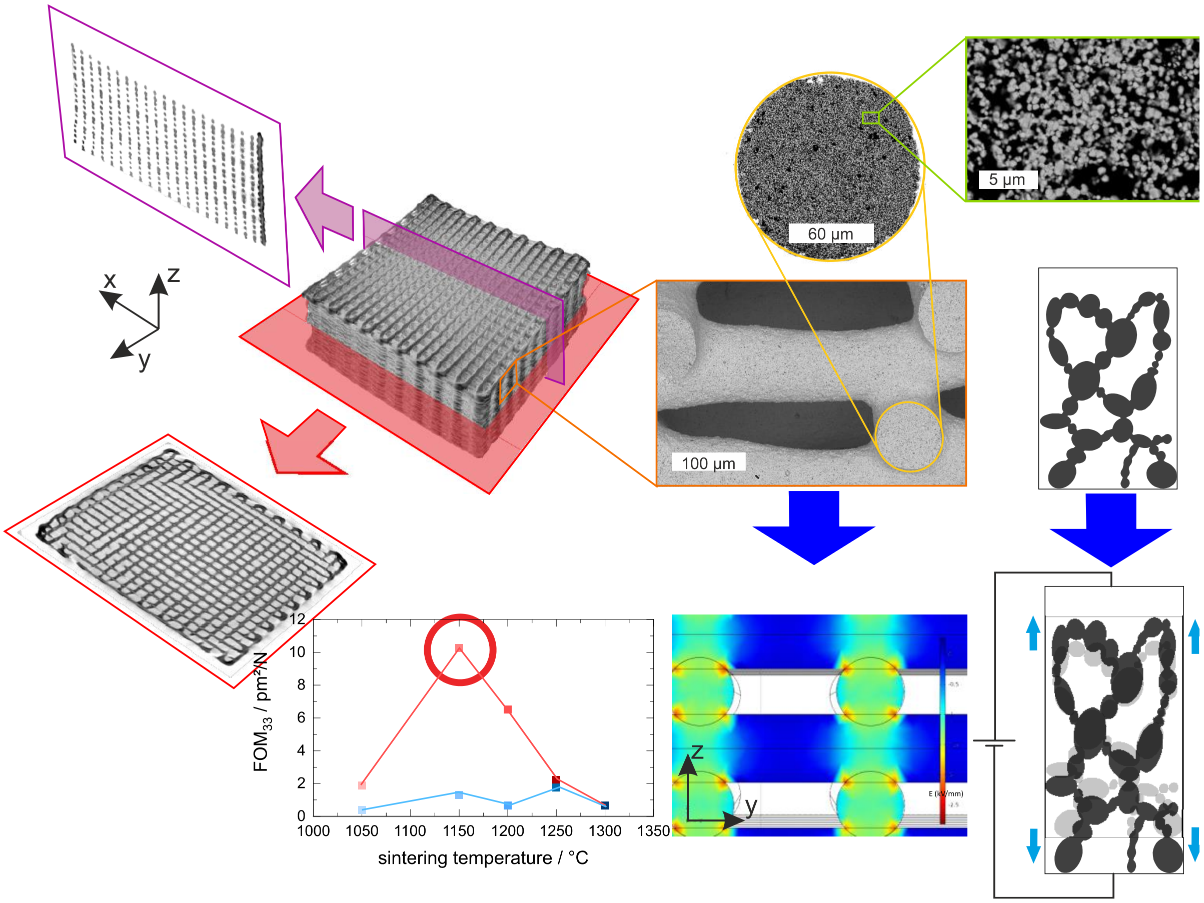

Figure 4.1 Giant Functional Properties in Electroceramics - Table of Content

## 4.2 Introduction

Complex porous ceramic structures are relevant for a wide range of applications, as they can be used for filtration of liquids, chemical reactive media or high temperature gases, as catalyst carriers, heat exchangers, lightweight construction materials and bio-mimetic materials, e.g. as bone substitutes. [1, 6–10] The microstructure, i.e. the open and closed porosity, the pore size, the pore orientation, the grain size, the degree of sintering and the hierarchical structure has to be carefully adapted to the demands of the respective application. [1, 2] To date, however, most applications focus on the mechanical and thermal properties of these mesostructures. Here we demonstrate that combining the mechanical properties with functional ceramics opens up new pathways for designing a new class of functional materials. These architected, hierarchically organized structures can be used to enhance the functional properties of electroceramic materials beyond previous limits.

Porous ceramics are usually manufactured by sacrificial templating, direct foaming, replica technique or partial sintering. [1, 2, 91–93] A novel, innovative and inexpensive method for creating highly open porous ceramics has recently been developed by Dittmann *et al.*. [17] It is based on the capillary suspension (CapS) phenomenon introduced by Koos *et al.*. [18] A CapS is an ink consisting of particles, a bulk fluid, and a small fraction of an immiscible secondary fluid. The capillary forces acting in this ternary solid/fluid/fluid system induce the formation of a self-organized, sample-spanning particle network with high shear modulus and yield stress, suited as a precursor for the porous sintered body. Fabricated porous ceramics are composite materials (ceramic – air) and are generally used as structural materials. [7]

AM of ceramic materials has attracted huge interest, since it allows for rapid prototyping, but also versatile and cost efficient production of parts with complex shape since no expensive tools or additional moulds are needed. [5, 94–96] So far there is a strong focus on dense objects with complex, often cellular, shape. However, AM has also been combined with various above mentioned porous ceramic concepts to obtain hierarchically structured cellular materials with exceptional specific strength. [24, 96, 97]

Beyond that, such complex structures can be combined with functional ceramics to obtain new materials with unique properties based on synergies of composite structures and functionality. A high demand for such complex structures with different functionalities currently emerges in the field of energy conversion. Ion exchange in fuel cells can be dramatically increased with a large surface area of oxygen or proton conducting materials. [98, 99] Future solid state batteries will only be competitive if the volume of active material can be dramatically increased with short conductive paths. [100] A combination of AM and self-organized particle networks yields a hierarchically structured cellular material with high specific strength. [24, 53, 96] Such synergy effects may also be used to improve mechanical and thermal energy conversion. By tailoring the electrical and thermal conductivity the efficiency of thermoelectric materials can be dramatically improved. [101] Similar effects can be observed for mechanical energy harvesting when the dielectric and electromechanical coupling is carefully adjusted. [102] Looking at nature, bone is a similar functional material exhibiting distinct porosity. It is a composite material consisting of collagen and hydroxyapatite, both exhibiting piezoelectric characteristics. [103–106] This intrinsic piezoelectric behavior of bone is discussed as one of the mechanisms governing bone healing and re-structuring processes. For this reason, research focuses on new types of electrically active implants that stimulate cell growth in the bone through stress induced surface charges. [107–109] The use of such active implants could be applied, for example, in the treatment of osteoporosis, bone loss of astronauts in space [110] or the design of flexible piezoelectric nanogenerators for biomechanical energy harvesting [111–113].

To take the next step forward in developing hierarchically structured functional materials, additive manufacturing comes into play, as it enables the manufacturing of precise structures with complex geometries or assemblies with interconnected structures. Using AM, a broad range of degrees of connectivity such as 0-3, 1-3, 2-2, 3-3 are accessible. Here, the first number refers to the connectivity of the material and the second number refers to the connectivity of the porosity. [114]

Some studies indicate that for example freeze casting can be used to fabricate structures with 3-0, 3-3 and 2-2 connectivity and thus enhanced piezoelectric energy harvesting properties can be achieved. [102, 115–118] According to these studies, the relative permittivity $\varepsilon_r$ of a material can be lowered by increasing porosity and thus the figure of merit $FOM_{33}$, the key parameter for energy harvesting, can be increased (see equation (11)):

$$FOM_{ij}^{\sigma} = \frac{d_{ij}^{2}}{\varepsilon_{ii}^{\sigma}} \tag{11}$$

Here $d_{ij}$ is the piezoelectric strain coefficient and $\varepsilon_{ii}^{\sigma}$ the permittivity, both in tensorial notation. However, the degrees of freedom that structures with 3-0, 3-3 and 2-2 connectivity exhibit cannot be fabricated as easily using conventional methods such as extrusion, tape-casting, replication, dice-and-fill, gel-casting and freeze casting as they can with AM methods. [119, 120]

Moreover, recent studies have shown that especially AM can be used to optimize the microstructural properties of piezoelectric materials, such as barium titanate (BT), and as a consequence, optimize functional properties as well. [121] A broad overview of additive manufactured piezoelectric ceramics is given by Chen *et al.*. [13] According to this review, BT and BT-based ceramics have already been investigated using AM techniques such as stereolithography, [13, 122, 123] binder jetting, [124, 125] extrusion free forming, [126] fused deposition modeling, [127, 128] selective laser sintering, [129] electrical poling-assisted additive manufacturing [130] or, solvent evaporation-assisted 3D printing [131]. Only few studies deal with the extrusion or DIW of BT and only a small fraction of those investigates the production of 3D printed ceramic bodies. [13, 132–134]

So far, using CapS as a pre-cursor is one of the most versatile and efficient ways to simultaneously achieve high open porosity (40 – 80 %) and pore sizes in the range from 0.5 to 50 µm in ceramic materials, and their microstructure can be finely tuned based on the choice of particle size, particle loading as well as type and amount of secondary fluid. [17, 22] Due to their distinct flow behaviour including a high yield stress and pronounced shear thinning, CapS are ideally suited for DIW and accordingly a second length scale of porosity, i.e. an architected mesostructure can be introduced. Based on this concept, Maurath *et al.* [24] adapted the composition of $Al_2O_3$-based CapS and developed appropriate DIW protocols to obtain undeformed, crack-free cellular ceramic structures with overall open porosity close to 90 % and unusually high specific strength.

The aim of this study is to demonstrate how this innovative ink concept and AM can be used to fabricate hierarchically structured porous ceramics with outstanding functionality, potentially applicable for energy harvesting or as bone substitute materials, but also for thermoelectric materials or as electrode materials in fuel cells and solid-state batteries. The combination of AM and CapS is especially well suited to obtain controlled complex porous structures, as it is possible to 3D print 3-3 structures, with the printed struts also being 3-3 composites. We manufactured log-pile structures with and without printed bottom and top layers from BT-based CapS. Printing behaviour of the CapS-type pastes as well as the accessible printed and self-organized structures were carefully analyzed. AM samples were compared to conventionally sintered (CS) reference samples. We employed different heat treatments and analyzed the different degrees of sintering, with respect to their microstructure (porosity, grain- and pore size) as well as their piezoelectric response. We could demonstrate that, the piezoelectric properties of functional ceramics can be taken to a new level by combining AM techniques and CapS.

## 4.3 Materials and methods

### 4.3.1 Raw materials

Commercial grade BT, 99 % (metals basis) particles were purchased (Alfa Aesar, Karlsruhe, Germany). The average particle size according to Fraunhofer diffraction is $x_{50,3} = 1.05\ \mu m$ (see Figure 4.2 left for particle size volume frequency - and cumulative distribution). The used particles have a spherical shape and are therefore well suited for creating capillary suspensions [25] (see Figure 4.2 right SEM image of the used BT powder). The particles have a density of $\rho = 5.95\ g/cm^3$.

As bulk phase for 3D printing a mixture of 37.6 vol% low viscous paraffin oil ($\eta = 0.035$ Pa s, $\rho = 0{,}85\ g/cm^3$; Carl Roth GmbH & Co. KGaA), 47.4 vol% mineral spirits ($\rho = 0{,}752\ g/cm^3$; Sigma Aldrich), and 15 vol% stearin wax ($\rho = 0{,}92\ g/cm^3$; TrendLight Creative GmbH) were used. The wax was dissolved in the mixture of the two liquid phases by heating the solution up to 70 °C while constantly mixing with a magnetic stirrer for 15 min. Subsequently, the mixture was further homogenized in a non-contact planetary mixer (Speedmixer$^{TM}$ 150.1 FVZ, Hauschild GmbH & Co KG) for 5 min at 2400 rpm. The secondary phase was an aqueous solution of 50 vol% D( + )-sucrose (Carl Roth GmbH & Co. KGaA). The three-phase contact angle of the system $\theta_{SB} = 31.6 \pm 5.4°$ was determined as described in, [24] placing the system in the pendular state. [17, 18]

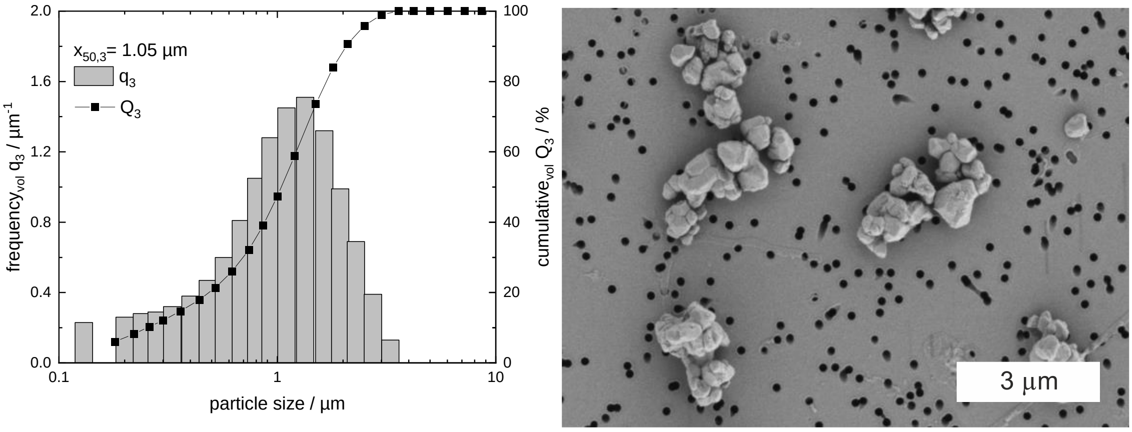

Figure 4.2 Left: Particle size analysis of the used BT powder. Particle size frequency distribution $q_3$ and sum distribution $Q_3$ were determined through Fraunhofer diffraction. Right: SEM image of the used BT powder.

The X-ray diffraction (XRD) pattern of the commercial-grade BT powder (99 %, metals basis) is displayed in Figure 4.3**.** The diffractogram does not show any secondary phases or significant impurities.

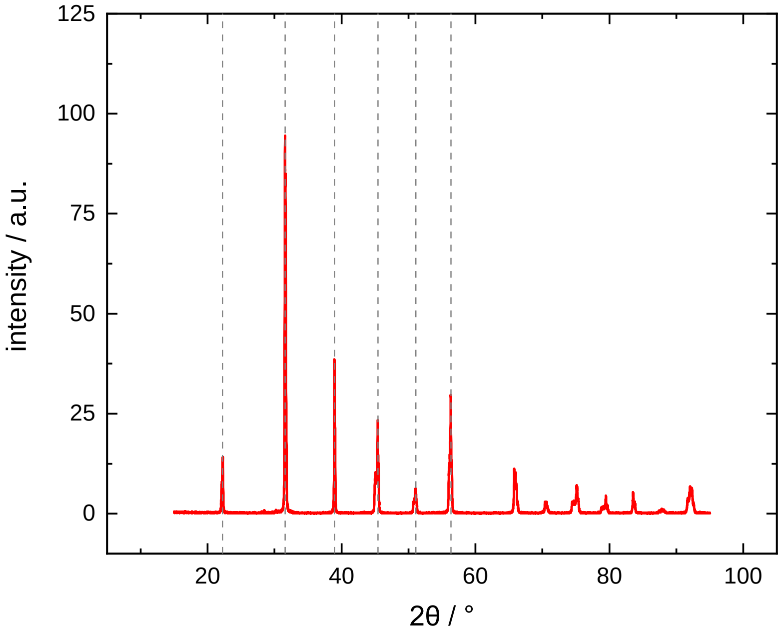

Figure 4.3 XRD pattern of commercial-grade BT, 99 % (metals basis) recorded using a D8-A25-Advance diffractometer (Bruker Corp.).

## 4.3.2 Sample preparation, printing, and sintering procedures

Suspensions were prepared by mixing BT particles (31 vol%) into the bulk phase in a non-contact planetary mixer (Speedmixer$^{TM}$ 150.1 FVZ, Hauschild GmbH & Co KG). We prepared a sample volume of 70 ml in 150 ml cups for 5min at 2400 rpm. Subsequently, the second fluid phase (2 vol%) was added and the suspension was mixed for 5 min at 2400 rpm. Followed by a subsequent de-agglomeration step in a three-roll mill EXAKT 80E (EXAKT Advanced Technologies GmbH) with decreasing gap width from 40 down to 10 µm and a roller speed of 160 rpm.

For the so-called conventionally prepared samples, the powder was dried, sieved (250 µm sized mesh), then pre-pressed into 10 mm diameter discs applying 20 MPa in a uniaxial press, followed by subsequent pressing in a cold-isostatic-press (CIP) at 200 MPa.

Log-Pile structures and log-pile structures with a bottom and top layer were 3D-printed using a commercial direct ink writing device (Developer`s Kit 3D Printer, Voxel8, Inc.). The structure consists of 21 parallel lines in one layer and a total of 40 layers. The capillary suspensions were extruded at room temperature with constant volumetric flow rates and constant print head speed (600 mm/min) through stainless steel tips with inner diameter of 150 µm (Nordson EFD) controlled by the applied pressure (480 kPa) directly onto porous alumina sintering plates. The distance between the layers of the log-pile structure was kept constant at $z = 0.12$ mm. Thereafter, the green body was mechanically debinded on porous alumina sintering plates at room temperature for 5 days. Organic binder components and secondary liquid in the green bodies were then burned out in a debinding furnace (LVT 05/11, Nabertherm GmbH) heating the samples to 200 °C (holding time $t_H = 30$ min), 500 °C ($t_H = 30$ min), and then 800 °C ($t_H = 1$ min) with a heating rate of 2 °C/min.

The samples were treated in a stepwise heating process (all in air and without flux): this means that the samples were heated in a first sintering step at a heating rate of 5 °C min$^{-1}$ to 800 °C ($t_H = 1$ min) and with a heating rate of 2 °C min$^{-1}$ to 1050 °C ($t_H = 2$ h). This was followed by cooling to 800 °C ($t_H = 1$ min) with a cooling rate of 2 °C min$^{-1}$ and cooling to room temperature in a sintering furnace (LHT 04/17, Nabertherm GmbH). After the temperature treatment, the samples were tested for their electromechanical and piezoelectric properties.

Subsequently, these samples were heat-treated in PT crucibles covered with an alumina lid leaving a 1-2 mm gap using 5 °C/min as heating rate up to 800 °C (1 min) and 2 °C/min up to 1150 °C ($t_H = 2$ h) and finally cooled down to 800 °C ($t_H = 1$ min) with a cooling rate of 2 °C/min and then to room temperature. Afterwards, theses samples were tested for their electromechanical and piezoelectric properties again.

Finally, the samples were temperature treated at the previously mentioned heating and cooling rates with the sintering temperatures of 1200, 1250 and 1300 °C ($t_H = 2$ h). Between each temperature treatment, the electromechanical and piezoelectric properties of the samples were determined.

### 4.3.3 Characterization

Rheological characterization of the printing inks was performed using a stress-controlled rheometer (Haake Mars II, Thermo Fisher Scientific Inc.) equipped with a plate-plate geometry (upper plate: titanium, lower plate: stainless steel) with a diameter of 35 mm. Both plates were rough (sandblasted surface) to prevent wall slip. The experiments were conducted at a gap height of 1 mm and a temperature of T =20 °C. The storage modulus G' and the apparent yield stress $\sigma_y$ were obtained from the stress amplitude sweep experiments performed at an angular frequency ω = 1 rad/s. G' was determined as the plateau value in the linear viscoelastic regime (LVE) and $\sigma_y$ was determined as the shear stress amplitude at the crossover, at which G' = G'', with the loss modulus G''. [135] The storage modulus G' determined as described above is also called shear modulus, since for the gel-like inks or pastes this quantity is essentially constant in a broad frequency range covering several orders of magnitude. [24]

The strut porosity $\varepsilon_s$ was determined using the Archimedes' principle according to DIN EN 933-1. The true porosity and density were calculated from sample dimensions and weight.

SEM images (S-4500; Hitachi High Technologies Europe GmbH and Zeiss Supra 55; Carls Zeiss AG) of sintered part cross-sections were used to analyze the microstructure. Pore size was calculated from the SEM using the line intercept method as described in. [22] Grain size measurements were performed following a line intercept method using the Lince software (Lince 2.4.2, TU Darmstadt, Germany).

X-ray computed tomography (XCT) measurements were obtained using an industrial scanner (XT H 225 ST industrial CT scan, Nikon Metrology Inc.).

For electric characterization, the AM structures, as well as the CS, were sputtered with silver paste on two opposite sites. Polarization, capacitance, relative permittivity, and piezoelectric coefficient ($d_{33}$) as a function of the electric field at room temperature were analyzed with a piezoelectric evaluation system (aixACCT, aixACCT Systems GmbH). Polarization and capacitance using a single loop, no prepolarization, and a hysteresis frequency of 1 Hz. The piezoelectric coefficient for the dense pellet (1.0 mm height) was measured using a small frequency and amplitude of 1 kHz and 30 V, respectively. For the 3D-structures (3.1 mm height) using a small frequency and amplitude of 1 kHz and 94 V, respectively.

## 4.3.4 Microstructural analysis

Figure 4.4 shows the densification rate versus temperature of the BT powder used from the optical dilatometry experiment. At 1050 °C, the powder used shows no densification. Sintering starts at 1150 °C, indicated by a weak increase in the slope of the densification rate. Thereafter, the densification rate increases to higher temperatures such as 1200 °C and reaches a maximum at 1250 °C. At a temperature of 1300 °C, the densification process no longer shows any change and the material is completely densified. To understand the effects of the degree of sintering on the electrical properties of a sample, samples without sintering effects (1050 °C), with just formed sinter necks (1150 °C), the highest compression rate (1250 °C) and the maximum compression (1300 °C) are investigated.

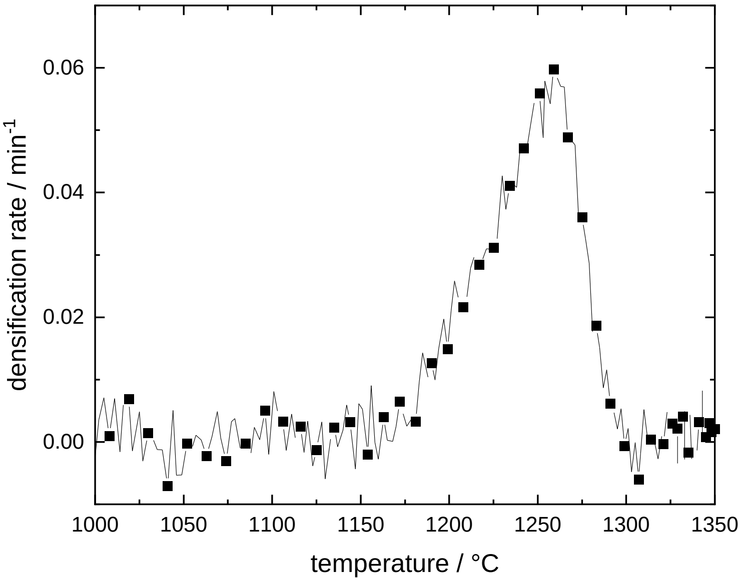

Figure 4.4 Densification rate of the used BT using a TOMMI PLUS optical dilatometer (Fraunhofer Institute for Silicate Research).

## 4.4 Results and discussion

We used the CapS concept to 3D print precise and fine log-pile structures with commercial grade BT. Figure 4.5 shows the typical microstructure of a sintered BT sample (10x10x5 mm) as obtained using computed tomography (CT). Viewing the CT scan in z-x axis shows the cross-section of the AM sample with 20 thin filigree struts stacked in z-direction, resulting in a total of 40 layers (Figure 4.5 b). The sample shows a slight curvature from the center to the sides and a slightly pyramidal shape, which is due to the shrinkage resulting from the sintering process, here performed at 1150 °C for 2 h. This is also the reason for not just seeing one but two layers when slicing the CT scan in the x-y axis (Figure 4.5 c). Shrinkage, however, is much less pronounced for CapS than for conventional suspensions, due to the strong capillary forces still present during de-binding, this also reduces crack formation significantly. [26, 27] Adjusting the composition of the BT-ink to the distinct wetting and surface properties of these particles, we were able to print homogeneous struts with a diameter of about 100 µm, while spanning pores of up to 400 µm (see Figure 4.5 d and e). Such high strut/pore width ratios of about 1:4 are possible since CapS-type pastes exhibit yield stress ($\sigma_y$) and shear moduli (G’) significantly higher than the corresponding two-phase suspensions, [27] here $\sigma_y = 192 \pm 7$ Pa and $G' = G'' = 3209 \pm 152$ Pa. Due to the properties of CapS, it was even possible to achieve strut/pore ratio of approx. 1:6 (70 µm strut and 440 µm pore diameter) previously not accessible (see Figure 4.10). The printed struts exhibit a porosity of $\alpha_s = 40.3 \pm 0.5$ % and the 3D printed log-pile structure had an overall open porosity of $\alpha = 58.4 \pm 0.2$ %. This is due to the sintered particle network formed by CapS, as shown in the SEM cross-sectional image in Figure 4.5 f and schematically illustrated in Figure 4.5 h and i.

Figure 4.5 g) shows a finite element method (FEM) simulation in which an electric field is applied to a log-pile specimen with dense struts. This simulation shows that the printed struts in the x-y plane are not affected by the electric field (dark blue area), however, the connected struts in z direction show a clear electromechanical coupling along the electric field direction. Therefore, this mechanical 3-3 composite has 1-3 electromechanical properties. According to Roscow *et al.*, [102] 3-1 and 2-2 connectivity types show higher values for $d_{33}$ coefficients than those with uniformly distributed porosity at similar porosity levels, indicating that the 3D printed structure could be further optimized. 1-3 interconnects would significantly reduce permittivity and thus increase the $FOM_{33}$ values, but provide very low mechanical stability. In contrast, our log-pile structures as 3-3 mechanical and 1-3 electromechanical composites offer both high $FOM_{33}$ values and high mechanical stability.

In addition to the sample geometry, the grain size and the sample porosity also have a major influence on the electromechanical and dielectric properties. [136, 137] One way to significantly influence both is the sintering protocol and here, we focus on the sintering degree of the AM sample made from our CapS ink in comparison to the CS obtained from the compacted powder.

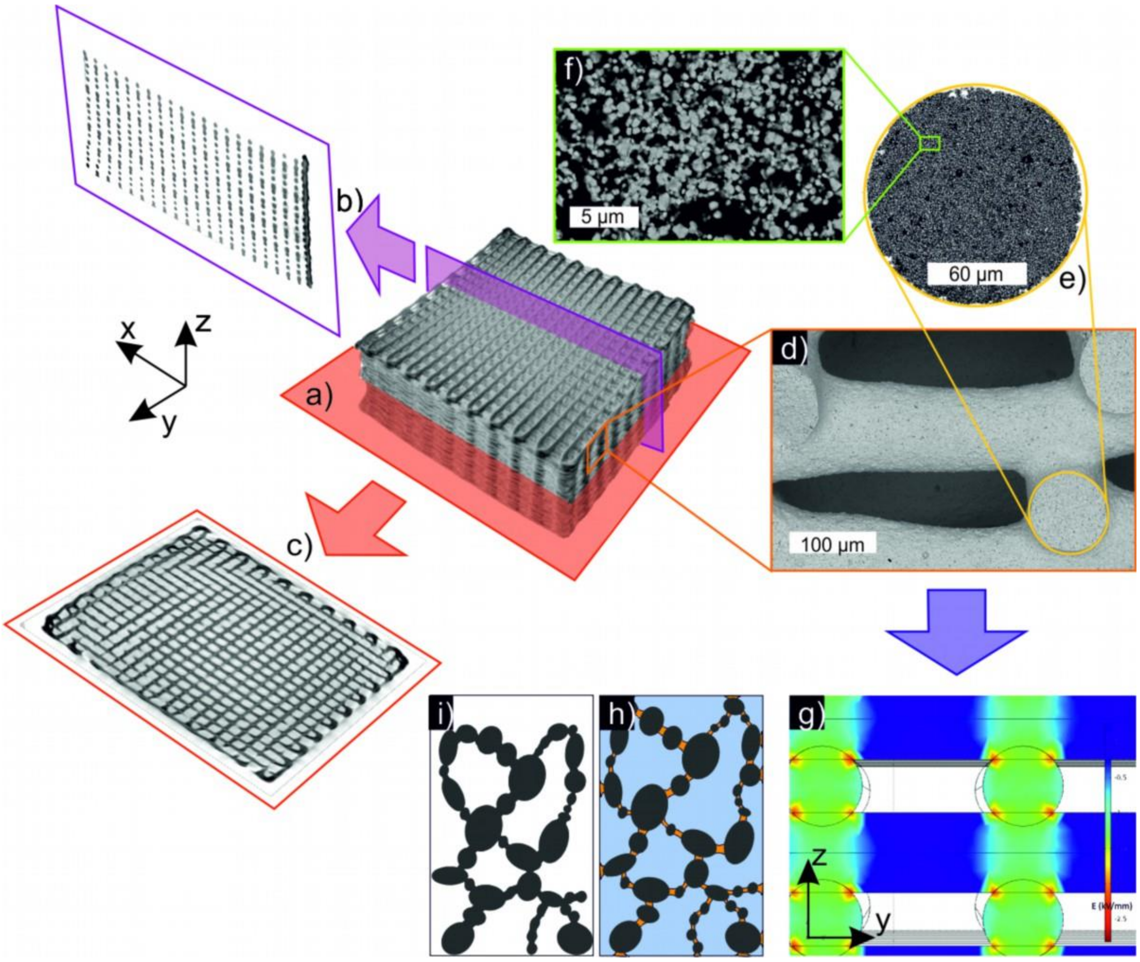

Figure 4.5 CT scan of 3D printed BT log-pile structure (10x10x5 mm): overall CT scan (a), crosscut through struts (b) and horizontal crosscut (c). SEM side view of a broken open log-pile structure (d), SEM crosscut image of magnified strut (e) and crosscut image with the unique microstructure of sintered capillary suspensions (f). The electric field intensity in a log-pile structure simulated with COMSOL Multiphysics®-Software (g). Schematic illustration of a capillary suspensions as paste (h) and sintered form (i). A paste with 31 vol% particle loading and a secondary fluid volume fraction of 2 % was used to print this object.

The upper row of Figure 4.6 shows SEM cross-sectional images of AM samples (Figure 4.6 a-d) and the lower row shows the micrographs of the CS samples (Figure 4.6 e-h) (see Figure 4.11 for enlarged images). Sintering temperatures range from 1050 °C to 1250 °C with dwell times of 2 h. The corresponding porosities are shown below each image. The strut porosity data and for the AM samples also the overall (3D printed scaffold) porosities are summarized in Table 4.1. The grain sizes of all samples correspond to the initial particle sizes of approximately $g_1$ = 1.0 µm.

At a sintering temperature of 1050 °C, both the AM sample (Figure 4.6 a) and the CS sample (Figure 4.6 e) show a low degree of sintering since the temperature is close to but still below the onset temperature of sintering activity. Although the CS sample was prepared with a cold isostatic press (CIP) and the AM using the CapS technique, the microstructures as observed in the SEM images appear similar. However, the samples show significant differences in porosity (Table 4.1), $\alpha$ =35.4 ± 1.5 % for the CS and $\alpha$ =50.6 ± 1.4 % for the AM sample. The high porosity of the AM sample is due to the particle network self-assembled in the CapS-type printing ink. At T = 1150 °C the AM sample exhibits a low degree of sintering, still maintaining the grain size (1.0 µm) but reducing the porosity to 40.3 ± 0.5 %. The sample-spanning particle network now is connected by necks throughout the sample. Necks also begin to form in the CS sample. As a result, the particles move closer together, the sample shrinks, and the porosity is reduced to 26.3 ± 0.9 %, while the grain size remains unchanged.

When the sintering temperature is further increased to 1200 °C, the necks continue to evolve for both the AM and CS samples. The grain sizes remain at 1.0 µm, but the porosity further decreases to 35.9 ± 0.9 % for the AM and 22.7 ± 1.4 % for the CS sample. When a sintering temperature of 1250 °C is applied, the driving force during sintering, i.e., the reduction of the surface energy, is greatest. At this state the densification is highest. The necks for the AM sample continue to form, causing the porosity to decrease to 32.5 ± 0.5 % with an unchanged grain size of 1.0 µm. For the CS sample, maximum densification occurs, resulting in a low porosity of 3 ± 0.5 % and no grain growth. Higher sintering temperatures, e.g., above 1320 °C, lead to abnormal grain growth due to a liquid phase in the BT phase diagram [136] and are not beneficial for the structural properties of the sample. The high structural stability and compressive strength of porous ceramics from capillary suspensions has been thoroughly discussed for bulk samples, [22] 3D printed cellular structures, [24] as well as for samples reinforced via deposition of nanoparticles at the neck between the sintered $Al_2O_3$ particles. [28] For the BT-based AM sample studied here (T = 1150 °C), we found 0.338 ± 0.112 for the relative compressive strength at a relative density of 0.427 ± 0.036, consistent with previous reports on CapS. [22, 24, 28]

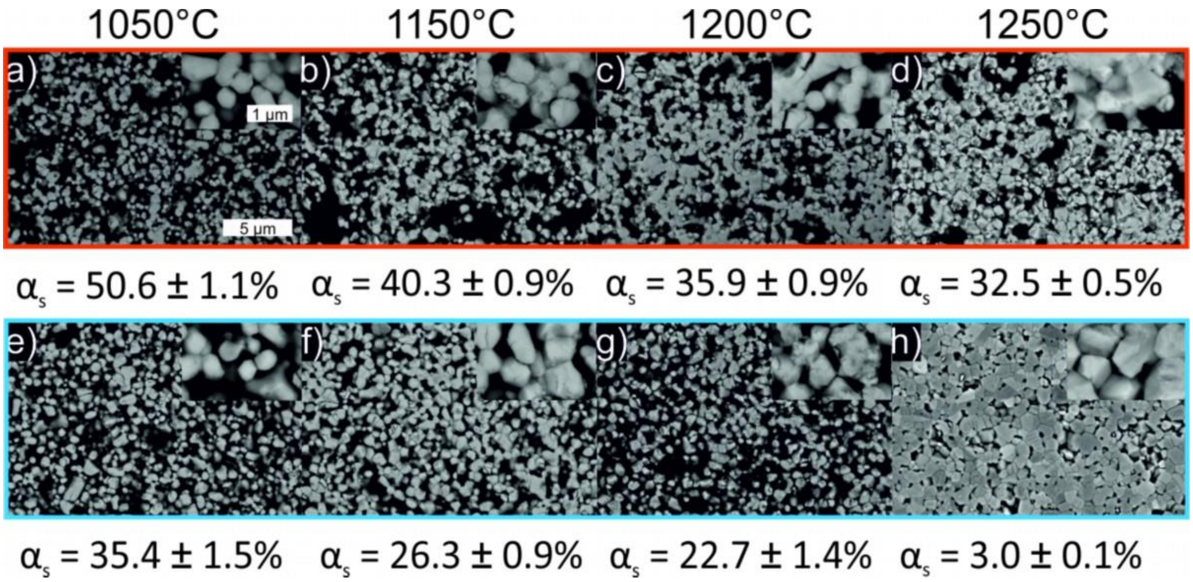

Figure 4.6 Crosscut SEM images showing the microstructure of AM samples sintered for 2 h at 1050 °C (a), 1150 °C (b), 1200 °C (c), 1250 °C (d), as well as CS samples sintered for 2 h at 1050 °C (e), 1150 °C (f), 1200 °C (g), 1250 °C (h), extracted values for strut porosity αs are listed underneath. The scale bars associated with all images is shown in a). The extracted values for grain size g1 are 1.0 ± 0.1 µm for all samples.

Table 4.1 Sintering conditions and corresponding strut porosities αs and overall porosities α.

| | **sintering condition** | **strut porosity $\alpha_s$** | **overall porosities α (3D scaffold)** |
|---|---|---|---|
| **AM** | 1050 °C – 2 h | 50.6 ± 1.4 % | 63.3 ± 0.5 % |
| | 1150 °C – 2 h | 40.3 ± 0.9 % | 58.4 ± 0.2 % |
| | 1200 °C – 2 h | 35.9 ± 0.9 % | 55.3 ± 0.7 % |
| | 1250 °C – 2 h | 32.5 ± 0.5 % | 49.4 ± 0.4 % |
| **CS** | 1050 °C – 2 h | 35.4 ± 1.5 % | |
| | 1150 °C – 2 h | 26.3 ± 0.9 % | |
| | 1200 °C – 2 h | 22.7 ± 1.4 % | |
| | 1250 °C – 2 h | 3.0 ± 0.1 % | |

Next, the effect of sintering temperature and hence porosity of BT samples on piezoelectric properties will be discussed. Figure 4.7 shows the electromechanical and dielectric properties of the AM and CS samples. The hysteresis loops of polarization (a, e), strain (b, f), relative permittivity (c, g) and piezoelectric coefficient $d_{33}$ (d, h) of the AM and the CS samples sintered at 1050 °C, 1150 °C and 1250 °C, respectively, are displayed as a function of the applied electric field strength (see Figure 4.12 for samples sintered at 1200 °C and 1300 °C).

The AM samples show a generally low maximum polarization between 4.90 µC/cm² for 1250 °C and 2.29 µC/cm² for 1050 °C, i.e. polarization decreases with increasing porosity. Similarly, the remanent polarization decreases from 2.30 µC/cm² to 1.70 µC/cm² and the coercive field from 0.13 kV/mm to 0.51 kV/mm, respectively. The strain loops exhibit a typical butterfly shape and are symmetrical, except for the 1050 °C sample. The samples show maximum strain values of about 0.05 % independent of the degree of porosity. Only the strain loop for the AM sample with the lowest porosity of α = 49 % shows a lower maximum strain value. This indicates a loss of electromechanical coupling due to a loss of connectivity. The remanent relative permittivity dramatically decreases with increasing porosity, from 2790 for α = 49 % to 619 for α = 63 %. However, at the maximum applied electric field, the AM samples show no significant difference with values between 461 for 1050 °C and 680 for 1250 °C in relative permittivity. The remanent piezoelectric strain coefficient $d_{33rem}$ value is relevant for this work because it indicates the amount of charge that the BT samples could retain and provide, e.g. to either stimulate surrounding cellular tissue when used as an active bone repair material or to accumulate charge when used as energy harvesting material. The AM sample sintered at 1150 °C with a porosity of 58 % shows the highest $d_{33rem}$ value of 330 pC/N. At both higher and lower porosities, the $d_{33rem}$ values are lower (101 pC/N for 1050 °C and 234 pC/N for 1250 °C). This occurs due to the reduced electromechanical coupling, as mentioned before in the context of electric field induced strain for high porosities. The decrease of $d_{33rem}$ for lower porosities results from a changed electric field dependent behavior. When porosity increases the $d_{33rem}$ loop becomes wider with higher remanent values. For increasing electric fields, the values are similar, indicating a high electromechanical coupling up to rather high porosities.

For the CS samples, a more pronounced influence of the porosity on the electromechanical and dielectric properties is observed. All parameters significantly increase with decreasing porosity and the dense sample shows the highest values. While the increase in polarization and permittivity are dramatic compared to the AM samples, the strain and piezoelectric coefficient have similar values compared to the AM samples. Only the dense CS sample surpasses the AM samples in maximum strain and the piezoelectric coefficient reaches similar values for the dense CS and the AM samples. The maximum polarization of the CS samples increases from 2.38 µC/cm² to 18.50 µC/cm², the remanent polarization from 0.80 µC/cm² to 9.84 µC/cm² with decreasing porosity. The coercive field, on the other hand, shows only a small decrease from 0.28 kV/mm to 0.21 kV/mm. The strain loops have a butterfly shape and are symmetrical. The maximum strain increases with decreasing porosity from 0.016 % to 0.076 %. This clearly demonstrates the strong influence of reduced electromechanical coupling in samples without particle networks. The permittivity loops show an increase in remanent relative permittivity from 1312 to 9126 with decreasing porosity. In addition, the permittivity at maximum electric field increases with decreasing porosity from 1154 to 2849. The dense CS sample sintered at 1250 °C shows the highest $d_{33rem}$ value of 377 pC/N.

Air has a significantly lower permittivity than ceramic materials and the permittivity of a porous ceramic is generally given as product of bulk permittivity and porosity. [138] This is not true for the data shown in Figure 4.7. While the high field permittivity clearly increases with decreasing porosity and follows the approximation of the overall permittivity being a product of the bulk permittivity and the porosity, the remanent relative permittivity is not simply proportional to porosity. Even though the permittivity increases with decreasing porosity, AM and CS samples behave very differently. Obviously, the sample microstructure plays a significant role. This is also reflected in the large-signal strain measurements. While the strain hysteresis of the AM samples remains almost constant, the CS samples exhibit a significant decrease of the strain output with increasing porosity. This effect is even more pronounced for the small-signal piezoelectric coefficient. Here, increasing porosity in the AM samples first leads to an increase in $d_{33}$ and a subsequent reduction. For the CS samples $d_{33}$ continuously decreases with increasing porosity and significantly lower absolute values are observed. This shows that especially the mechanical coupling in the AM samples can be maintained up to high levels of porosity, while the dielectric response is suppressed by the porosity. The reason for the strong electromechanical coupling in the AM samples is the ordered particle network in the porous struts and the mechanical stability of the log-pile structure. So far, only cellular structures fabricated from CapS based inks using AM allow for this micro- and mesostructural tailoring. AM enables these unique microstructural interactions and the corresponding unique mechanical 3-3 structure with a 3-3 strut structure that show 1-3 electromechanical properties.

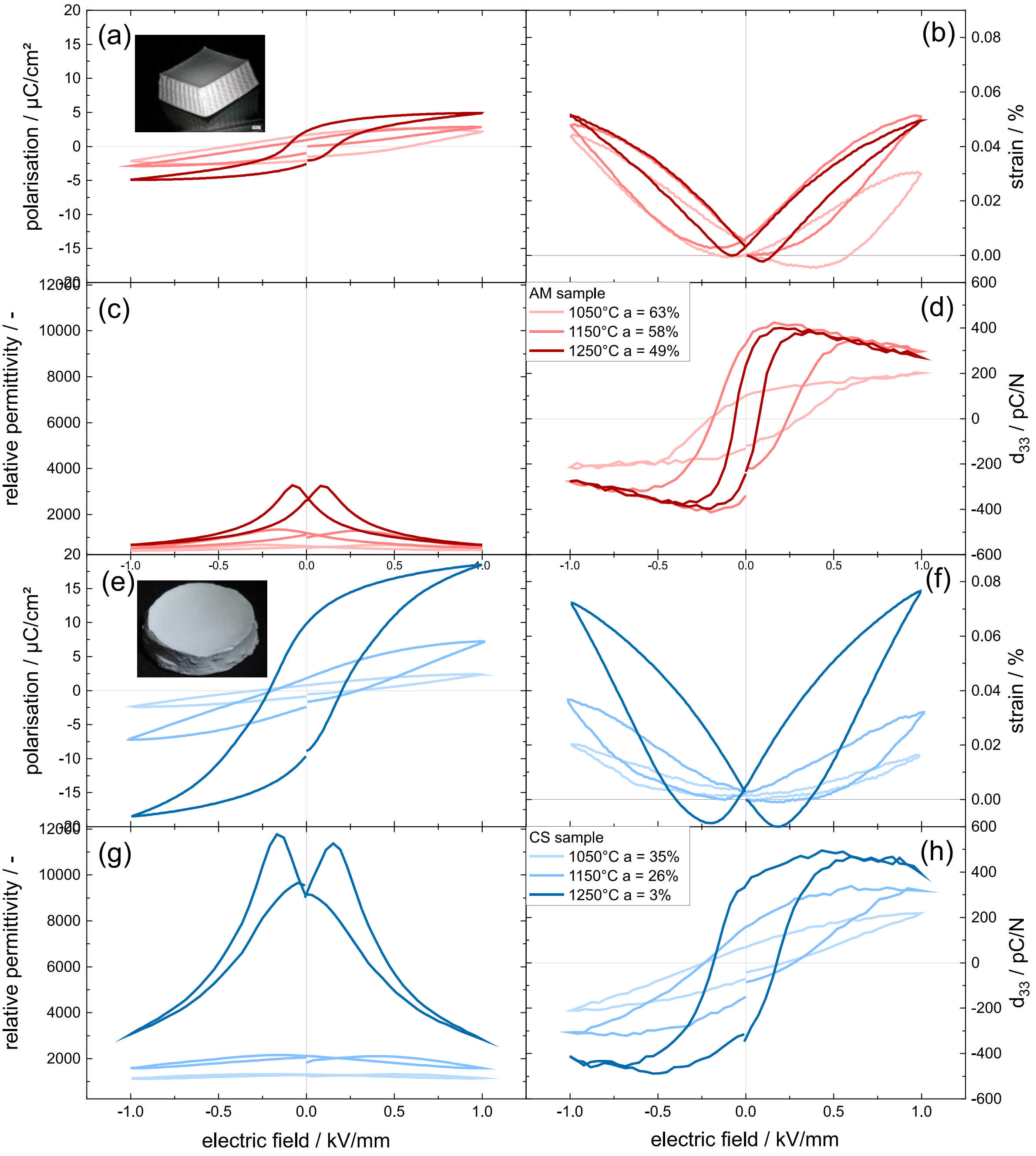

Figure 4.7 Polarization (a, e), strain (b, f), relative permittivity (c, g), and $d_{33}$ hysteresis (d, h) loops of AM and CS BT samples. Polarization and capacitance using a single loop, no prepolarization, and a hysteresis frequency of 1 Hz. Piezoelectric coefficient was measured using a small frequency and amplitude of 1 kHz and 30 V for the dense pellets (1.0 mm height) and 94 V for 3D-structures (3.1 mm height).

For bone substitutes, the $d_{33}$ value is relevant and can be directly compared with the value of bone. [103] For sensing or energy harvesting applications, however, the $FOM_{33}$ is the relevant parameter. [132, 138] This quantity directly depends on the $d_{33}$ value and the relative permittivity (see Equation (11)). The higher the $d_{33}$ and the lower the relative permittivity, the higher values are achieved for the $FOM_{33}$.

Figure 4.8 displays the values of the coefficients $d_{33}$, remanent relative permittivity and $FOM_{33}$ for the AM and CS samples sintered at different temperatures. The relevant electromechanical and dielectric characteristics are summarized in Table 4.2. Figure 4.8 indicates the continuous increase of electromechanical properties for the CS sample with decreasing porosity. The AM samples exhibit lower permittivity values due to their overall higher porosity, but the trend upon variation of porosity is the same as for the CS samples. For the piezoelectric coefficient, however, a completely different behavior appears. Here maximum levels of piezoelectric strain coefficients $d_{33}$ are reached for the AM samples at intermediate sintering temperatures. At these temperatures the sintering activity is high enough to firmly connect the ordered particle network but still maintains a high level of porosity, finally resulting in high $d_{33}$ and hence high $FOM_{33}$ values. In contrast, for the CS samples, the $d_{33rem}$ values increase alongside with the strongly increasing remanent relative permittivity. As a result, the $FOM_{33}$ remains at a relatively low value for all sintering temperatures, i.e. increasing the degree of sintering has no significant effect on the $FOM_{33}$ of the CS samples.

These results show that the combination of a log-pile structure and an ordered particle network fosters high electromechanical coupling with simultaneous low dielectric response. Printing a log-pile structure from a normal two-phase BT ink would require either a higher particle loading or the use of suitable binders. This would lead to a lower porosity and thus to a lower $FOM_{33}$ as well as to different debinding and sintering conditions. The strong deviation between electromechanical and dielectric response leads to a dramatic increase in $FOM_{33}$ and outperforms current concepts for electromechanical energy harvesting applications, electrode materials for batteries or fuel cells, thermoelectrics or bone tissue engineering based on BT.

According to Equation (11), $FOM_{33}$ depends quadratically on the piezoelectric coefficient $d_{33rem}$, while the relative permittivity enters only with the first power. Accordingly, the $FOM_{33}$ values increase drastically with increasing $d_{33rem}$. This is the case for the AM samples at 1150 °C and 1200 °C and the values of the remanent relative permittivity increase only slightly. Both samples show a large $d_{33rem}$ value, whereas the remanent relative permittivity still remains low according to the high porosity of these samples ($\alpha = 58$ % and 55 %, resp.). This results in $FOM_{33}$ values as high as 10.28 pC²/N and

6.50 pC²/N, respectively. For BT, such high $FOM_{33}$ values have not yet been documented. [102] The $FOM_{33}$value of the AM sample at 1150 °C is more than four times higher than any reported value and around 3 times higher than the theoretical maximum value for an ideal 2-2 structure. [102] With materials more optimised for energy harvesting these values can potentially be increased dramatically. [138]

To understand why such high $FOM_{33}$ values are achieved with our CapS based 3D printed porous ceramics, we have to consider the origin of the high $d_{33rem}$ value and at the same time relatively low remanent relative permittivity. The high $d_{33rem}$ value is a result of the sample spanning particle network induced by CapS with grain-connecting necks that just formed at the sintering temperature of 1150 °C (see Figure 4.5). The grains that make up a ceramic material are usually randomly distributed with respect to the orientation of their crystallographic axis. When exposed to an electric field each grain as such wants to deform in a direction dictated by the angle between electric field vector and crystallographic axis. In dense ceramics, however, the local stress distribution in a grain is highly heterogeneous and determined by the surrounding grains, grain boundaries, domain walls and defects. This local stress state contributes significantly to the way a single grain can deform when an electric field is applied. [139] Both an enhancement as well as an inhibition of the local piezoelectric response is possible, however the macroscopic piezoelectric response is reduced. [140]

In the present case, the clamping effect on each grain is minimized due to the highly porous structure that allows the grains to freely respond to the applied electric field. This way even large anisotropic strains can fully develop. At the same time, necking between the particles has evolved to a degree that allows sufficient electric field distribution throughout the whole sample to trigger the observed piezoelectric response.

The low relative permittivity can be directly attributed to the high overall porosity, which occurs on different length scales: on the one hand the CapS ink enables a high porosity of about 40 % within the printed struts with pore sizes in the lower µm range (< 5 µm), and on the other hand of the 3D printed log-pile structure with macropores in the range of several hundred µm, due to the mechanical strength of the CapS ink, we were able to print with a strut/pore diameter of approx. 1:6 (70 µm strut and 440 µm pore diameter) and achieve the resulting free spaces (see Figure 4.10).

Table 4.2 Relevant values for maximum polarization (high field) ($P_{max}$), remanent polarization ($P_{rem}$), coercive electric field ($E_c$), remanent relative permittivity ($\varepsilon_{rem}$), maximum relative permittivity (high field, $\varepsilon_{max}$), maximum strain (high field, $S_{max}$), remanent strain ($S_{rem}$), remanent piezoelectric strain coefficient $d_{33rem}$ and maximum piezoelectric strain coefficient $d_{33max}$ (high field).

| | $T_s$ [°C] | $P_{max}$ [µC/cm$^2$] | $P_{rem}$ [µC/cm$^2$] | $S_{max}$ [%] | $S_{rem}$ [%] | $E_c$ [kV/mm] | $\varepsilon_{rem}$ [-] | $\varepsilon_{max}$ [-] | $d_{33rem}$ [pC/N] | $d_{33max}$ [pC/N] |
|---|---|---|---|---|---|---|---|---|---|---|
| **AM** | 1050 | 2.2 | 1.7 | 0.030 | 4.3E-4 | 0.51 | 619 | 462 | 101 | 201 |
| | 1150 | 2.9 | 1.0 | 0.051 | 64.7E-4 | 0.22 | 1197 | 564 | 330 | 297 |
| | 1200 | 3.3 | 1.8 | 0.053 | 19.4E-4 | 0.30 | 1657 | 732 | 309 | 312 |
| | 1250 | 4.9 | 2.3 | 0.049 | 35.7E-4 | 0.13 | 2791 | 680 | 234 | 270 |
| | 1300 | 5.3 | 2.0 | 0.047 | 16.9E-4 | 0.07 | 3495 | 858 | 145 | 266 |
| **CS** | 1050 | 2.4 | 0.8 | 0.016 | 13.9E-4 | 0.28 | 1312 | 1154 | 68 | 218 |
| | 1150 | 7.2 | 1.9 | 0.032 | 25.3E-4 | 0.24 | 2125 | 1593 | 157 | 317 |
| | 1200 | 7.2 | 1.9 | 0.032 | 24.9E-4 | 0.24 | 3627 | 2661 | 147 | 355 |
| | 1250 | 18.4 | 9.8 | 0.076 | 47.3E-4 | 0.21 | 9126 | 2849 | 377 | 394 |
| | 1300 | 16.4 | 6.5 | 0.070 | 64.7E-4 | 0.10 | 5104 | 2423 | 175 | 403 |

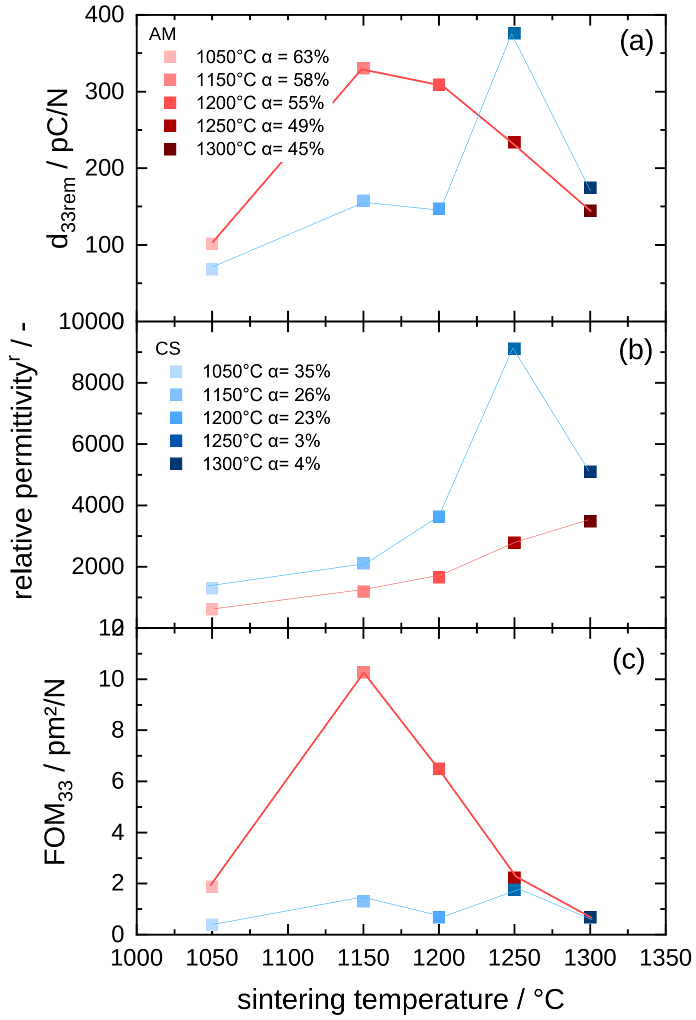

Figure 4.8 Summarized values of $d_{33rem}$ (a), remanent relative permittivity (b) and $FOM_{33}$ (c) values as a function of the sintering temperature for AM and CS samples. in addition, the porosity α of the respective sample is shown in the legend

In Figure 4.9, the $FOM_{33}$ values from our work are compared with the highest values from others [102, 141] achieved with BT. In addition, two models have been included: an ideal 2-2 model and model predicting $FOM_{33}$ from the intrinsic material properties and assuming uniform porosity [102].

With the method presented here, the combination of capillary suspensions and additive manufacturing, we achieve $FOM_{33}$ values that are 486 % higher than those of dense ceramics. This is far above all previously documented values for BT material. Even the models shown in literature are clearly below the potential we have demonstrated.

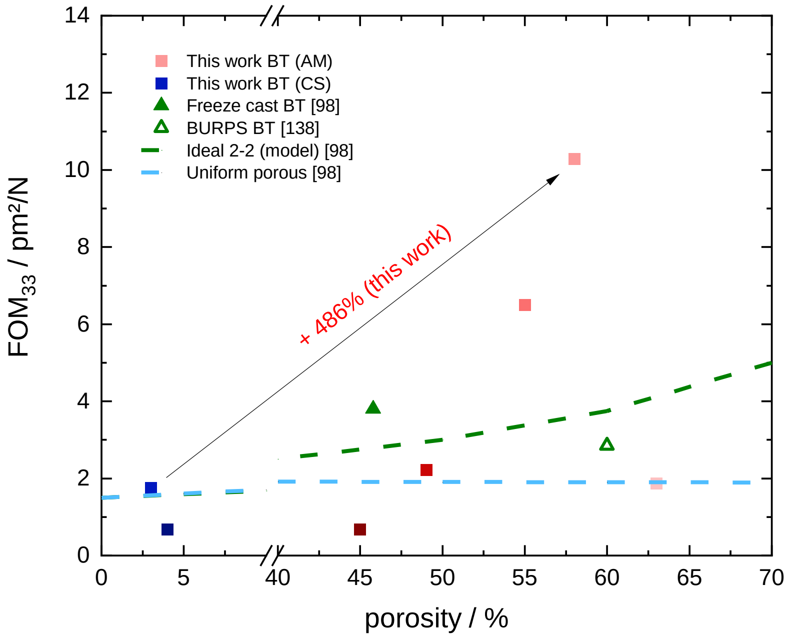

Figure 4.9 Energy harvesting figure of merit as a function of porosity. Comparison of AM and CS samples with freeze casted [102], uniform porous burned out polymer spheres (BURPS) [142] BT samples and two models: a model predicting $FOM_{33}$ from the intrinsic material properties assuming an ideal 2-2 structure and a model assuming uniform porosity.

## 4.5 Conclusion

DIW is a feasible method for manufacturing complex hierarchical structures from piezoelectric materials for applications in the field of electromechanical energy harvesting or bone tissue engineering with piezoelectrically stimulated cell growth. Depending on the application, the properties can be specifically tailored by 3D printing. Here we focus on the fabrication of highly open porous, hierarchically structured BT ceramics via DIW using CapS type BT inks providing a unique pore structure in the printed struts. Dedicated sintering of the printed objects with complex hierarchical structure and 3-3 connectivity yields unusual piezoelectric functionality. A step-wise heat treatment between 1050 °C and 1300 °C is employed, resulting in different degrees of sintering. The AM sample sintered at 1150 °C was found to show an overall porosity of 58 % and at the same time the highest $d_{33rem}$ value of 330 pC $N^{-1}$ which is comparable to dense BT. At the same time this sample was found to show a remanent relative permittivity of 1197, resulting in a high energy harvesting figure of merit - $FOM_{33}$ of 10.3 $pm^2$ $N^{-1}$, more than four times higher than documented data for this particular material. This is rationalized by the distinct sample spanning network formed in the porous, sintered ceramics made from CapS-type inks. In order to exploit the full potential of this technology material composition as well as the 3D printed geometry may be further optimized. The generic concept of combining AM with self-assembly based on capillary forces in the printing ink may also be applied to create thermoelectric materials as well as electrode materials for fuel cells and solid-state batteries in order to achieve complex hierarchical structures with unprecedented functionality.

## 4.6 Acknowledgments

D. Menne would like to thank Deutsche Forschungsgemeinschaft (DFG) for funding under grant no. HI 1867/1-2 and WI 3138/26-1 and the Karlsruhe House of Young Scientists for the financial support that included travel expenses and allowed for the collaboration between Karlsruhe Institute of Technology and Norwegian University of Science and Technology.

D. Menne also wants to thank and gratefully acknowledge Ragnvald Mathiesen for the fruitful discussions regarding the X-ray experiments and the kind assistance of Ole Tore at the X-ray laboratory at NTNU.

Thanks also to Felipe Buffa-Fehr and Anna Koltsova (both KIT) for contributing to the ceramic characterization, paste preparation and 3D printing.

## 4.7 Supporting information

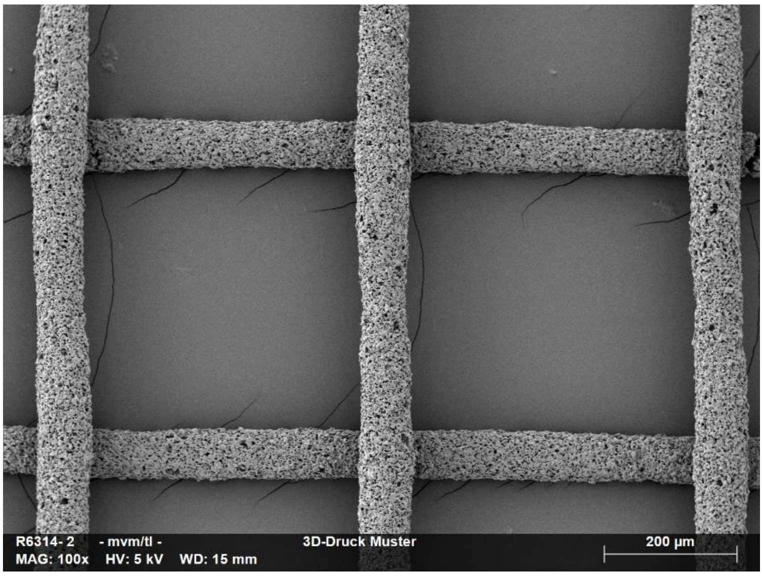

Figure 4.10 SEM top view of an AM log-pile structure with printed strut widths ≈ 70 µm.

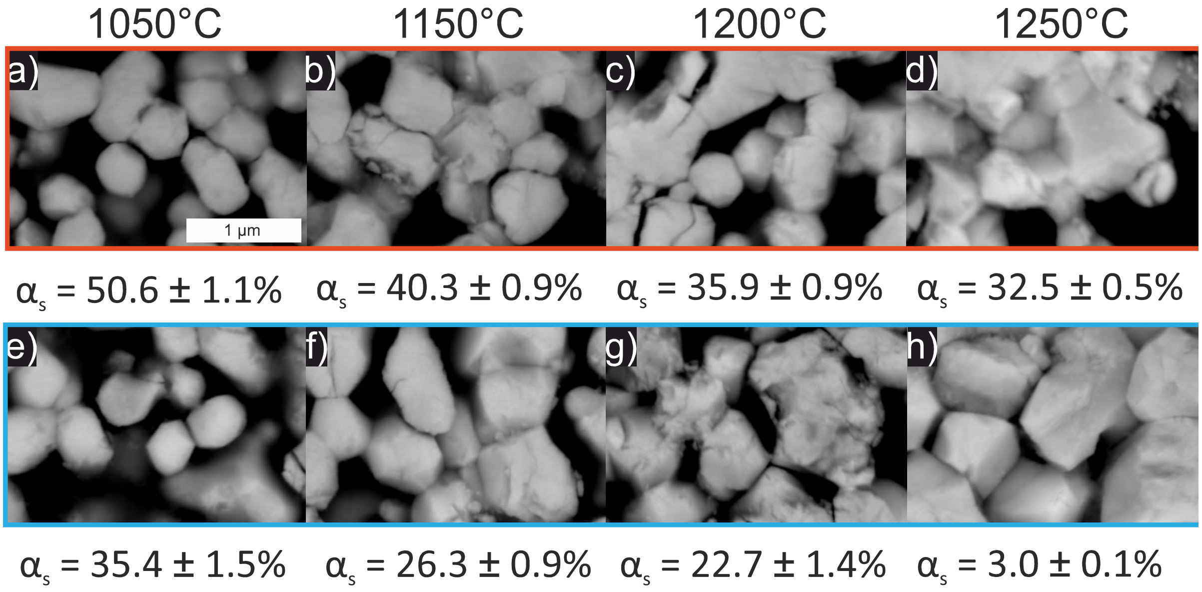

Figure 4.11 Crosscut SEM images showing the microstructure of AM samples sintered for 2 h at 1050 °C (a), 1150 °C (b), 1200 °C (c), 1250 °C (d), as well as CS samples sintered for 2 h at 1050 °C (e), 1150 °C (f), 1200 °C (g), 1250 °C (h), extracted values for strut porosity $\alpha_s$ are listed underneath. The scale bars associated with all images is shown in a

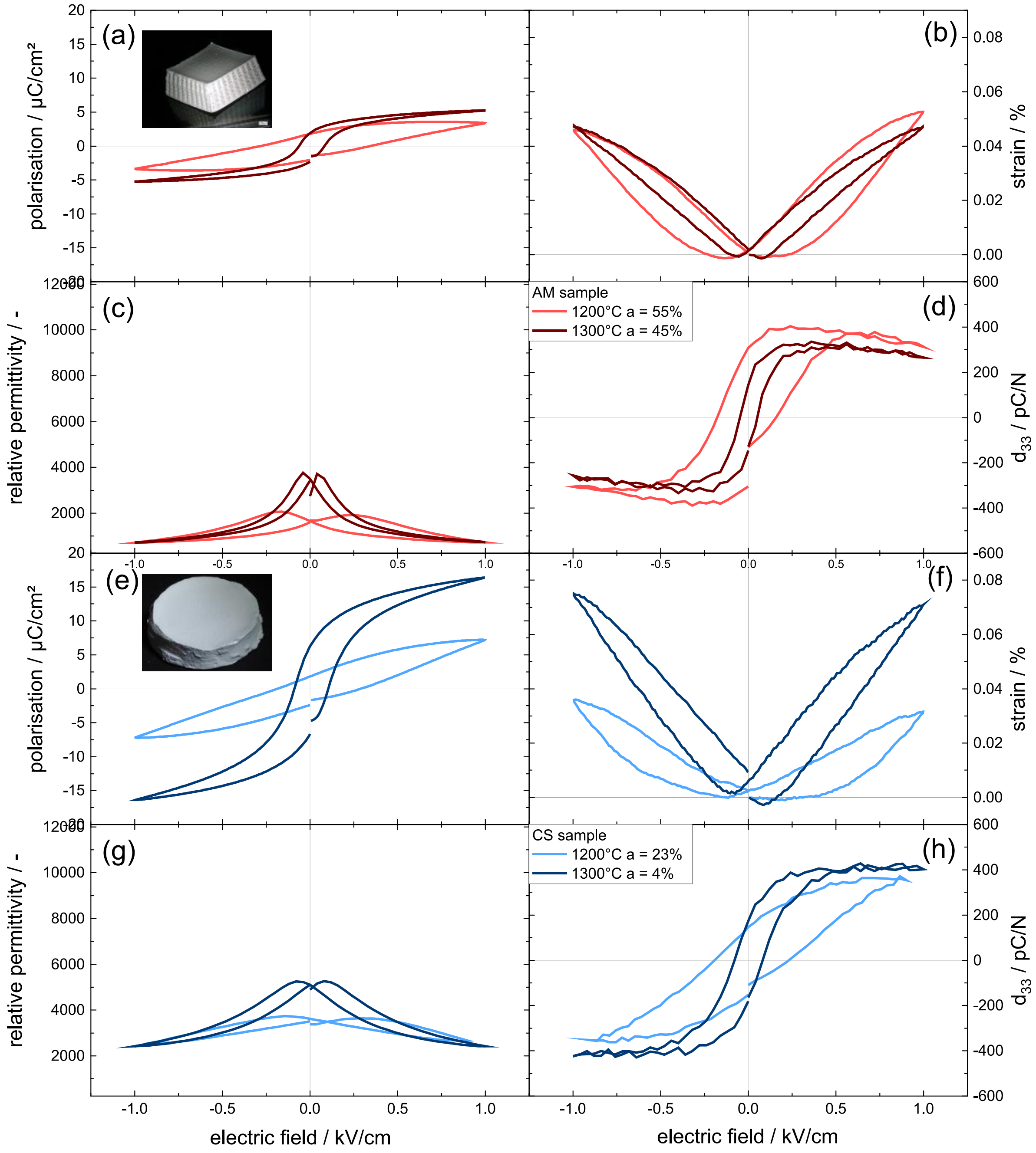

Figure 4.12 Polarization (a, e), strain (b, f), relative permittivity (c, g), and $d_{33}$ hysteresis (d, h) loops of AM and CS BT samples. Polarization and capacitance using a single loop, no prepolarization, and a hysteresis frequency of 1 Hz. Piezoelectric coefficient was measured using a small frequency and amplitude of 1 kHz and 30 V for the dense pellet (1.0 mm height) and 94 V for 3D-structures (3.1 mm height).

# 5 Summary

The novel processing route of manufacturing highly porous ceramics using capillary suspensions (CapS) as precursor, was first introduced by Dittmann *et al.* in 2012 [17]. With this concept, macroporous ceramics with porosities > 50 % and pore sizes in the range between 0.5 and 50 µmcan be flexibly adjusted. 10 years after the concept was introduced, in this dissertation we are presenting the first product using a porous ceramic based on CapS that has been developed to market readiness. Furthermore, in this dissertation we extend the range of applications of porous ceramics based on CapS from structural ceramics to the field of functional ceramics, that were not in the focus of other researchers, so far. The main results of this cumulative dissertation are divided into two parts.

In **part I** of this thesis a novel soil water potential sensor was developed and tested in collaboration with TRUEBNER GmbH, a manufacturer of soil moisture sensors. This device measures plant-available water, i.e. the soil water potential and can therefore be used to optimize irrigation in agriculture. The sensor consists of a printed circuit board with tailored electronic layout and two porous ceramic discs mounted on it. The highly porous (> 69 ± 0.1 %) ceramic discs show a sufficient high mechanical strength (> 6 ± 1 MPa) and a broad pore size distribution (0.5 to 200 µm) and were developed using capillary suspensions as precursors. The new circuit board system was build using a transmission line within a time-domain transmission circuit. In this way, a change in dielectric response of the ceramic discs with changing water uptake is detected. The concept was proven by carrying out multiple laboratory and field experiments in a wide range of soil types, which demonstrated the versatility of the sensor. In this way, it was confirmed that the signal of the new sensor correlates with the soil water potential irrespective of soil composition and is thus suitable for the optimization of irrigation systems. By comparing the new sensor with commercial soil water potentials- and soil moisture sensors, it was confirmed that the new sensor provides accurate and reliable results. In particular, in the experiments with controlled irrigation it was shown that the new sensor provides data with high accuracy and low scatter. A universal empirical relationship was established between the output signal of the new sensor and the soil water potential determined with a T8 tensiometer through a comparative study with three very different soil types. Through this, a determination of the soil water potential without knowledge of the soil composition is possible with the new sensor.

In **part II** of this thesis for the first time a porous electroceramic was manufactured using CapS as precursor. The CapS were optimized for the use in the 3D printing process direct ink writing in such a way that previously unattained strut to pore ratio of approx. 1:6 (70 µm strut and 440 µm pore diameter) were achieved. In this way, highly open porous hierarchically structured barium titanate ceramics with closed bottom and top layers and inner 3-3 connectivity were manufactured. Here, the printed mesostructure (~100 µm) was combined with a pore size of the printed struts (~1 µm), resulting in overall porosities of > 60 %. Employing a step-wise heat treatment between 1050 °C and 1300 °C, resulted in different degrees of sintering. The 3D printed sample sintered at 1150 °C showed an overall porosity of 58 % and at the same time the highest $d_{33rem}$ value of 330 pC $N^{-1}$ which is comparable to dense barium titanate. At the same time this sample was found to show remanent relative permittivity of 1197, resulting in a high energy harvesting figure of merit of 10.3 $pm^2$ $N^{-1}$, which is more than four times higher than documented data for this particular material. The high $d_{33rem}$ value is a result of the sample spanning particle network induced by CapS, with grain-connecting necks that just formed at the sintering temperature of 1150 °C. Here, the clamping effect on each grain is minimized due to the highly porous structure that allows the grains to freely respond to the applied electric field. At the same time, the sintering necks between the particles have evolved to a degree that allows sufficient electric field distribution throughout the whole sample to trigger the observed piezoelectric response. In this way, it was proven, that by combining the microstructural properties of the CapS with a printed structure using additive manufacturing, the piezoelectric and electromechanical properties of electroceramic can be tuned to a previously unattained level.

# 6 Outlook

## 6.1 Soil water potential sensor

In this dissertation in chapter 3, a soil water potential sensor with a porous ceramic based on CapS as the main component was developed. In a number of laboratory and field experiments it could be shown that the sensor works up to a soil water potential of 1000 hPa and shows low scatter in the measurement signal. In future work, the ceramic could be further optimized so that the sensor can be used up to soil water potential of 15 000 hPa. This could be relevant for research in soil science as it is the permanent wilting point [143]. For this purpose, the pore size distribution, which has been relatively broad up to now, would have to be expanded, especially in the number of smaller pores (< 10 µm). The ceramic could be produced, for example, by particle mixtures of kieselgur with different particle sizes. One possibility would be to add particles with an average particle diameter of < 20 µm. In this way, the sensor could also be used in particular for optimized irrigation in very fine-grained soils. In addition, there is still a need for development in the calibration of the sensors. The current sensors are calibrated individually. In future work, a sensor-independent calibration could be implemented. For this, it must be ensured in production that, on the one hand, the circuit boards do not differ significantly from one another and, on the other hand, the microstructure of the ceramics is always comparable in all ceramic discs.

## 6.2 Additive Manufacturing of Caps

### 6.2.1 Electroceramics

In Chapter 4 of this thesis, the functional properties of an electroceramic were significantly improved by the unique particle network of the CapS and by using additive manufacturing. A commercial BT powder was used to produce the porous ceramics. Compared to other electroceramics, BT has a lower maximum $d_{33}$ value. Solid solutions of BT-based ceramics with $CaZrO_3$ ($Ba_{1-x}Ca_xZr_{1-y}Ti_yO_3$, BCZT) already reach excellent piezoelectric properties with $d_{33}$ values > 500 pC/N [144]. For this reason, in future work CapS type pastes should be developed with BCZT as solid content, 3D printed and investigated for their electrical properties.

In this work the 3D printed log-pile structures with closed top and bottom were not explicitly optimized in their geometrical design to achieve maximum functional properties. Therefore, there is still a need to explore what structure of the 3D printed components would yield higher $d_{33}$- and lower permittivity values. In particular, the geometry should be adjusted to maximize the $d_{33}$ value and minimize the permittivity. One possible strategy could be to maximize the printed pore sizes of the objects. The larger the spanning factor of the printed struts in the component, the larger the pores and the lower the permeability will be. Based on the work presented here, new piezoelectric devices may be designed opening up new technological opportunities, especially in the field of energy harvesting.

The rheological properties of the CapS produced in this work were adapted for 3D printing. For this reason, neither the solid content nor the second-phase content were varied in the paste formulation for subsequent investigations of the functional properties of the manufactured ceramics. However, these two parameters in particular allow the microstructural properties of the particle network of the CapS to be strongly changed. The three regimes I, II and III of the CapS show distinct structural differences. In further work the influence of these structural differences on the functional properties of electroceramics should be investigated. Printable formulations should be accessible in all three regimes.

### 6.2.2 Bioactive Materials

CapS can be used to produce macroporous ceramics with pore sizes between 0.5 and 100 µm. With the use of CapS in 3D printing, the range of printed pores can be increased to > 100 µm by selecting a suitable cellular structure. In the bone tissue engineering field, scaffolds made of osteoconductive and resorbable materials, such as ß-tricalcium phosphate, bioactive glass or hydroxyapatite, are used. In order to guarantee cell growth, the use of these materials is recommended with pores in the range of 300 – 500 µm [145, 146] or, in recent studies, in the range of 700 – 1200 µm [147]. The ceramic material can serve both as a support structure and, depending on the choice of material, as a nutrient medium for the cells. Since CapS can be used to 3D print hierarchical structures and there are no restrictions on the material to be used, CapS could be suitable for the production of bone replacement materials.

In the field of bone replacement materials in combination with 3D printed CapS the following questions could be investigated: influence of strut porosity on cell growth [148, 149], influence of 3d printed strut sizes, pore size and shape on cell growth, influence of rough surface induced by CapS on adhesion and growth of cells, influence of nanoparticles like SiO2, TiO2 MgO or ZnO included in the secondary liquid on cell growth, and the effect of the nanoparticles on the mechanical strength and the sintering properties of the material [150].

To take a first step in this direction, preliminary tests were carried out with two different materials. On the one hand commercial grade beta tricalciumphosphat (TCP) C13-13 (Chemische Fabrik Budenheim KG, Budenheim, Germany) with an average particle size of $x_{50,3}$ = 3.3 µm, according to Fraunhofer diffraction, and a density of $\rho$ = 3.4 g/cm³ was used. On the other hand, commercial grade bioactive glass 45S5 Bioglass® product name Vitryxx® (SCHOTT AG, Mainz, Germany) with an average particle size of $x_{50,3}$ = 4.98 µm, according to Fraunhofer diffraction, and a density of $\rho$ = 2.7 g/cm³ was employed for paste formulation.

Based on these two materials CapS were produced suitable for 3D printing in a first run. The composition of these material systems was based on the composition described in [40]. Cellular structures were printed using a nozzle with inner diameters of 150 µm for both systems. In preliminary tests TCP honey comb structures with densities > 128 kg/m³ and triangular structures with densities > 250 kg/m³ were printed (see Figure 6.1 A and B). The bioactive glass material was used to print 3D structures with a gradient in pore sizes to mimic the bone structure (see Figure 6.1 C). In the middle row of Figure 6.1, SEM images are shown of 3D printed TCP log pile structures with printed strut diameters of 70 µm (D) and a magnification of such a strut (E). In Figure 6.1 (F) a crosscut image of a printed strut with a diameter of 70 µm with the unique microstructure of sintered capillary suspensions is shown. The bottom row shows a 3D printed TCP log-pile scaffold (G), and a SEM picture of the broken up scaffold with human mesenchymal stem cells (hMSC) placed inside the scaffold (H) and a magnification of the cell (I). These preliminary experiments show that the cells adhere to the porous surface structure in the 3D printed scaffold. In further work cell viability- and proliferation experiments should be performed in both the TCP and bioactive glass structures. The aim should be to investigate whether the particle network created by CapS, the resulting pores and the surface roughness and surface structure promote cell growth. In this way, CapS-based components could serve as scaffolds in the body to regenerate bone defects more quickly or experiments on cell and bone growth could be carried out to develop bone disease models [151, 152].

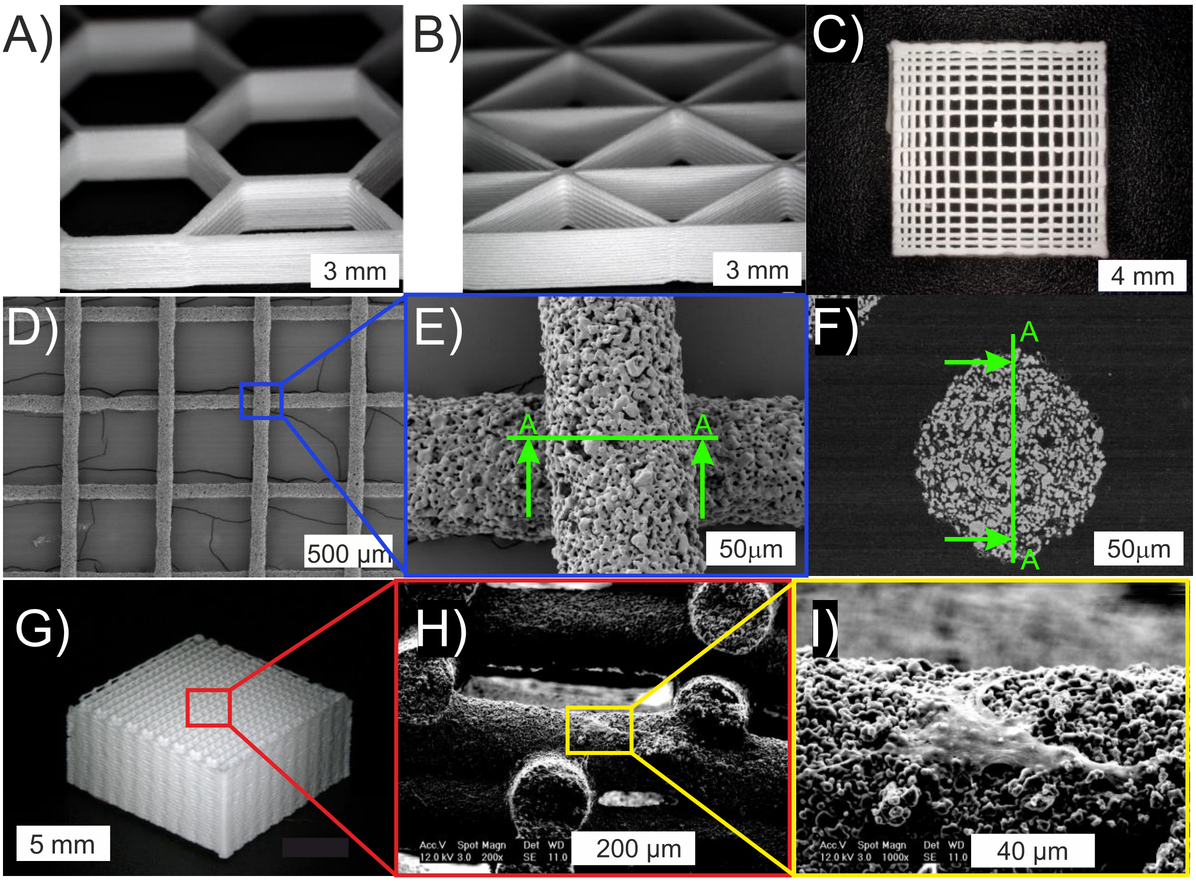

Figure 6.1 3D printed and sintered structures using CapS-based inks: TCP honeycomb structures (A), TCP triangular structures (B), bioglass® structure with varied printed pre sizes (C), SEM picture of TCP struts with a 70 µm diameter (D & E), crosscut through TCP strut (F), TCP log-pile scaffold (G), SEM picture of adhered hMSC on TCP strut in 3D printed log-pile scaffold (H and I).

# 7 Biblography

[1] Ohji, T.; Fukushima, M. Macro-Porous Ceramics: Processing and Properties. *Int. Mater. Rev.*, **2012**, *57* (2), 115–131.

[2] Studart, A. R.; Gonzenbach, U. T.; Tervoort, E.; Gauckler, L. J. Processing Routes to Macroporous Ceramics: A Review. *J. Am. Ceram. Soc.*, **2006**, *89* (6), 1771–1789.

[3] Somiya, S. *Handbook of Advanced Ceramics: Materials, Applications, Processing, and Properties: Second Edition*; Academic press, 2013.

[4] Salmang, H.; Scholze, H.; Telle, R. *Keramik*; Springer, 1982.

[5] Hwa, L. C.; Rajoo, S.; Noor, A. M.; Ahmad, N.; Uday, M. B. Recent Advances in 3D Printing of Porous Ceramics: A Review. *Curr. Opin. Solid State Mater. Sci.*, **2017**, *21* (6), 323–347.

[6] Scheffler, M.; Colombo, P. *Cellular Ceramics: Structure, Manufacturing, Properties and Applications*; John Wiley & Sons, 2006.

[7] Hammel, E. C.; Ighodaro, O. L. R.; Okoli, O. I. Processing and Properties of Advanced Porous Ceramics: An Application Based Review. *Ceram. Int.*, **2014**, *40* (10), 15351–15370.

[8] Hwa, L. C.; Rajoo, S.; Noor, A. M.; Ahmad, N.; Uday, M. B. Recent Advances in 3D Printing of Porous Ceramics: A Review. *Curr. Opin. Solid State Mater. Sci.*, **2017**, *21* (6), 323–347.

[9] Akhtar, F.; Andersson, L.; Ogunwumi, S.; Hedin, N.; Bergström, L. Structuring Adsorbents and Catalysts by Processing of Porous Powders. *J. Eur. Ceram. Soc.*, **2014**, *34* (7), 1643–1666.

[10] Castro, N. J.; O'Brien, J.; Zhang, L. G. Integrating Biologically Inspired Nanomaterials and Table-Top Stereolithography for 3D Printed Biomimetic Osteochondral Scaffolds. *Nanoscale*, **2015**, *7* (33), 14010–14022.

[11] Chen, Y.; Wang, N.; Ola, O.; Xia, Y.; Zhu, Y. Porous Ceramics: Light in Weight but Heavy in Energy and Environment Technologies. *Mater. Sci. Eng. R Reports*, **2021**, *143* (August 2020), 100589.

[12] Chung, D. D. L. Materials for Electromagnetic Interference Shielding. *Mater. Chem. Phys.*, **2020**, *255* (April), 123587.

[13] Chen, C.; Wang, X.; Wang, Y.; Yang, D.; Yao, F.; Zhang, W.; Wang, B.; Sewvandi, G. A.; Yang, D.; Hu, D. Additive Manufacturing of Piezoelectric Materials. *Adv. Funct. Mater.*, **2020**, *30* (52), 1–29.

[14] Liang, C.; Wang, Z.; Wu, L.; Zhang, X.; Wang, H.; Wang, Z. Light and Strong Hierarchical Porous SiC Foam for Efficient Electromagnetic Interference Shielding and Thermal Insulation at Elevated Temperatures. *ACS Appl. Mater. Interfaces*, **2017**, *9* (35), 29950–29957.

[15] Zakaria, Z.; Awang Mat, Z.; Abu Hassan, S. H.; Boon Kar, Y. A Review of Solid Oxide Fuel Cell Component Fabrication Methods toward Lowering Temperature. *Int. J. Energy Res.*, **2020**, *44* (2), 594–611.

[16] Dou, L.; Zhang, X.; Cheng, X.; Ma, Z.; Wang, X.; Si, Y.; Yu, J.; Ding, B. Hierarchical Cellular Structured Ceramic Nanofibrous Aerogels with Temperature-Invariant Superelasticity for Thermal Insulation. *ACS Appl. Mater. Interfaces*, **2019**, *11* (32), 29056–29064.

[17] Dittmann, J.; Koos, E.; Willenbacher, N. Ceramic Capillary Suspensions: Novel Processing Route for Macroporous Ceramic Materials. *J. Am. Ceram. Soc.*, **2013**, *96* (2), 391–397.

[18] Koos, E.; Willenbacher, N. Capillary Forces in Suspension Rheology. *Science (80-. ).*, **2011**, *331* (6019), 897–900.

[19] Sun, H.; Han, Z.; Willenbacher, N. Ultrastretchable Conductive Elastomers with a Low Percolation Threshold for Printed Soft Electronics. *ACS Appl. Mater. Interfaces*, **2019**, *11* (41), 38092–38102.

[20] Bitsch, B.; Dittmann, J.; Schmitt, M.; Scharfer, P.; Schabel, W.; Willenbacher, N. A Novel Slurry Concept for the Fabrication of Lithium-Ion Battery Electrodes with Beneficial Properties. *J. Power Sources*, **2014**, *265*, 81–90.

[21] Yüce, C.; Okamoto, K.; Karpowich, L.; Adrian, A.; Willenbacher, N. Non-Volatile Free Silver Paste Formulation for Front-Side Metallization of Silicon Solar Cells. *Sol. Energy Mater. Sol. Cells*, **2019**, *200* (July), 110040.

[22] Dittmann, J.; Willenbacher, N. Micro Structural Investigations and Mechanical Properties of Macro Porous Ceramic Materials from Capillary Suspensions. *J. Am. Ceram. Soc.*, **2014**, *97* (12), 3787–3792.

[23] Dittmann, J.; Maurath, J.; Bitsch, B.; Willenbacher, N. Highly Porous Materials with Unique Mechanical Properties from Smart Capillary Suspensions. *Adv. Mater.*, **2016**, *28* (8), 1689–1696.

[24] Maurath, J.; Willenbacher, N. 3D Printing of Open-Porous Cellular Ceramics with High Specific Strength. *J. Eur. Ceram. Soc.*, **2017**, *37* (15), 4833–4842.

[25] Maurath, J.; Bitsch, B.; Schwegler, Y.; Willenbacher, N. Influence of Particle Shape on the Rheological Behavior of Three-Phase Non-Brownian Suspensions. *Colloids Surfaces A Physicochem. Eng. Asp.*, **2016**, *497*, 316–326.

[26] Schneider, M.; Maurath, J.; Fischer, S. B.; Weiß, M.; Willenbacher, N.; Koos, E. Suppressing Crack Formation in Particulate Systems by Utilizing Capillary Forces. *ACS Appl. Mater. Interfaces*, **2017**, *9* (12), 11095–11105.

[27] Weiß, M.; Maurath, J.; Willenbacher, N.; Koos, E. Shrinkage and Dimensional Accuracy of Porous Ceramics Derived from Capillary Suspensions. *J. Eur. Ceram. Soc.*, **2019**, *39* (5), 1887–1892.

[28] Weiß, M.; Sälzler, P.; Willenbacher, N.; Koos, E. 3D-Printed Lightweight Ceramics Using Capillary Suspensions with Incorporated Nanoparticles. *J. Eur. Ceram. Soc.*, **2020**, *40* (8), 3140–3147.

[29] Maurath, J. Tailored Formulation of Capillary Suspensions as Precursor for Porous Sintered Materials. **2018**.

[30] Baino, F.; Caddeo, S.; Novajra, G.; Vitale-Brovarone, C. Using Porous Bioceramic Scaffolds to Model Healthy and Osteoporotic Bone. *J. Eur. Ceram. Soc.*, **2016**, *36* (9), 2175–2182.

[31] Zhang, L.; Mao, Z.; Thomason, J. D.; Wang, S.; Huang, K. Synthesis of a Homogeneously Porous Solid Oxide Matrix with Tunable Porosity and Pore Size. *J. Am. Ceram. Soc.*, **2012**, *95* (6), 1832–1837.

[32] Fane, A. G.; Wang, R.; Hu, M. X. Synthetic Membranes for Water Purification: Status and Future. *Angew. Chemie - Int. Ed.*, **2015**, *54* (11), 3368–3386.

[33] Vijayan, S.; Narasimman, R.; Prabhakaran, K. Freeze Gelcasting of Hydrogenated Vegetable Oil-in-Aqueous Alumina Slurry Emulsions for the Preparation of Macroporous Ceramics. *J. Eur. Ceram. Soc.*, **2014**, *34* (16), 4347–4354.

[34] Naviroj, M.; Miller, S. M.; Colombo, P.; Faber, K. T. Directionally Aligned Macroporous SiOC via Freeze Casting of Preceramic Polymers. *J. Eur. Ceram. Soc.*, **2015**, *35* (8), 2225–2232.

[35] Roscow, J. I.; Zhang, Y.; Kraśny, M. J.; Lewis, R. W. C.; Taylor, J.; Bowen, C. R. Freeze Cast Porous Barium Titanate for Enhanced Piezoelectric Energy Harvesting. *J. Phys. D. Appl. Phys.*, **2018**, *51* (22), 323–347.

[36] Pokhrel, A.; Seo, D. N.; Lee, S. T.; Kim, I. J. Processing of Porous Ceramics by Direct Foaming: A Review. *J. Korean Ceram. Soc.*, **2013**, *50* (2), 93–102.

[37] Shimamura, A.; Fukushima, M.; Hotta, M.; Ohji, T.; Kondo, N. Fabrication and Characterization of Porous Alumina with Denser Surface Layer by Direct Foaming. *J. Ceram. Soc. Japan*, **2017**, *125* (1), 7–11.

[38] Huo, W.; Zhang, X.; Tervoort, E.; Gantenbein, S.; Yang, J.; Studart, A. R. Ultrastrong Hierarchical Porous Materials via Colloidal Assembly and Oxidation of Metal Particles. *Adv. Funct. Mater.*, **2020**, *30* (38).

[39] Roman-Manso, B.; Muth, J.; Gibson, L. J.; Ruettinger, W.; Lewis, J. A. Hierarchically Porous Ceramics via Direct Writing of Binary Colloidal Gel Foams. *ACS Appl. Mater. Interfaces*, **2021**, *13* (7), 8976–8984.

[40] Menne, D.; Lemos da Silva, L.; Rotan, M.; Glaum, J.; Hinterstein, M.; Willenbacher, N. Giant Functional Properties in Porous Electroceramics through Additive Manufacturing of Capillary Suspensions. *ACS Appl. Mater. Interfaces*, **2022**, *14* (2), 3027–3037.

[41] Menne, D.; Hübner, C.; Trebbels, D.; Willenbacher, N. A Robust Soil Water Potential Sensor with High Sensitivity and Broad Measuring Range. *2021 13th Int. Conf. Electromagn. Wave Interact. with Water Moist Subst. ISEMA 2021*, **2021**, 1–7.

[42] Menne, D.; Hübner, C.; Trebbels, D.; Willenbacher, N. Robust Soil Water Potential Sensor to Optimize Irrigation in Agriculture. *Sensors*, **2022**, *22* (12).

[43] Koos, E.; Willenbacher, N. Particle Configurations and Gelation in Capillary Suspensions. *Soft Matter*, **2012**, *8* (14), 3988–3994.

[44] Bossler, F.; Koos, E. Structure of Particle Networks in Capillary Suspensions with Wetting and Nonwetting Fluids. *Langmuir*, **2016**, *32* (6), 1489–1501.

[45] Bindgen, S.; Bossler, F.; Allard, J.; Koos, E. Connecting Particle Clustering and Rheology in Attractive Particle Networks. *Soft Matter*, **2020**, *16* (36), 8380–8393.

[46] Pietsch, W.; Rumpf, H. Haftkraft, Kapillardruck, Flüssigkeitsvolumen Und Grenzwinkel Einer Flüssigkeitsbrücke Zwischen Zwei Kugeln. *Chemie Ing. Tech.*, **1967**, *39* (15), 885–893.

[47] Koos, E.; Kannowade, W.; Willenbacher, N. Restructuring and Aging in a Capillary Suspension. *Rheol. Acta*, **2014**, *53* (12), 947–957.

[48] Herminghaus, S. Dynamics of Wet Granular Matter. *Adv. Phys.*, **2005**, *54* (3), 221–261.

[49] Willett, C. D.; Adams, M. J.; Johnson, S. A.; Seville, J. P. K. Capillary Bridges between Two Spherical Bodies. *Langmuir*, **2000**, *16* (24), 9396–9405.

[50] Koos, E. Capillary Suspensions: Particle Networks Formed through the Capillary Force. *Curr. Opin. Colloid Interface Sci.*, **2014**, *19* (6), 575–584.

[51] Bindgen, S.; Allard, J.; Koos, E. The Behavior of Capillary Suspensions at Diverse Length Scales: From Single Capillary Bridges to Bulk. *Curr. Opin. Colloid Interface Sci.*, **2022**, *58*, 1–29.

[52] Maurath, J.; Dittmann, J.; Schultz, N.; Willenbacher, N. Fabrication of Highly Porous Glass Filters Using Capillary Suspension Processing. *Sep. Purif. Technol.*, **2015**, *149*, 470–478.

[53] Compton, B. G.; Lewis, J. A. 3D-Printing of Lightweight Cellular Composites. *Adv. Mater.*, **2014**, *26* (34), 5930–5935.

[54] Weiß, M. Hierarchically Structured Porous Bodies from Capillary Suspensions. **2019**, No. May, 61.

[55] Voosen, P. Global Temperatures in 2020 Tied Record Highs. *Science (80-. ).*, **2021**, *37* (6527), 334–336.

[56] Fischer, G.; Tubiello, F. N.; van Velthuizen, H.; Wiberg, D. A. Climate Change Impacts on Irrigation Water Requirements: Effects of Mitigation, 1990-2080. *Technol. Forecast. Soc. Change*, **2007**, *74* (7), 1083–1107.

[57] Siebert, S.; Döll, P. Quantifying Blue and Green Virtual Water Contents in Global Crop Production as Well as Potential Production Losses without Irrigation. *J. Hydrol.*, **2010**, *384* (3–4), 198–217.

[58] Hamdy, A.; Ragab, R.; Scarascia-Mugnozza, E. Coping with Water Scarcity: Water Saving and Increasing Water Productivity. *Irrig. Drain.*, **2003**, *52* (1), 3–20.

[59] Bittelli, M. Measuring Soil Water Potential Forwater Management in Agriculture: A Review. *Sustainability*, **2010**, *2* (5), 1226–1251.

[60] McDermid, S. S.; Mahmood, R.; Hayes, M. J.; Bell, J. E.; Lieberman, Z. Minimizing Trade-Offs for Sustainable Irrigation. *Nat. Geosci.*, **2021**, *14* (10), 706–709.

[61] Lischeid, G.; Merz, C.; Schindler, U.; Schulz, R.; Steidl, J.; Tauschke, R. Quantifying Process Heterogeneity : Signal Propagation in Hydrological Systems. *Assembly*, **2009**, *11*, 6701.

[62] Hardie, M. Review of Novel and Emerging Proximal Soil Moisture Sensors for Use in Agriculture. *Sensors (Switzerland)*, **2020**, *20* (23), 1–23.

[63] Degré, A.; van der Ploeg, M. J.; Caldwell, T.; Gooren, H. P. A. Comparison of Soil Water Potential Sensors: A Drying Experiment. *Vadose Zo. J.*, **2017**, *16* (4), vzj2016.08.0067.

[64] Jackisch, C.; Germer, K.; Graeff, T.; Andrä, I.; Schulz, K.; Schiedung, M.; Haller-Jans, J.; Schneider, J.; Jaquemotte, J.; Helmer, P.; et al. Soil Moisture and Matric Potential-an Open Field Comparison of Sensor Systems. *Earth Syst. Sci. Data*, **2020**, *12* (1), 683–697.

[65] Novick, K. A.; Ficklin, D. L.; Baldocchi, D.; Davis, K. J.; Ghezzehei, T. A.; Konings, A. G.; MacBean, N.; Raoult, N.; Scott, R. L.; Shi, Y.; et al. Confronting the Water Potential Information Gap. *Nat. Geosci.*, **2022**, *15* (3), 158–164.

[66] Muñoz-Carpena, R. Field Devices For Monitoring Soil Water Content. *Edis*, **1969**, *2004* (8), 1–16.

[67] Whalley, W. R.; Watts, C. W.; Hilhorst, M. A.; Bird, N. R. A.; Balendonck, J.; Longstaff, D. J. The Design of Porous Material Sensors to Measure the Matric Potential of Water in Soil. *Eur. J. Soil Sci.*, **2001**, *52* (3), 511–519.

[68] Whalley, W. R.; Clark, L. J.; Take, W. A.; Bird, N. R. A.; Leech, P. K.; Cope, R. E.; Watts, C. W. A Porous-Matrix Sensor to Measure the Matric Potential of Soil Water in the Field. *Eur. J. Soil Sci.*, **2007**, *58* (1), 18–25.

[69] Whalley, W. R.; Lock, G.; Jenkins, M.; Peloe, T.; Burek, K.; Balendonck, J.; Take, W. A.; Tuzel, İ. H.; Tuzel, Y. Measurement of Low Matric Potentials with Porous Matrix Sensors and Water-Filled Tensiometers. *Soil Sci. Soc. Am. J.*, **2009**, *73* (6), 1796–1803.

[70] Or, D.; Wraith, J. M. A New Soil Matric Potential Sensor Based on Time Domain Reflectometry. *Water Resour. Res.*, **1999**, *35* (11), 3399–3407.

[71] da Mota, W. N.; Evangelista, A. W. P.; Maia, L. J. Q.; Correchel, V.; Alves, J.; Varrone, L. F. R.; Gitirana, G. de F. N. Development of a Heat Pulse Sensor for Measuring Matric Suction on Soilless Substrates. *Comput. Electron. Agric.*, **2021**, *185* (March).

[72] Chen, C.; Yan, X.; Xu, Q.; Yu, S.; Ma, Y.; Cheng, X.; Wang, Z.; Cheng, Q. A Novel Frequency Domain Impedance Sensor with a Perforated Cylinder Coaxial Design for In-Situ Measuring Soil Matric Potential. *Sensors (Switzerland)*, **2019**, *19* (11).

[73] Carvalhaes-Dias, P.; Morais, F. J. O.; Duarte, L. F. C.; Cabot, A.; Dias, J. A. S. Autonomous Soilwater Content Sensors Based on Bipolar Transistors Encapsulated in Porous Ceramic Blocks. *Appl. Sci.*, **2019**, *9* (6).

[74] Chen, Y.; Tian, Y.; Wang, X.; Dong, L. Miniaturized Soil Sensor for Continuous, In-Situ Monitoring of Soil Water Potential. *2019 20th Int. Conf. Solid-State Sensors, Actuators Microsystems Eurosensors XXXIII, TRANSDUCERS 2019 EUROSENSORS XXXIII*, **2019**, No. June, 2025–2028.

[75] Goodchild, M. S.; Jenkins, M. D.; Whalley, W. R.; Watts, C. W. A Novel Dielectric Tensiometer Enabling Precision PID-Based Irrigation Control of Polytunnel-Grown Strawberries in Coir. *Biosyst. Eng.*, **2018**, *165*, 70–76.

[76] Lungal, M.; Si, B. C. Coiled Time Domain Reflectometry Matric Potential Sensor. *Soil Sci. Soc. Am. J.*, **2008**, *72* (5), 1422–1424.

[77] Matile, L.; Berger, R.; Wächter, D.; Krebs, R. Characterization of a New Heat Dissipation Matric Potential Sensor. *Sensors (Switzerland)*, **2013**, *13* (1), 1137–1145.

[78] Persson, M.; Wraith, J. M.; Dahlin, T. A Small-Scale Matric Potential Sensor Based on Time Domain Reflectometry. *Soil Sci. Soc. Am. J.*, **2006**, *70* (2), 533–536.

[79] Xin, X. L.; Xu, F. A.; Zhang, J. B.; Xu, M. X. A New Resistance Sensor for Monitoring Soil Matric Potential. *Soil Sci. Soc. Am. J.*, **2007**, *71* (3), 866–871.

[80] METER Group AG. TEROS 21 _ Soil Water Potential Sensor _ METER Environment https://www.metergroup.com/environment/products/teros-21/ (accessed Mar 5, 2022).

[81] MMM tech support GmbH & Co. KG. Irrometer Company Watermark Sensor - MMM - Mosler Tech Support https://www.mmm-tech.de/de/watermark/wms#top (accessed Mar 5, 2022).

[82] Delta-T Devices Ltd. EQ3 Equitensiometer - Soil Water Potential https://www.delta-t.co.uk/product/eq3/ (accessed Mar 5, 2022).

[83] EcoTech Umwelt Meßsysteme GmbH. EcoTech Umwelt Meßsysteme GmbH Tensiomark https://www.ecotech.de/produkt/tensiomark (accessed Mar 5, 2022).

[84] Bakker, G.; van der Ploeg, M. J.; de Rooij, G. H.; Hoogendam, C. W.; Gooren, H. P. A.; Huiskes, C.; Koopal, L. K.; Kruidhof, H. New Polymer Tensiometers: Measuring Matric Pressures Down to the Wilting Point. *Vadose Zo. J.*, **2007**, *6* (1), 196–202.

[85] Umwelt-Geräte-Technik GmbH. UGT Umwelt-Geräte-Technik Watermark https://www.ugt-online.de/en/products/soil-science/tensiometers/watermark (accessed Mar 5, 2022).

[86] Van Der Ploeg, M. J.; Gooren, H. P. A.; Bakker, G.; Hoogendam, C. W.; Huiskes, C.; Koopal, L. K.; Kruidhof, H.; De Rooij, G. H. Polymer Tensiometers with Ceramic Cones: Direct Observations of Matric Pressures in Drying Soils. *Hydrol. Earth Syst. Sci.*, **2010**, *14* (10), 1787–1799.

[87] Hübner, C.; Kaatze, U. *Electromagnetic Moisture Measurement*; 2017.

[88] Schlaeger, S.; Huebner, C.; Becker, R. Simple Soil Moisture Probe for Low-Cost Measurement Applications. *Proc. 6th Conf. Electromagn. Wave Interact. with Water Moist Subst. ISEMA*, **2005**, 258–265.

[89] Zazueta, F.; Xin, J. Soil Moisture Sensors| Netafim https://www.netafimindia.com/digital-farming/netbeat/Monitor/soil-moisture-sensors/.

[90] Pham, H. Q.; Fredlund, D. G.; Barbour, S. L. A Study of Hysteresis Models for Soil-Water Characteristic Curves. *Can. Geotech. J.*, **2005**, *42* (6), 1548–1568.

[91] Saggio-Woyansky, J.; Scott, C. E.; Minnear, W. P. Processing of Porous Ceramics. *Am. Ceram. Soc. Bull.*, **1992**, *71* (11), 1674–1682.

[92] Montanaro, L.; Jorand, Y.; Fantozzi, G.; Negro, A. Ceramic Foams by Powder Processing. *J. Eur. Ceram. Soc.*, **1998**, *18* (9), 1339–1350.

[93] Li, S. H.; De Wijn, J. R.; Layrolle, P.; De Groot, K. Novel Method to Manufacture Porous Hydroxyapatite by Dual-Phase Mixing. *J. Am. Ceram. Soc.*, **2003**, *86* (1), 65–72.

[94] Truby, R. L.; Lewis, J. A. Printing Soft Matter in Three Dimensions. *Nature*, **2016**, *540* (7633), 371–378.

[95] Lewis, J. A.; Smay, J. E.; Stuecker, J.; Cesarano, J. Direct Ink Writing of Three-Dimensional Ceramic Structures. *J. Am. Ceram. Soc.*, **2006**, *89* (12), 3599–3609.

[96] Minas, C.; Carnelli, D.; Tervoort, E.; Studart, A. R. 3D Printing of Emulsions and Foams into Hierarchical Porous Ceramics. *Adv. Mater.*, **2016**, *28* (45), 9993–9999.

[97] Muth, J. T.; Dixon, P. G.; Woish, L.; Gibson, L. J.; Lewis, J. A. Architected Cellular Ceramics with Tailored Stiffness via Direct Foam Writing. *Proc. Natl. Acad. Sci. U. S. A.*, **2017**, *114* (8), 1832–1837.

[98] Li, M.; Pietrowski, M. J.; De Souza, R. A.; Zhang, H.; Reaney, I. M.; Cook, S. N.; Kilner, J. A.; Sinclair, D. C. A Family of Oxide Ion Conductors Based on the Ferroelectric Perovskite Na0.5Bi0.5TiO3. *Nat. Mater.*, **2014**, *13* (1), 31–35.

[99] Papac, M.; Stevanović, V.; Zakutayev, A.; O'Hayre, R. Triple Ionic–Electronic Conducting Oxides for next-Generation Electrochemical Devices. *Nat. Mater.*, **2021**, *20* (3), 301–313.

[100] Sun, H.; Zhu, J.; Baumann, D.; Peng, L.; Xu, Y.; Shakir, I.; Huang, Y.; Duan, X. Hierarchical 3D Electrodes for Electrochemical Energy Storage. *Nat. Rev. Mater.*, **2019**, *4* (1), 45–60.

[101] Zhu, T.; Liu, Y.; Fu, C.; Heremans, J. P.; Snyder, J. G.; Zhao, X. Compromise and Synergy in High-Efficiency Thermoelectric Materials. *Adv. Mater.*, **2017**, *29* (14).

[102] Roscow, J. I.; Zhang, Y.; Kraśny, M. J.; Lewis, R. W. C.; Taylor, J.; Bowen, C. R. Freeze Cast Porous Barium Titanate for Enhanced Piezoelectric Energy Harvesting. *J. Phys. D. Appl. Phys.*, **2018**, *51* (22).

[103] Fukada, E.; Yasuda, I. On the Piezoelectric Effect of Bone. *Journal of the Physical Society of Japan*. 1957, pp 1158–1162.

[104] Fukada, E.; Yasuda, I. Piezoelectric Effects in Collagen. *Japanese J. Appl. Physics, Part 1 Regul. Pap. Short Notes Rev. Pap.*, **1964**, *3* (8), 502B.

[105] Tofail, S. A. M.; Haverty, D.; Cox, F.; Erhart, J.; Hána, P.; Ryzhenko, V. Direct and Ultrasonic Measurements of Macroscopic Piezoelectricity in Sintered Hydroxyapatite. *J. Appl. Phys.*, **2009**, *105* (6).

[106] Tofail, S. A. M.; Zhang, Y.; Gandhi, A. A. Piezoelectricity of Bone from a New Perspective. *Proc. - Int. Symp. Electrets*, **2011**, 91–92.

[107] Zhang, Y.; Chen, L.; Zeng, J.; Zhou, K.; Zhang, D. Aligned Porous Barium Titanate/Hydroxyapatite Composites with High Piezoelectric Coefficients for Bone Tissue Engineering. *Mater. Sci. Eng. C*, **2014**, *39* (1), 143–149.

[108] Poon, K. K.; Wurm, M. C.; Evans, D. M.; Einarsrud, M. A.; Lutz, R.; Glaum, J. Biocompatibility of (Ba,Ca)(Zr,Ti)O3 Piezoelectric Ceramics for Bone Replacement Materials. *J. Biomed. Mater. Res. - Part B Appl. Biomater.*, **2020**, *108* (4), 1295–1303.

[109] Rotan, M.; Zhuk, M.; Boughton, P.; Glaum, J. The Influence of Low-Temperature Sterilization Procedures on Piezoelectric Ceramics for Biomedical Applications. *Open Ceram.*, **2021**, *7* (May), 100143.

[110] Lang, T.; LeBlanc, A.; Evans, H.; Lu, Y.; Genant, H.; Yu, A. Cortical and Trabecular Bone Mineral Loss from the Spine and Hip in Long-Duration Spaceflight. *J. Bone Miner. Res.*, **2004**, *19* (6), 1006–1012.

[111] Xu, Z.; Jin, C.; Cabe, A.; Escobedo, D.; Hao, N.; Trase, I.; Closson, A. B.; Dong, L.; Nie, Y.; Elliott, J.; et al. Flexible Energy Harvester on a Pacemaker Lead Using Multibeam Piezoelectric Composite Thin Films. *ACS Appl. Mater. Interfaces*, **2020**, *12* (30), 34170–34179.

[112] Jin, C.; Hao, N.; Xu, Z.; Trase, I.; Nie, Y.; Dong, L.; Closson, A.; Chen, Z.; Zhang, J. X. J. Flexible Piezoelectric Nanogenerators Using Metal-Doped ZnO-PVDF Films. *Sensors Actuators, A Phys.*, **2020**, *305*, 111912.

[113] Jin, C.; Dong, L.; Xu, Z.; Closson, A.; Cabe, A.; Gruslova, A.; Jenney, S.; Escobedo, D.; Elliott, J.; Zhang, M.; et al. Skin-like Elastomer Embedded Zinc Oxide Nanoarrays for Biomechanical Energy Harvesting. *Adv. Mater. Interfaces*, **2021**, *8* (10), 1–10.

[114] Safari, A.; Akdogan, E. K. Rapid Prototyping of Novel Piezoelectric Composites. *Ferroelectrics*, **2006**, *331*, 153–179.

[115] Zhang, Y.; Roscow, J.; Xie, M.; Bowen, C. High Piezoelectric Sensitivity and Hydrostatic Figures of Merit in Unidirectional Porous Ferroelectric Ceramics Fabricated by Freeze Casting. *J. Eur. Ceram. Soc.*, **2018**, *38* (12), 4203–4211.

[116] Roscow, J. I.; Lewis, R. W. C.; Taylor, J.; Bowen, C. R. Modelling and Fabrication of Porous Sandwich Layer Barium Titanate with Improved Piezoelectric Energy Harvesting Figures of Merit. *Acta Mater.*, **2017**, *128*, 207–217.

[117] Huang, L.; Qin, H.; Hu, T.; Xie, J.; Guo, W.; Gao, P.; Xiao, H. Fabrication of High Permeability SiC Ceramic Membrane with Gradient Pore Structure by One-Step Freeze-Casting Process. *Ceram. Int.*, **2021**, *47* (12), 17597–17605.

[118] Yan, M.; Zhong, J.; Liu, S.; Xiao, Z.; Yuan, X.; Zhai, D.; Zhou, K.; Li, Z.; Zhang, D.; Bowen, C.; et al. Flexible Pillar-Base Structured Piezocomposite with Aligned Porosity for Piezoelectric Energy Harvesting. *Nano Energy*, **2021**, *88* (June), 106278.

[119] Olhero, S. M.; Garcia-Gancedo, L.; Button, T. W.; Alves, F. J.; Ferreira, J. M. F. Innovative Fabrication of PZT Pillar Arrays by a Colloidal Approach. *J. Eur. Ceram. Soc.*, **2012**, *32* (5), 1067–1075.

[120] Brennan, R. E.; Turcu, S.; Hall, A.; Hagh, N. M.; Safari, A. Fabrication of Electroceramic Components by Layered Manufacturing (LM). *Ferroelectrics*, **2003**, *293* (Lm), 3–17.

[121] Cui, H.; Hensleigh, R.; Yao, D.; Maurya, D.; Kumar, P.; Kang, M. G.; Priya, S.; Zheng, X. (Rayne). Three-Dimensional Printing of Piezoelectric Materials with Designed Anisotropy and Directional Response. *Nat. Mater.*, **2019**, *18* (3), 234–241.

[122] Liu, W.; Wang, D.; Huang, J.; Wei, Y.; Xiong, J.; Zhu, W.; Duan, L.; Chen, J.; Sun, R.; Wang, D. Low-Temperature Deposition Manufacturing: A Novel and Promising Rapid Prototyping Technology for the Fabrication of Tissue-Engineered Scaffold. *Mater. Sci. Eng. C*, **2017**, *70*, 976–982.

[123] Tariverdian, T.; Behnamghader, A.; Brouki Milan, P.; Barzegar-Bafrooei, H.; Mozafari, M. 3D-Printed Barium Strontium Titanate-Based Piezoelectric Scaffolds for Bone Tissue Engineering. *Ceram. Int.*, **2019**, *45* (11), 14029–14038.

[124] Gaytan, S. M.; Cadena, M. A.; Karim, H.; Delfin, D.; Lin, Y.; Espalin, D.; MacDonald, E.; Wicker, R. B. Fabrication of Barium Titanate by Binder Jetting Additive Manufacturing Technology. *Ceram. Int.*, **2015**, *41* (5), 6610–6619.

[125] Polley, C.; Distler, T.; Detsch, R.; Lund, H.; Springer, A.; Boccaccini, A. R.; Seitz, H. 3D Printing of Piezoelectric Barium Titanate-Hydroxyapatite Scaffiolds with Interconnected Porosity for Bone Tissue Engineering. *Materials (Basel).*, **2020**, *13* (7).

[126] Kim, H.; Renteria-Marquez, A.; Islam, M. D.; Chavez, L. A.; Garcia Rosales, C. A.; Ahsan, M. A.; Tseng, T. L. B.; Love, N. D.; Lin, Y. Fabrication of Bulk Piezoelectric and Dielectric BaTiO 3 Ceramics Using Paste Extrusion 3D Printing Technique. *J. Am. Ceram. Soc.*, **2019**, *102* (6), 3685–3694.

[127] Kim, H.; Fernando, T.; Li, M.; Lin, Y.; Tseng, T. L. B. Fabrication and Characterization of 3D Printed BaTiO3/PVDF Nanocomposites. *J. Compos. Mater.*, **2018**, *52* (2), 197–206.

[128] Kim, H.; Johnson, J.; Chavez, L. A.; Garcia Rosales, C. A.; Tseng, T. L. B.; Lin, Y. Enhanced Dielectric Properties of Three Phase Dielectric MWCNTs/BaTiO3/PVDF Nanocomposites for Energy Storage Using Fused Deposition Modeling 3D Printing. *Ceram. Int.*, **2018**, *44* (8), 9037–9044.

[129] Qi, F.; Chen, N.; Wang, Q. Dielectric and Piezoelectric Properties in Selective Laser Sintered Polyamide11/BaTiO3/CNT Ternary Nanocomposites. *Mater. Des.*, **2018**, *143*, 72–80.

[130] Kim, H.; Torres, F.; Villagran, D.; Stewart, C.; Lin, Y.; Tseng, T. L. B. 3D Printing of BaTiO3/PVDF Composites with Electric In Situ Poling for Pressure Sensor Applications. *Macromol. Mater. Eng.*, **2017**, *302* (11), 1–6.

[131] Malakooti, M. H.; Julé, F.; Sodano, H. A. Printed Nanocomposite Energy Harvesters with Controlled Alignment of Barium Titanate Nanowires. *ACS Appl. Mater. Interfaces*, **2018**, *10* (44), 38359–38367.

[132] Lorenz, M.; Martin, A.; Webber, K. G.; Travitzky, N. Electromechanical Properties of Robocasted Barium Titanate Ceramics. *Adv. Eng. Mater.*, **2020**, *22* (9), 1–10.

[133] Gadea, C.; Spelta, T.; Simonsen, S. B.; Esposito, V.; Bowen, J. R.; Haugen, A. B. Hybrid Inks for 3D Printing of Tall BaTiO3-Based Ceramics. *Open Ceram.*, **2021**, *6* (April), 100110.

[134] Smay, J. E.; Nadkarni, S. S.; Xu, J. Direct Writing of Dielectric Ceramics and Base Metal Electrodes. *Int. J. Appl. Ceram. Technol.*, **2007**, *4* (1), 47–52.

[135] del-Mazo-Barbara, L.; Ginebra, M. P. Rheological Characterisation of Ceramic Inks for 3D Direct Ink Writing: A Review. *J. Eur. Ceram. Soc.*, **2021**, *41* (16), 18–33.

[136] da Silva, L. L.; Hinterstein, M. Size Effect on Ferroelectricity in Nanoscaled BaTiO3. In *Engineering Materials*; Springer, 2022; pp 123–133.

[137] Picht, G.; Khansur, N. H.; Webber, K. G.; Kungl, H.; Hoffmann, M. J.; Hinterstein, M. Grain Size Effects in Donor Doped Lead Zirconate Titanate Ceramics. *J. Appl. Phys.*, **2020**, *128* (21), 0–14.

[138] Roscow, J.; Zhang, Y.; Taylor, J.; Bowen, C. R. Porous Ferroelectrics for Energy Harvesting Applications. *Eur. Phys. J. Spec. Top.*, **2015**, *224* (14–15), 2949–2966.

[139] Simons, H.; Haugen, A. B.; Jakobsen, A. C.; Schmidt, S.; Stöhr, F.; Majkut, M.; Detlefs, C.; Daniels, J. E.; Damjanovic, D.; Poulsen, H. F. Long-Range Symmetry Breaking in Embedded Ferroelectrics. *Nat. Mater.*, **2018**, *17* (9), 814–819.

[140] Daniels, J. E.; Majkut, M.; Cao, Q.; Schmidt, S.; Wright, J.; Jo, W.; Oddershede, J. Heterogeneous Grain-Scale Response in Ferroic Polycrystals under Electric Field. *Sci. Rep.*, **2016**, *6* (December 2015), 1–7.

[141] Roscow, J. I.; Pearce, H.; Khanbareh, H.; Kar-Narayan, S.; Bowen, C. R. Modified Energy Harvesting Figures of Merit for Stress- and Strain-Driven Piezoelectric Systems. *Eur. Phys. J. Spec. Top.*, **2019**, *228* (7), 1537–1554.

[142] Roscow, J. I.; Taylor, J.; Bowen, C. R. Manufacture and Characterization of Porous Ferroelectrics for Piezoelectric Energy Harvesting Applications. *Ferroelectrics*, **2016**, *498* (1), 40–46.

[143] Ghanbarian-Alavijeh, B.; Millán, H. The Relationship between Surface Fractal Dimension and Soil Water Content at Permanent Wilting Point. *Geoderma*, **2009**, *151* (3–4), 224–232.

[144] Acosta, M.; Novak, N.; Rojas, V.; Patel, S.; Vaish, R.; Koruza, J.; Rossetti, G. A.; Rödel, J. BaTiO3-Based Piezoelectrics: Fundamentals, Current Status, and Perspectives. *Appl. Phys. Rev.*, **2017**, *4* (4).

[145] LeGeros, R. Z. Calcium Phosphate-Based Osteoinductive Materials. *Chem. Rev.*, **2008**, *108* (11), 4742–4753.

[146] Tsuruga, E.; Takita, H.; Itoh, H.; Wakisaka, Y.; Kuboki, Y. Pore Size of Porous Hydroxyapatite as the Cell-Substratum Controls BMP-Induced Osteogenesis. *J. Biochem.*, **1997**, *121* (2), 317–324.

[147] Ghayor, C.; Bhattacharya, I.; Weber, F. E. The Optimal Microarchitecture of 3D-Printed β-TCP Bone Substitutes for Vertical Bone Augmentation Differs from That for Osteoconduction. *Mater. Des.*, **2021**, *204*, 0–7.

[148] Ghayor, C.; Chen, T. H.; Bhattacharya, I.; Özcan, M.; Weber, F. E. Microporosities in 3d-Printed Tricalcium-Phosphate-Based Bone Substitutes Enhance Osteoconduction and Affect Osteoclastic Resorption. *Int. J. Mol. Sci.*, **2020**, *21* (23), 1–15.

[149] Ghayor, C.; Bhattacharya, I.; Guerrero, J.; Özcan, M.; Weber, F. E. 3D-Printed HA-Based Scaffolds for Bone Regeneration: Microporosity, Osteoconduction and Osteoclastic Resorption. *Materials (Basel).*, **2022**, *15* (4), 1–12.

[150] Somers, N.; Jean, F.; Lasgorceix, M.; Curto, H.; Urruth, G.; Thuault, A.; Petit, F.; Leriche, A. Influence of Dopants on Thermal Stability and Densification of β-Tricalcium Phosphate Powders. *Open Ceram.*, **2021**, *7* (December 2020), 100168.

[151] Koivisto, J. T.; Oelschlaeger, C.; Menne, D.; Willenbacher, N.; Näreoja, T. Microrheology Study on Matrix Remodelling by Osteoblasts in 3D Hydrogel in Vitro Culture. *Bone Reports*, **2022**, *16*, 101388.

[152] de Wildt, B. W. M.; Ansari, S.; Sommerdijk, N. A. J. M.; Ito, K.; Akiva, A.; Hofmann, S. From Bone Regeneration to Three-Dimensional in Vitro Models: Tissue Engineering of Organized Bone Extracellular Matrix. *Curr. Opin. Biomed. Eng.*, **2019**, *10*, 107–115.

# 8 Additional sheets at the end of the thesis for publication-based dissertations.

Zusatzblatt am Ende der Arbeit bei publikationsbasierten Dissertationen

**Chapter 4: Verification of the contribution from the co-authors**

Title: A Robust Soil Water Potential Sensor with High Sensitivity and Broad Measuring Range

Journal: IEEE

Authors: David Menne; Christof Hübner; Dennis Trebbels; Norbert Willenbacher

**Position in the dissertation:**

The content of this paper has been included in Chapter 3

Contribution of “David Menne”: Conceptualization, Software, Validation, Formal analysis, Investigation, Data Curation, Writing - Original Draft, Writing - Review & Editing, Visualization, Project administration

Contribution of “Christof Hübner”: Conceptualization, Investigation, Software, Validation, Resources, Writing - Review & Editing, Supervision

Contribution of “Dennis Trebbels”: Software, Resources, Review

Contribution of “Norbert Willenbacher”: Conceptualization, Validation, Resources, Writing - Review & Editing, Supervision, Funding acquisition

Zusatzblatt am Ende der Arbeit bei publikationsbasierten Dissertationen

**Chapter 4: Verification of the contribution from the co-authors**

Title: Robust Soil Water Potential Sensor to Optimize Irrigation in Agriculture

Journal: Sensors

Authors: David Menne; Christof Hübner; Dennis Trebbels; Norbert Willenbacher

**Position in the dissertation:**

The content of this paper has been included in Chapter 3

Contribution of “David Menne”: Conceptualization, Software, Validation, Formal analysis, Investigation, Data Curation, Writing - Original Draft, Writing - Review & Editing, Visualization, Project administration

Contribution of “Christof Hübner”: Conceptualization, Investigation, Software, Validation, Resources, Writing - Review & Editing, Supervision

Contribution of “Dennis Trebbels”: Software, Resources, Review

Contribution of “Norbert Willenbacher”: Conceptualization, Validation, Resources, Writing - Review & Editing, Supervision, Funding acquisition

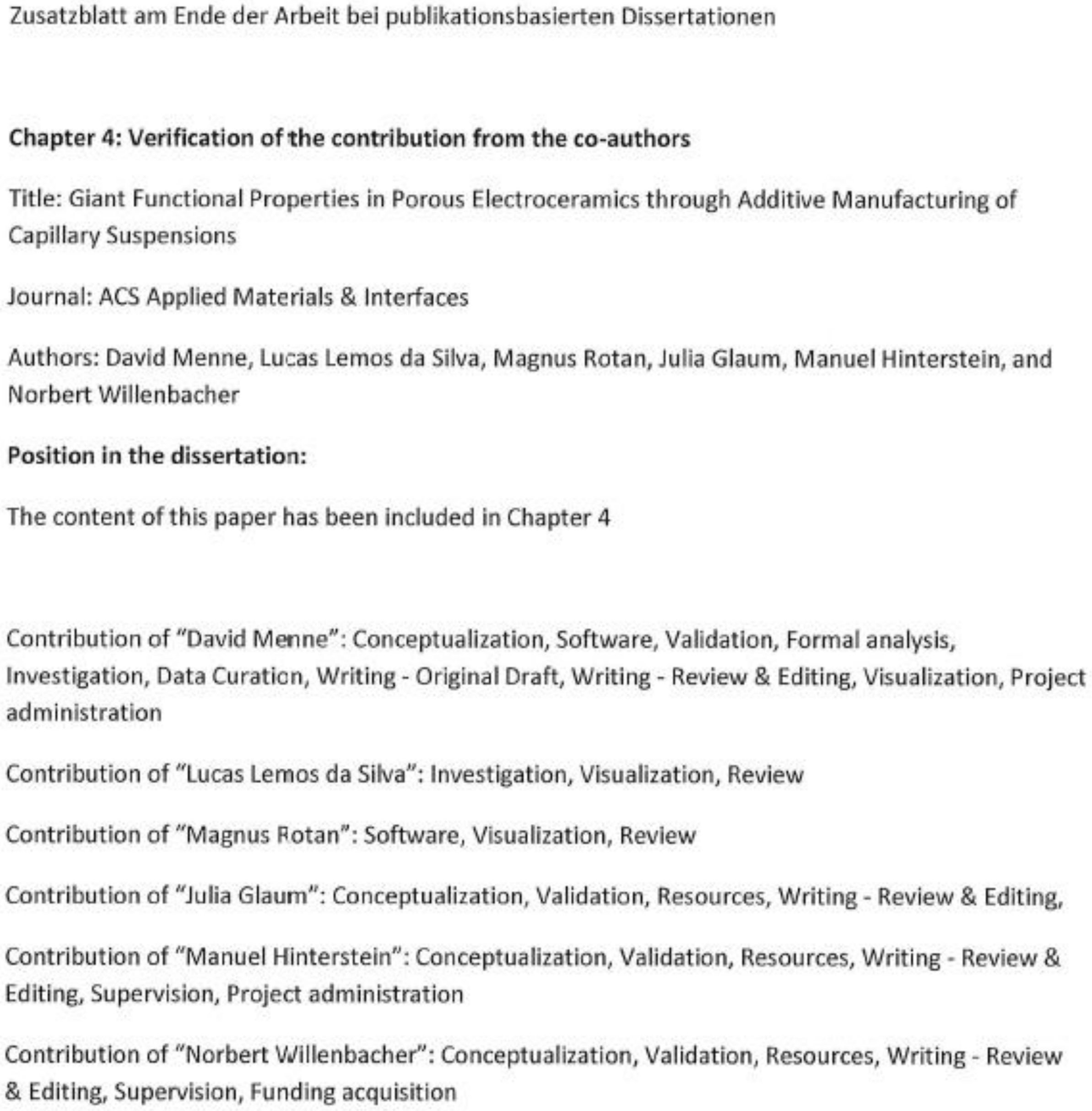

Zusatzblatt am Ende der Arbeit bei publikationsbasierten Dissertationen

## Chapter 4: Verification of the contribution from the co-authors

Title: Giant Functional Properties in Porous Electroceramics through Additive Manufacturing of Capillary Suspensions

Journal: ACS Applied Materials & Interfaces

Authors: David Menne, Lucas Lemos da Silva, Magnus Rotan, Julia Glaum, Manuel Hinterstein, and Norbert Willenbacher

**Position in the dissertation:**

The content of this paper has been included in Chapter 4

Contribution of “David Menne”: Conceptualization, Software, Validation, Formal analysis, Investigation, Data Curation, Writing - Original Draft, Writing - Review & Editing, Visualization, Project administration

Contribution of “Lucas Lemos da Silva”: Investigation, Visualization, Review

Contribution of “Magnus Rotan”: Software, Visualization, Review

Contribution of “Julia Glaum”: Conceptualization, Validation, Resources, Writing - Review & Editing,

Contribution of “Manuel Hinterstein”: Conceptualization, Validation, Resources, Writing - Review & Editing, Supervision, Project administration

Contribution of “Norbert Willenbacher”: Conceptualization, Validation, Resources, Writing - Review & Editing, Supervision, Funding acquisition